Synthesis and Characterization of Nanostructured ZnO- and $BiFeO_3$-Based Multifunctional Materials

By
Marco A. Gálvez Saldaña

A thesis submitted in partial fulfillment of the requirements for the degree of

MASTER OF SCIENCE
In
Physics
UNIVERSITY OF PUERTO RICO, MAYAGUEZ CAMPUS
2012

Approved by:

Oscar Perales-Perez, PhD President, Graduate Committee	Date
Henri Radovan, Ph.D Member, Graduate Committee	Date
Félix Fernández, Ph.D Member, Graduate Committee	Date
Raúl E. Macchiavelli, Ph.D Representative of Graduate Studies	Date
Dorial Castellanos, Ph.D Director of Department of Physics	Date

ABSTRACT

The effective incorporation of dopant species into ZnO host structure usually induces changes in its physical and chemical properties enabling the establishment of novel multi-functional properties. In the case of doping with transition metal ions, the subsequent exchange interaction between available spins of the magnetic species would induce a ferromagnetic behavior in the so-called ZnO-based diluted magnetic semiconductor. This ferromagnetic functionality will enable the application of this material in data storage and spintronics-based devices. On this basis, a systematic study was carried out to determine the effect of composition and crystal size on the structural, optical and magnetic properties of pure and doped ZnO $[Zn_{1-x}(M)_xO]$, where M: Co (II), Sc(III) or V(III), nanocrystalline powders and films. The Co, Sc and V doping levels varied in the 0.0 at% to 10 at% range.

Powders and films were synthesized via a sol-gel approach, where ethanolamine was used to increase the viscosity of the precursor solutions and promote the adhesion of precursor and final oxides onto quartz and Silicon (100) substrates. Thermogravimetric analysis in air suggested the complete formation of the oxide structure at temperatures above 350ºC. X-ray diffractometry verified the development of the ZnO host structure after annealing of the precursors. The average crystallite size of ZnO powders varied from 25 nm to 30 nm when the samples were annealed in air at 400ºC and 500ºC, respectively, for 1hour. Sc and V dopants produce a decrease in the average crystallite size. This behavior is also observed in the samples of doped ZnO films, in this case the average crystallite size decreases from 24 nm to 15 nm annealed at 500ºC and from 27 nm to 14 nm in the films annealed at 550ºC. UV-vis and photoluminescence (PL) measurements corroborated the formation of high-quality ZnO host structure. PL measurements evidenced an

intense emission peak in the UV region around 390 nm, for an excitation wavelength of 342 nm. The intensity of this main emission peak was strongly dependent on the level of Co, Sc and V species in both powders and thin films. Furthermore, it was found that the dopant concentration and the annealing temperature play an important role in the ferromagnetic behavior of the material.

On the other hand, multiferroic materials are the focus of intensive research because of their expected improved performance in data storage and processing devices. Bismuth Ferrite, $BiFeO_3$ or BFO, is a multiferroic with a non-centro symmetric rhombohedral perovskite structure that exhibits antiferromagnetic and ferroelectric behaviors. Challenges associated with the synthesis of this material are the co-existence of BFO with impurity compounds. The incorporation of specific dopant species (transition metal or rare earths) in the BFO structure can enhance the ferroelectric properties and produce a weak ferromagnetic response. Accordingly, the present study was focused on evaluating the effect on the physical properties of the partial substitution of Praseodymium species in Bi-site in BFO structure as well as the substitution of Cobalt ions in Fe-site in BFO films. The level of the doping species varied from 0 at% to 4 at% BFO thin films were synthesized by a sol-gel approach, where glycol was aggregated to the main solvent to increase the viscosity of the precursor solutions and promote their adhesion onto platinum substrates. The development of the host BFO structure was confirmed by XRD analyses of samples annealed at 500ºC for two hours in air, all samples showed single phase corresponding to rhombohedral BFO. The average crystallite size varied from 28 nm to 40 nm and 28nm to 31nm for Pr doped BFO and Co doped BFO films, respectively, with a rise of the doping level. In turn, the corresponding coercivity value was increased from 166 Oe to 428 Oe in pure and 4

at% doped Pr-doped samples respectively and there was no variation in coercivity with respect to the pure films in the Cobalt system. Furthermore a weak ferroelectric behavior was observed, with predominant paraelectric response in pure and doped films in both systems.

RESUMEN

La efectiva incorporación de especies dopantes en la estructura del ZnO usualmente induce cambios en sus propiedades físicas y químicas, permitiendo establecer nuevas propiedades multifuncionales. En el caso del dopaje con iones de metales de transición, la subsecuente interacción de intercambio entre los espines disponibles de las especies magnéticas induciría un comportamiento ferromagnético en estos materiales llamados diluidos magnéticos semiconductores basados en ZnO. Esta característica ferromagnética permitirá la aplicación de este material en dispositivos de almacenamiento de datos y 'spintronic'. Sobre esta base, se realizó un estudio sistemático para determinar el efecto de la composición y el tamaño del cristal en las propiedades estructurales, ópticas y magnéticas de polvos y películas de ZnO puro y dopado [$Zn_{1-x}M_xO$], donde M es Co (II), Sc(III) y V(III). Los niveles de dopaje de Co, Sc y V variaron desde 0.0 at% hasta 10 at%.

Los polvos y las películas se sintetizaron por el método de 'sol-gel'. Para crecer las películas se utilizó etanolamina para incrementar la viscosidad de las soluciones precursoras y promover la adhesión de las películas en los sustratos de cuarzo y silicio (100).

Las mediciones de análisis termo-gravimétrico en aire sugirieron la formación completa de la estructura del óxido a temperaturas por encima de los 350ºC. La difractometría de rayos X verificó la obtención de la estructura del ZnO después de un recocido de los precursores. El tamaño promedio del cristalito en los polvos de ZnO varió desde 25 nm hasta 30 nm cuando las muestras fueron recocidas en aire a 400ºC y 500ºC respectivamente durante una hora. Los dopantes Escandio y Vanadio producen una disminución en el tamaño promedio del cristalito. Este comportamiento también es observado para las películas delgadas de ZnO dopadas, en este

caso el tamaño promedio del cristalito disminuyó desde 24 nm hasta 15 nm para las películas recocidas a 500ºC y desde 27 nm hasta14 nm en las películas recocidas a 550ºC. Las mediciones de UV-visible y fotoluminiscencia corroboraron la formación de una estructura de ZnO de alta calidad. Las mediciones de fotoluminiscencia evidenciaron un pico de emisión intensa en la región ultravioleta alrededor de 390 nm para una longitud de onda de excitación de 342 nm. La intensidad de este pico de emisión fue fuertemente dependiente de los niveles de dopaje de Co, Sc, V para ambos sistemas polvos y películas. Además se encontró que la concentración de los dopantes y la temperatura de recocido juegan un papel importante en el comportamiento ferromagnético del material.

Por otro lado, los materiales multiferróicos están siendo el centro de atención de intensa investigación debido a las mejoras en el rendimiento en los dispositivos de almacenamiento y procesamiento de datos que generaría este material. La ferrita de bismuto $BiFeO_3$ o BFO, es multiferroico con una estructura romboidal no centro- simétrica del tipo de las perovskitas, que exhibe comportamientos antiferromagnético y ferroléctrico. Los desafíos asociados con la síntesis de este material son la coexistencia de impurezas en la BFO. La incorporación de especies dopantes específicas como metales de transición o tierras raras en la estructura de la BFO pueden realzar las propiedades ferroeléctricas y producir una débil respuesta ferromagnética. Por consiguiente, el presente estudio se basó en evaluar el efecto sobre las propiedades físicas de una sustitución de las especies de praseodimio en los sitios del Bi en la estructura de la BFO así como también la sustitución de los iones de cobalto en los sitios del hierro en esta misma estructura. El nivel del dopaje varió desde 0 at% hasta 4 at%, las películas delgadas de BFO se sintetizaron por el método de sol-gel y se usó glicol como un agente gelante

para incrementar la viscosidad en las soluciones precursoras y promover su adhesión sobre los sustratos de platino. La obtención de la estructura de la ferrita fue verificada con análisis de XRD para las muestras recocidas a 500ºC durante dos horas en aire, todas las muestras exhibieron una única fase correspondiente a BFO romboidal. El tamaño promedio del cristalito varió desde 28 nm a 40 nm y desde 28 nm a 31 nm para las películas dopadas con Praseodimio y Cobalto respectivamente, con un incremento en el nivel de los dopante. A su vez, las correspondientes coercitividades se incrementaron desde 166 Oe hasta 480 Oe en películas puras y dopadas con Pr al 4 at% respectivamente, y no se observó una variación en la coercitividad para las muestras dopadas con cobalto. En adición se observó un débil comportamiento ferroeléctrico con una predominante respuesta paraeléctrica en las muestras puras y dopadas en ambos sistemas.

DEDICATORY

To God, for his infinite love and care.

Dedicated to my loved mother Eugenia who is the most wonderful person in the world, Who took care of my studies and contributed in my professional development as well as her affection and love during happiness and sadness and to my brothers and sisters Elmo, Imelda, Amaranto, Maria, Juan, Norvil and Margot for their unconditional support, sacrifice, inspiration and love.

Este trabajo está dedicado a mi amada mamá, Eugenia, quien es la persona más maravillosa del mundo, quien se encargo de inducirme en el camino de educación además, por contribuir todo este tiempo en el desarrollo de mi vida profesional, así como el cariño y amor que me ha dado en los buenos y malos momento de mi vida, y a mis queridos hermanos Elmo, Imelda, Amaranto, María, Juan, Norvil y Margot por su incondicional apoyo, sacrificio, inspiración y amor.

ACKNOWLEDGMENTS

Special thanks to the University of Puerto Rico at Mayagüez for giving me the opportunity to develop as a student and researcher.

- Thanks to my advisor, Dr. Oscar Perales Perez for his support, guidance, motivation, scientific discussions, and the opportunity to work in his laboratory.
- Dr. Carlos Rinaldi for the SQUID measurements at UPRM.
- Thanks to Dr. Ram S. Katiyar, Ricardo Martínez and Danilo Barrionuevo, UPR-RP, for the ferroelectric measurement facility at UPR-RP.
- Special thanks to Dr. Maxime J-F Guinel, UPR-RP, for the SEM images at the IFN Nanospectroscopy Laboratory UPR-RP.
- Special thanks to Miss Gina Montes the collaboration in the $BiFeO_3$ research.
- Special thanks to M.S. Boris Rentería and PhD. Yarilyn Cedeño, UPRM, for the magnetic measurements at The NANO materials Processing Laboratory at UPRM.
- Special thanks to Miss Yesusa Collantes for helping in the English reviews of this thesis.
- I also want to acknowledge my friends and coworkers from the Nanomaterials Processing Laboratory.
- This material is based upon work supported by the DOE-Grant No FG02-08ER46526.

Table of Contents

Tables List

List of Figures

CHAPTER I. INTRODUCCTION

1.1 Motivation

The research and development of multifunctional nanomaterials and devices are receiving increased attention from both industry and academia. These materials can be designed to have integrated optical, electrical, piezoelectric, and magnetic properties, and possibly other functionalities. These materials have high potential for technology applications due to size, weight, cost, power consumption, and complexity as well as improving efficiency, safety, and versatility.

Zinc Oxide (ZnO) is a II-VI group compound semiconductor, having a hexagonal wurtzite structure with lattice parameters a=3.249 Å and c=5.207 Å. This semiconductor oxide has a direct band gap of 3.3 eV at room temperature and an excitation binding energy of 60 meV. ZnO doped with transition metals and rare earth ions, also known as diluted magnetic semiconductor (DMS), may exhibit a ferromagnetic behavior due to the effective incorporation of dopant species in the host oxide structure and the subsequent exchange interactions between available spins. This ferromagnetic functionality would enable doped ZnO to become a multifunctional material for applications in data storage and spintronics-based devices. DMSs materials have been the subject of diverse studies oriented towards the development of ZnO-based spintronic devices that would operate based on a quantum mechanical property of electrons called “spin” rather than on the electron’s electrical charge. The quantum properties of superposition and entanglement may someday permit quantum computers to perform certain types of computations much more quickly using less power than that required by conventional charge-based devices.

ZnO thin films have been synthesized by different techniques, including sputtering [1], chemical vapor deposition [2], pulsed laser deposition [3], and sol- gel process [4]. The sol-gel route is relatively simple, easy-to-scale and allows the synthesis of well crystallized powders and films. On this basis, this part of our research was focused on the development of a modified sol-gel technique where the film growth has been improved by proper selection of viscosity-controlling additives in the precursor sol for spin-coating. ZnO was doped with different transition metal ions (e.g., Co^{2+} and Sc^{3+}, V^{3+}) to study their structural, optical and magnetic properties as a function of the type and amount of dopant and the thermal treatment temperature and time. The dopants were chosen based on the size compatibility with Zn species in the host oxide lattice as well as the availability of *d*-electrons that would contribute with magnetic moments in the semiconductor host.

On the other hand, multiferroic materials which offer the possibility of manipulating their magnetic state by an electric field or viceversa are of current interest for a broad scope of applications including actuators, switches, magnetic field sensors, and new types of electronic memory devices. The term ‘‘*multiferroic*’’ indicates the coexistence of ferroelectric and magnetic ordering in one single phase [5]. Among different multiferroics candidates, $BiFeO_3$ is a non-centro symmetric rhombohedral perovskite transition metal oxide that crystallizes in the space group R3c with ‘*a*’ = 5.58Å [6]. This ferrite is expected to exhibit ferromagnetism, ferroelectricity, and ferroelasticity. Since the ability to couple to either the electric or the magnetic polarization would allow an additional degree of freedom in multiferroics-based device designs, the viability of tuning the multiferroic properties of $BiFeO_3$ by appropriate cationic substitutions would be desirable [7].

Although many efforts have been made to synthesize $BiFeO_3$, the main challenge has been the difficulty in avoiding the formation of parasite phases such as bismuth oxide or iron oxide. This impurity can be removed by leaching using dilute nitric acid. The removal of the impurity phases has been claimed; however, the method still lacks reproducibility [8]. Accordingly, the search of a synthesis approach that could lead to the direct formation of the $BiFeO_3$ structure, as nanocrystalline powders and thin films, becomes indispensable. On a functional basis, the challenge associated to the use of BFO is the high current leakage [9]. As an attempt to overcome this current leakage, without affecting the magnetic response of the material, the doping of the ferrite host with rare earths or transition metals was also evaluated. On this basis, this part of our work was addressed on the systematic study of the substrate-less synthesis of nanocrystalline BFO, both pure and Co- and Pr-doped, in acetic acid medium as well as the development of a novel route to produce thin films of the same material by a suitable selection of the solvent, spin-coating conditions and thermal treatment temperatures. Co^{2+} ions were used as doping species since they contribute with magnetic moments to the system, increasing its magnetic properties. In turn, Pr-doping in BFO could cause a reduction in oxygen vacancies that would affect the corresponding ferroelectric properties.

Produced powders and films allowed a systematic study of the relationship between synthesis conditions and structure, composition dopant levels of the corresponding functional properties.

1.2 Aim of study

1.2.1 Main objective

Investigate the dependence of optical, magnetic and ferroelectric properties in multifunctional ZnO- and $BiFeO_3$-based nanostructured powders and thin films with of average crystallite size and composition dopant levels.

1.2.2 Specific objectives

A. - Determine the optimum condition to synthesize pure and doped (Co, Sc, and V ions) ZnO and (Co and Pr ions) BFO powders and thin films via a modified sol- gel method.

B. - Determine the effect of type and concentration of dopant species on the optical and magnetic properties in ZnO-based DMS at room temperature.

C. - Determine the effect of type and concentration of dopant species on the ferromagnetic and ferroelectric properties in BFO-based Multiferroic.

D. - Discuss and propose mechanisms involved with the functional properties attained in pure and doped systems.

1.3 Contents of the thesis

An overview of the content of this thesis is as follows. Chapter II consists of a background on ZnO-based DMS and the theoretical predictions of ferromagnetic behavior at room temperature, and background on BFO structural magnetic and electric properties. Chapter III in an updated review of previous related work on ZnO based DMS systems and BFO multiferroics. Chapter IV details the experimental procedures as well as the characterization of the ZnO and BFO samples (nanocrystalline powders and films). Chapter V is focused on results, discussion and

interpretation of our obtained results. Finally, Chapter VI summarizes the main conclusions of our research.

CHAPTER II: BACKGROUND

2.1 Multifunctional Materials and Systems

2.1.1 Introduction

In recent years there has been an increased interest on the study of materials that are capable of combining different electrical, optical, magnetic, mechanical, thermal, chemical properties, and low weight, which are desirable in material systems. In order to produce a material with these features it is necessary to understand the mechanisms and processes that occur at the micro and nano scale. Development of this new generation of multifunctional materials requires design and fabrication at the nanoscale to obtain a high performance. These materials can possess novel properties including the ability to recognize shape or sense changes in the environment and can respond to more than one type of stimulus.

These materials have a great potential to enhance future structural performance by reducing size, weight, cost, power consumption, and complexity while improving efficiency, safety, and versatility; and can find several applications in medical implants, miniature energy storage devices, display devices, spintronics, and data storage. Possible candidates with these features and multifunctional applications are metals, semiconductors, superconductors, polymers, multiferroics, etc.

2.1.2 DMSs and Spintronics Materials

The DMSs have been studied for several decades due to their important properties that researchers have discovered. The DMS novel magnetic properties are combined with their semiconducting intrinsic properties to become materials with multiple applications in science

and technology. These new magnetic properties are generated mainly by interchange between the non-magnetic ions and magnetic ions (transition metals or rare earths). These magnetic ions produce localized magnetic moments in the semiconductor host. Magnetic ions are sited randomly in the semiconductor host, having an incomplete (3*d* or 4*f*) electron shell. These ions generate interchange interactions that usually occur with its nearest neighbors. These interactions produce drastic changes in the semiconductor physical properties and also promote a magnetic behavior.

The first transition metal used as dopant was Mn on IV-VI, II-VI, II-V and III-V compound semiconductors based DMSs, for example, IV-VI: (Sn,Mn)Te, (Pb,Mn)Te; II-VI: (Zn,Mn)Se, (Cd,Mn)Se, (Cd,Mn)Te. In these DMSs the magnetic interaction is dominated by the antiferromagnetic exchange among the Mn spins, which results in the paramagnetic, antiferromagnetic, or spin-glass behavior of the compound and III-V: (InMn)As and (GaMn)As. Figure1 shows a schematic of a non-magnetic material, a DMS material and a magnetic material.

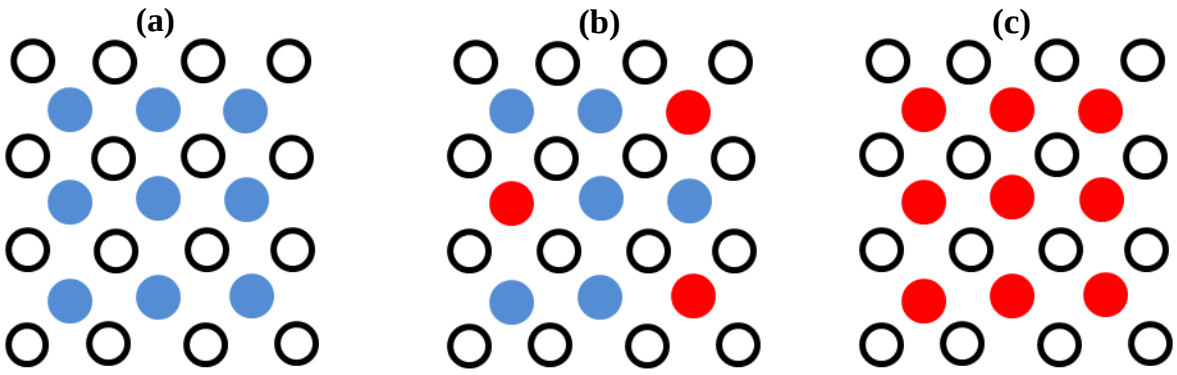

Figure 1. (a) Schematic of a non-magnetic semiconductor. This matrix has non-magnetic cations (blue) and anions (white); (b) a diluted magnetic semiconductor, some of the non-magnetic cations have been replaced by magnetic cations (red), (c) Magnetic Material.

The Mn-doped GaAs semiconductor generated great expectation due to its magnetic behavior, with a Curie temperature of 110K [10]. This fact makes a big challenge to researchers to find magnetic properties at room temperature in GaAs- based DMS, but the highest Curie temperature obtained in this system was 172 K [11].

Then the favorites for research became ZnO and GaN semiconductors based DMSs, due to a reported theoretical work by T. Dietl *et al.* [12]. These researchers explained that magnetic behavior is caused by the effect of the amount of holes that there are in a given volume of material. In addition, they also determined the values of T_C for various semiconductors containing 5% of Mn and $3.5x10^{20}$ holes per cm^3, as shown in Figure 2**.**

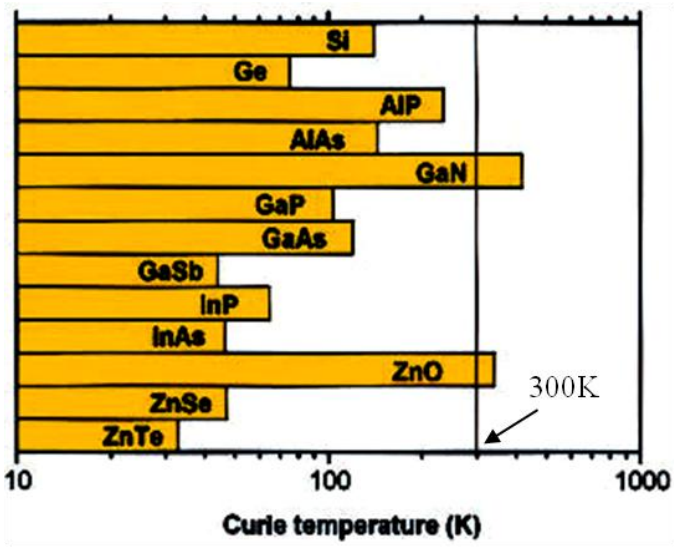

Figure 2. Computed values of the Curie temperature T_C for various p-type semiconductors containing 5% of Mn and $3.5x10^{20}$ holes per cm^3 as reported in [12]

Nowadays it is still not well understood the ferromagnetic behavior in these solids. Several mechanisms were proposed such as direct exchange interaction where the direct coupling of spins through overlap of magnetic orbital could generate an antiferromagnetic configuration,

indirect exchange interaction where the incomplete shell *d* spins and the spins of the conduction band electrons are strongly couple could generate a ferromagnetic behavior. Furthermore indirect spin coupling, known as super-exchange interaction, is possible even in the presence of non magnetic ion. Also, DMSs magnetic properties can be explained through double-exchange mechanism proposed by Zener [13], Ruderman–Kittel–Kasuya–Yoshida (RKKY)- type interactions [14,15], and bound magnetic polarons [16,17].

2.1.2.1 Theories of Magnetism for DMSs

Double Exchange Interaction

Zener proposed [13] the double exchange interaction model to explain the mixed-valence manganites which can produce large moments, but also to explain nearest- neighbor interaction that requires mixed cation valence of transition metals, where $3d^n \leftrightarrow 3d^{n+1}$ configuration fluctuations can be produced. The mechanism is based on the coupling of magnetic ions with different charge states by virtual hopping of the extra electron from one ion to the other, for example in the transition metal Mn^{2+}-Mn^{3+} (or d^4– d^5) pair of ions, where one d electron can hop virtually from one ion to another via the p-orbitals of neighboring anions. The double exchange is not suitable to explain the ferromagnetic correlation between distant Mn spins, since the magnetic electrons remain localized and do not contribute to the charge transport. In this case Matsukura *et al*. [18] proposed that the holes in the extended or weakly localized states mediate the long range interactions between the localized spins.

Some works suggest that the existence of the mixed valence of Mn in doped ZnO lead the double exchange interaction. This mechanism occurs in a DMS if the neighboring TM magnetic moments are in the same direction so the *d*-band is widened by the hybridization between the up-

spin states. Besides, in the ferromagnetic configuration the addition of carriers in the *d* band lowers the band energy. When this happens the 3*d* electron in the partially occupied 3*d*-orbitals are allowed to hop towards the 3*d*-orbitals of the neighboring TM if the magnetic moments of the neighboring TM are parallel. The result is a lower kinetic energy for the d-electron due to the hopping in the ferromagnetic state.

The Ruderman–Kittel–Kasuya–Yoshida (RKKY) Model

The RKKY mechanism was originally proposed to explain interactions between nuclear spins in metals via the conduction electrons and resulted suitable only when a high concentration of free carriers is present. There were attempts to use this mechanism to explain the magnetic behavior of DMSs where two local magnetic ions over relatively large distance interact via RKKY interactions.

RKKY interaction is based on the exchange coupling between the magnetic ion and the band electrons through the *s–d* Kondo Hamiltonian. This can be analyzed as a first order perturbation effect. Therefore, in a perfect one electron system in a cubic semiconductor this mechanism would not lead to any effect since the *s* and *d* wave-functions are orthogonal. Conduction electrons are magnetized in the neighborhood of a magnetic ion, the polarization of conduction electrons depends on the distance from the magnetic ion an oscillatory way. This oscillation produces an indirect interaction (RKKY) between the two magnetic ions on the nearest or the next nearest magnetic neighbors. This coupling could result in a ferromagnetic (parallel) or an antiferromagnetic (antiparallel) setting of the moments dependent on the distance of the interacting atoms. Although this mechanism is not suitable to explain ion–ion interactions in DMSs, it is the basis for the carrier-mediated inter-ionic spin interactions in metals and highly degenerate semiconductors.

The Mean-Field Zener Model

Dietl *et al.* [12] proposed the mean-field Zener model which is based on the original model proposed by Zener [13] and the RKKY interaction. Dietl *et al.* explained that ferromagnetic coupling between localized spins of TM ions in doped semiconductor is through the holes originating from shallow acceptors. Moreover they suggested that the holes in the extended or weakly localized states mediate the long-range interactions between the localized spins on both sides of the metal-insulator transition in the III-V and II-VI magnetic semiconductors. In addition they computed the Curie temperature the results are shown in Figure 2. The data demonstrated that there is a large range to increase T_C in most of *p*-type magnetic semiconductors. In particular, a general tendency for greater T_C values in the case of lighter elements stems from the corresponding increase in *p-d* hybridization and reduction of spin-orbit coupling. The results obtained by Dietl reveal the important effect of the spin-orbit coupling in the valence band in determining the magnitude of the T_C and the direction of the easy axis in *p*-type ferromagnetic semiconductors.

Theoretical approximation for electronic structure in DMS

Sato and Katayama-Yoshida [19] studied the ferromagnetic behavior in DMSs as a disordered system, because the magnetic ions are randomly substituted in the principal host of a material.

The calculation methods based on ordinary band theory cannot be used in disordered systems because they are based on the assumption of periodic boundary conditions. The procedure to overcome this difficulty was the introduction of a regular arrangement of impurities in the crystal, neglecting randomness. Over this regular arrangement of impurities a large unit cell, so-called super-cell was constructed, which contains the magnetic ions. Then the corresponding

band structures were calculated for this new super-cell. This super-cell method is frequently used in the calculation of electronic band structure of disordered systems [19].

Sato and Katayama described the DMSs without neglecting the ramdomness using the coherent potential approximation (CPA) instead of the super-cell method.

Sato and Yoshida performed theorethical calculations considering 3*d* TM-doped semiconductors among these TM-doped ZnO based DMS. In general, the 3*d* dopant states usually presented a large hybridization with the conduction band of the semiconductor. However the large exchange splitting of 3*d*-states produce an "almost saturated" magnetic moment. In this case, there are two directions of magnetic moment along the quantization axis originating two self-consistent solutions for the electronic structure of the DMS. These solutions are the ferromagnetic state and the spin-glass state.

The ferromagnetic state, which is described as $(Zn_{1-x},TM_x(\uparrow),O)$ for a ZnO-based DMS, presents a finite magnetization. Since the magnetic moments of all TM atoms are parallel. In the spin glass state, which is described as $(Zn_{1-x},TM_{x/2}(\uparrow),TM_{x/2}(\downarrow),O)$, magnetization is zero since magnetic moments of TM atoms point randomly with respect to each other. Comparing the total energy of both states, it is possible to recognize the ground state. The ferromagnetism in DMS is a consequence of a competition between the ferromagnetic state and the spin-glass state, and the magnetic properties of DMS can be controlled by changing the carrier density (electrons or holes). The stability of the ferromagnetic state in the case of ZnO and GaN calculated by Sato and Katayama-Yoshida is shown in Figure 3.

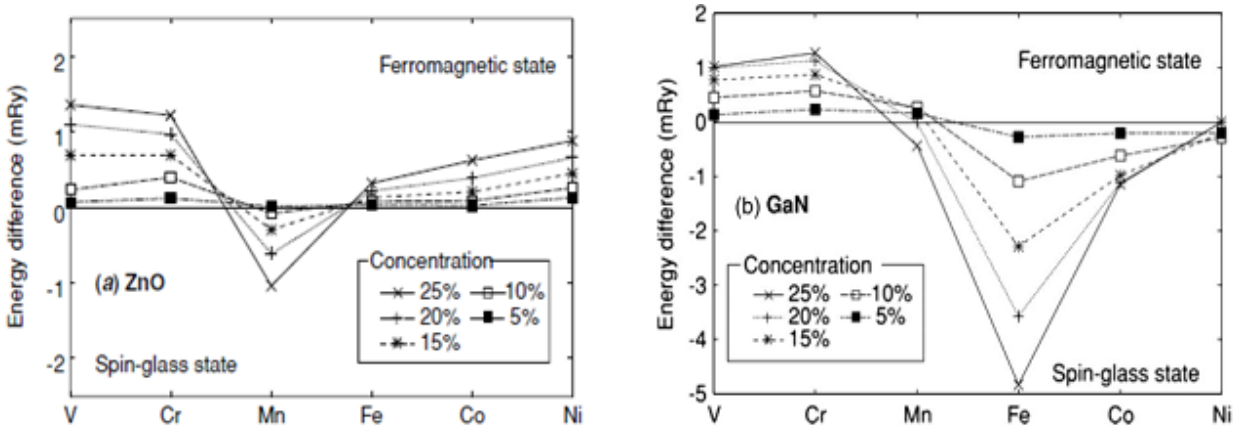

Figure 3. Stability of the ferromagnetic states in (a) ZnO- and (b) GaN-based DMSs. The vertical axis is the energy difference per formula unit between the ferromagnetic state and the spin-glass state. A positive energy difference indicates that the ferromagnetic state is more stable than the spin-glass state [19]

Magnetic Polarons

The ferromagnetic behavior of doped semiconductors with low percentages of magnetic ions cannot be attributed to the superexchange or double-exchange interactions, since these interactions do not produce long-range magnetic order at very low concentrations of dopants. Consequently Coey *et al.* [17] proposed for such cases that the ferromagnetism is mediated by shallow donor electrons that form bound magnetic polarons, which overlap to create a spin-split impurity band. For example the ferromagnetic ordering of Mn moments may be arisen from carriers (holes) presents in the material, but localized at the TM. In the Figure 4 is shown a representation of the bound magnetic polarons. A bound magnetic polaron is a localized hole. The localized holes act on the TM surrounding them and generating an effective magnetic field that aligns all the spins. Below the T_C, the neighboring magnetic polarons overlap and interact via TM forming correlated clusters of polarons. Then the ferromagnetic transition occurs when the size of the cluster is the same to the size of the sample. This model is applicable to few percent dopants in DMSs of both *p*- and *n*-types. Although the direct exchange interaction of

localized holes is antiferromagnetic, the interaction between bound magnetic polarons may be ferromagnetic at sufficiently large concentration of dopants.

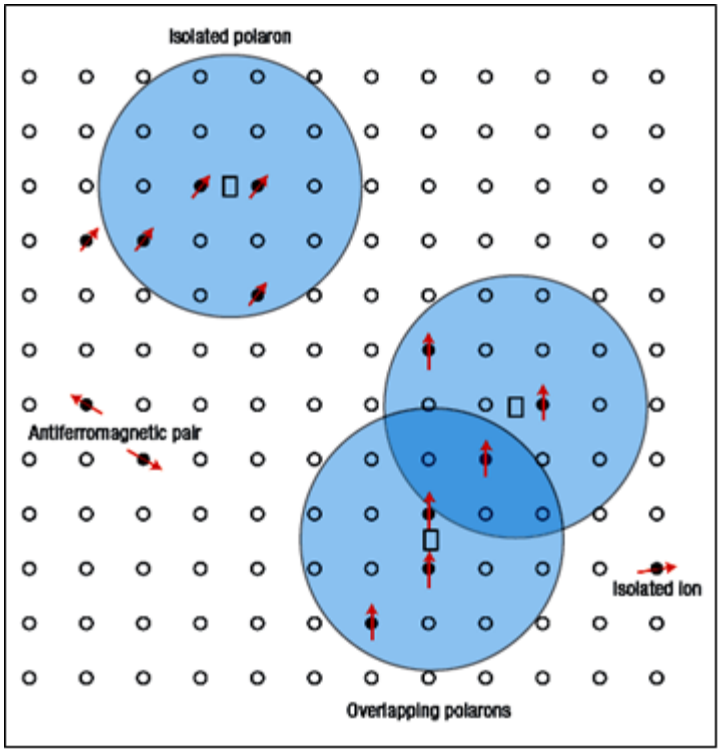

Figure 4. Representation of magnetic polarons, a donor electron in its hydrogenic orbit couples with its spin antiparallel to impurities with a 3*d* shell that is half-full or more than half-full. Cations sites are represented by small circles. Oxygen is not shown; the unoccupied oxygen sites are represented by squares [17].

One the challenge is to understand the new magnetic properties of DMSs, since these materials are excellent candidates for applications in science and technology, as Spintronic (spin electronic transport). This new technology has generated great expectations for the new generation of devices. Spintronics is based on the electron spins that carry information, with the manipulation of spin degrees of freedom in solid could be controllable the behavior of the spins (up or down) of a collection of particles, this could add considerably more capability and performance to electronic devices. The devices have many advantages such as non-volatility, increased data

processing speed, decreased electric power consumption, and increased integration densities compared to semiconductor devices. So far several types of devices with spin manipulation have been proposed such as, spin field-effect transistor, spin LEDs, spin resonant tunneling device, optical switches operating at terahertz frequency, modulators, quantum computation and communications [20-24].

2.1.2.2 ZnO- Based Dilute Magnetic Semiconductors

There are several types of semiconductors, but ZnO and GaN based DMSs are the most researched, because they have a Curie temperature above room temperature, and therefore are very attractive materials for spintronic applications. ZnO is the most attractive due to its larger exciton binding energy, ~ 60 meV, compared to GaN ~ 25 meV; the higher exciton binding energy enhances the luminescence efficiency of light emission. Electron Hall mobility in single crystal ZnO is ~ 200 $cm^2 V^{-1}$, slightly lower than that of GaN at room temperature, but ZnO has higher saturation velocity. ZnO has exhibited better radiation resistance than GaN, useful for possible space and nuclear applications. Furthermore ZnO has many promising properties for application such as blue/UV optoelectronics, transparent electronics, facial powders, sunscreens, paint pigmentation, catalysts, lubricant additives, piezoelectric transducers, varistors, and also medicine.

ZnO Crystal structure

ZnO is a compound of the group II-VI semiconductor type; this compound has three phases, hexagonal wurtzite structure (B4), Zinc blende (B3) and rock salt structure (B1). Wurtzite phase is thermodynamically stable under environmental conditions of pressure and temperature, Zinc

blende is stable only by growth on cubic substrates. The rock salt structure can be obtained at relatively high pressures. These three phases are schematically shown in Figure 5. In the hexagonal wurtzite structure, each anion (oxygen) is surrounded by four cations (Zinc) at the corners forming a tetrahedron, and vice versa. The tetrahedral coordination of ZnO is typical of sp^3 covalent bonding; furthermore the electronegative difference between Zinc and Oxygen in this compound produced strong ionic bond. ZnO lies on the borderline between covalent and ionic semiconductor. The wurtzite structure belongs to the space group of C^4_{6V} or $P6_3mc$ and its hexagonal unit cell has two lattice parameter (a= 3.249Å and c=5.207Å) [25], as shown in Figure 6.

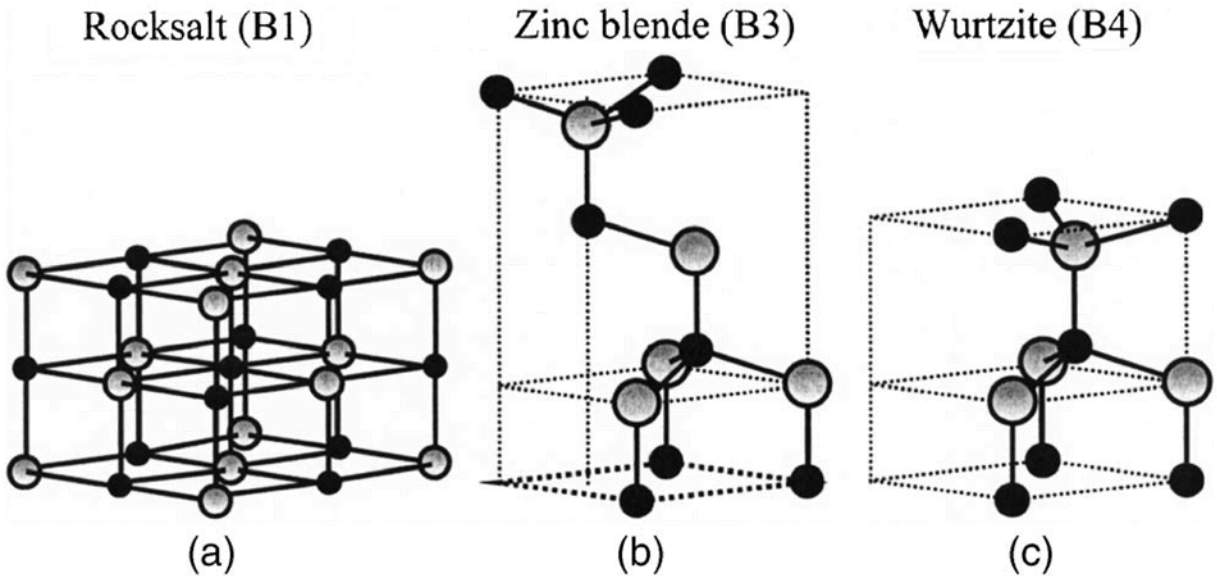

Figure 5. ZnO crystal structures: (a) cubic rocksalt (*B*1), (b) cubic zinc blende (*B*3), and (c) hexagonal wurtzite (*B*4). The shaded gray and black spheres denote Zn and O atoms, respectively [25].

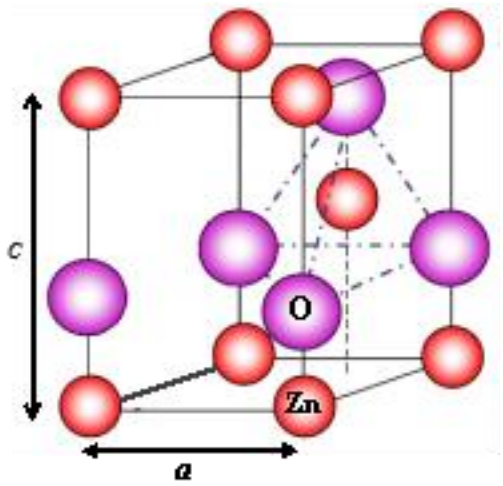

Figure 6. The ZnO hexagonal unit cell has two lattice parameters: *a*= 3.249Å and *c*=5.207Å

ZnO Electronic band structure

Knowledge of the band structure in a semiconductor is important because this will provide the necessary information to consider if this material can be useful for device applications. There are several theoretical methods to determine the band structure of solids such as Local Density Approximation (LDA) and Linear Combination of Atomic Orbitals (LCAO) Hartree-Fock; experimental methods are also used. To measure the electronic core levels in solids, UV (emission, reflection or absorbance) or X-ray techniques are used. These methods measure the difference in energy of electronic level transitions; i.e., transitions from the valence band to the conduction band. Several methods have been used in the study of ZnO band structure, but the most demanded method is LDA [26–28] because this method takes into account the cationic *d* electrons in calculations. When the *d* electrons are considered as core electrons, the calculated lattice constant is lower than the experimental values by 18% for wurtzite ZnO; if the *d* electrons are included in the valence band, very accurate lattice constants are obtained. Even when the *d* electrons have been properly taken into account, the results of standard LDA calculations show a

strongly underestimated band gap and overestimated occupied cationic *d* bands. Furthermore, interactions with the anion *p* valence bands are artificially enlarged, resulting in overestimated dispersion and bandwidth of the latter, shifting them close to the conduction bands. For example, the ZnO band gap calculation using LDA was 0.23 eV, which is not in a good agreement with the experimental value 3.37 eV. Zakharov *et al.* [29] also reported plane-wave *GW* method for some II-VI compounds, the *d* electrons were considered as core electrons and deliberately carried out their *GW* calculation at the experimental lattice constants. The results for the anion *p* valence bands and for the band-gap energies were consistent with experiments, but there was no agreement in the *d*-band positions. Vogel *et al.* [30] proposed to incorporate dominant self-interaction corrections to LDA in the study of band structure of II-VI semiconductor compounds. Figure 7 shows ZnO band structure calculations by standard LDA (a) and self-interaction corrected pseudo-potential approach included in the LDA (b).

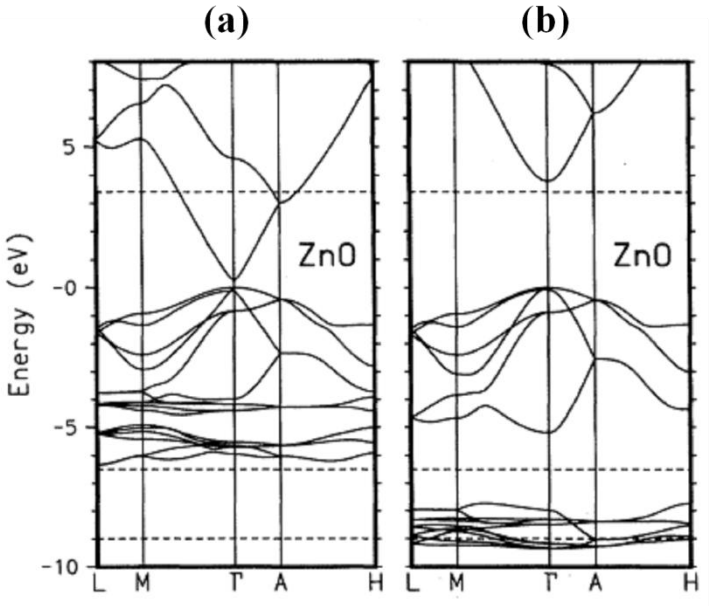

Figure 7. ZnO band structure calculations by standard LDA (a) and self-interaction corrected pseudo-potential approach included in the LDA (b) [30].

Magnetic Properties in ZnO based DMS

The ferromagnetic behavior in ZnO doped with TM could be attributed to interactions between the local moments of the TM atoms, which are mediated by free carriers in the material, and the spin-spin coupling is assumed as a long-range interaction. This is why a mean-field approximation can be used. Ferromagnetic behavior may also be attributed to the super exchange interaction through oxygen (TM-O^{2-}-TM), or the exchange interaction between spins of the band carriers and localized spin of TM. However, there is not a general theory that can explain these magnetic properties in ZnO based DMS. Further magnetic properties depend of the growth conditions used to DMS material.

This work presents the calculation of the effective contribution (μ_{eff}) to the saturation magnetization per magnetic ion of the utilized dopants: Cobalt, Scandium and Vanadium.

For this purpose the quantum numbers ***J, S***, ***L***, representing the total angular momentum, total spin momentum, and total orbital angular moment, respectively, are needed. Using Hund's rules:

First rule: ***S*** must be maximum by Pauli Exclusion Principle, to get the lower repulsion energy.

Second rule: ***L*** must be maximum consistent with the value of *S*.

Third rule: $J = |L\text{-}S|$ when *d* shell is less than half full and $J=L+S$ when *d* shell is more than half full.

Co^{2+} ions: Electronic configuration (Co^{2+}[Ar]$3d^7$,$4s^0$), using Hund's rules fill the electrons in the *d* shell:

Co^{2+}: *d* 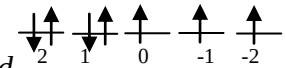

shell.

The total spin moment is the sum of the spins of all the electrons in the *d*-shell:

S=1/2+1/2+1/2= 3/2

The total orbital angular momentum is the sum of the angular momentum of each electron in the *d* shell:

L= 2+1+0-1-2+2+1=3

The total angular momentum according to the third Hund's rule is:

$J=L+S=3+3/2=9/2$

Then there are $2J+1 = 10$ possible projections of the total angular momentum according to:

$$-J \le m_J \le J$$

In our case: $-9/2 \le m_J \le 9/2$

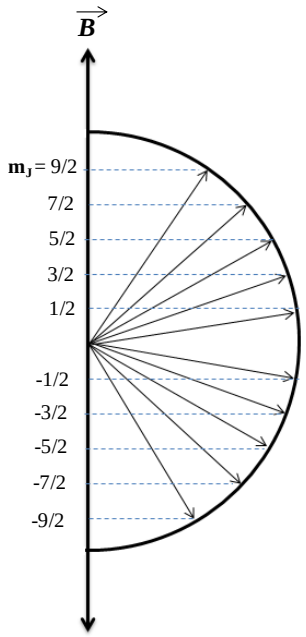

Figure 8. Possible projections of the total momentum *J* onto the direction of the magnetic field *B* of the Co^{2+} ion

The projection of the effective magnetic moment onto the *z*- direction, magnetic field direction

$$(\mu_{eff})_z = -g\mu_B m_J$$

where g is the Landé-factor, μ_B is the Bohr magneton and m_J must be one of the ten values above.

Calculating the Landé-factor:

$$g = \frac{3}{2} + \frac{S(S+1) - L(L+1)}{2J(J+1)}$$

Using the values of *S*, *L* and *J* obtained for Co^{2+} ion, the values of the Landé-factor is $g = 4/3$.

So the maximum value of the effective moment in the direction of the magnetic field will be when $m_J = -9/2$ and then $(\mu_{eff})_z = 6\mu_B$

V^{3+} ions: Electronic configuration (V^{3+}[Ar]$3d^2$,$4s^0$), using the Hund's rules to fill the electrons in the *d* shell.

V^{3+}: *d* 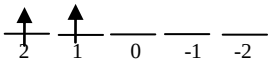

shell.

Total spin momentum: $S = 1/2+1/2 = 1$

Total orbital angular momentum: $L = 2+1 = 3$

Total angular momentum using the Hund's rules when *d* shell is less than half full.

$J = |L-S| = 2$

Then there are $2J+1 = 5$ possible projections of the total angular momentum in the direction of the magnetic field: $-2 \le m_J \le 2$

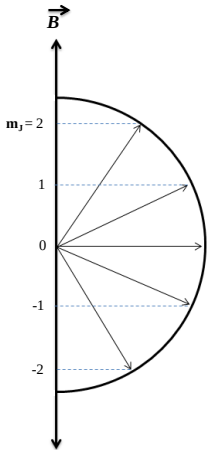

Figure 9. Possible projections of the total momentum *J* onto the direction of the magnetic field *B* of the V^{3+} ion.

To determine $(\mu_{\text{eff}})_z$ the Landé-factor was calculated in the same way as in the previous case, g=2/3. Then the maximum possible value of the effective moment onto the direction of the magnetic field will be when m_J = -2; $(\mu_{eff})_z = 4/3\mu_B$

For the case of Sc^{3+}, this ion will not have magnetic contribution since its shell is empty (Sc^{3+}[Ar]$3d^0$,$4s^0$), then S=0, L=0 and J= 0, the weak ferromagnetic contribution can be attributed to others mechanisms such as superficial defects or magnetic polarons.

2.1.3 Multiferroics

A compound has multiferroic features when it presents more than one "*ferroic"* property simultaneously in a single phase [31]. These properties are ferromagnetic, ferroelectric, ferroelastic, as shown in Figure 10. Coupling occurs in these properties, for instance magnetic and electrical properties. These types of compounds have become a boom today in the research world, due to their promising features as transducers, magnetic field sensors, and also in high performance storage devices.

Coupling could give attractive functionalities, such as permitting data be written electrically and read magnetically. This would develop the best features of ferroelectric random access memory (FeRAM) and magnetic data storage, while avoiding problems related with reading FeRAM and production of large local magnetic fields needed to write.

There are many materials that present this ferroic property, but the most investigated ones are perovskite structures. This group also includes bismuth compounds $BiFeO_3$ and $BiMnO_3$.

In addition is these ferroic materials, rare-earth manganites and ferrites (e.g. $TbMnO_3$, $HoMn_2O_5$, $LuFe_2O_4$), and non-oxides and spinel chalcogenides are included.

Materials with perovskite structure have an arrangement ABO_3 [32] as shown in Figure 11. Cations A (Pb^{2+}, Bi^{3+}, Tl^{+},…) are responsible for the ferroelectric behavior due to the fact that these ions have a sterochemically active unshared pair of 6s-electrons and cations B (Ti^{4+}, Zr^{4+}, Nb^{5+}, W^{6+}, Mo^{6+}, Fe^{3+},…) which produce ferromagnetic behavior. The exchange interaction of the electron spins produces the magnetic behavior and the redistribution of charge density in the lattice produces the ferroelectric behavior. Multiferroics also present the magnetoelectric effect: in an electric field it is possible to induce magnetization and in a magnetic field it is possible to induce polarization.

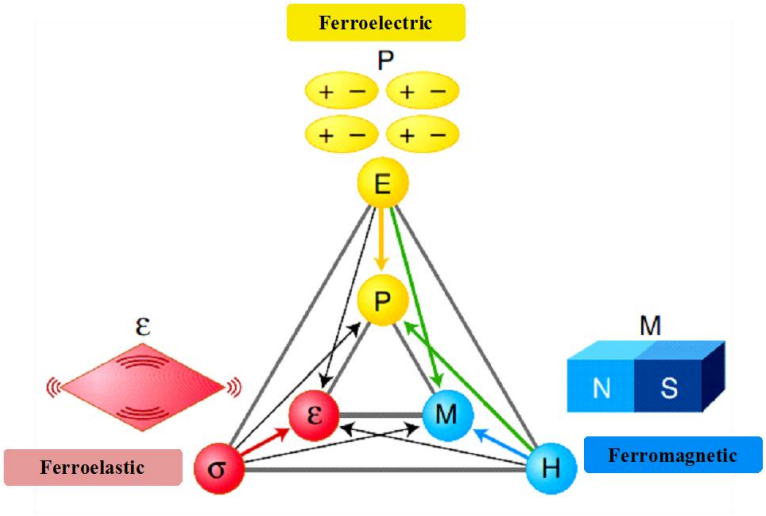

Figure 10. Phase control in multiferroic, the electric field *E*, magnetic field *H*, and stress *σ* control the electric polarization *P*, magnetization *M*, and strain *ε*, respectively. In a ferroic material, *P*, *M*, or *ε* are spontaneously formed to produce ferromagnetism, ferroelectricity, or ferroelasticity, respectively. In a multiferroic, the coexistence of at least two ferroic forms of ordering leads to additional interactions [33].

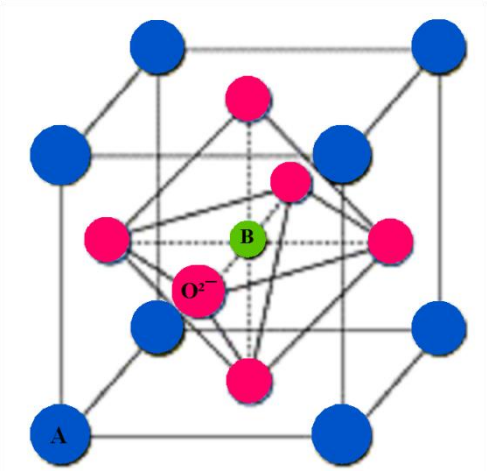

Figure 11. The ideal unit cell of perovskite ABO_3. The B ion lies at the center of the cube and the oxygen ions at the centers of the faces.

Ferromagnetic Effect

In a ferromagnetic material its electrons have a net angular momentum. This momentum can be originated from either the orbital component or the spin component, or both. The quantum mechanical exchange energy aligns spins parallel, producing different amounts of up and down spin electrons. The exchange energy in solids is the energy difference per magnetic ion between ferro and antiferromagnetic order arrangements. The ferromagnetism can be explained by two phenomenological theories, localized moment theory of Curie-Weiss and the Stoner band theory [34, 35].

In the Curie-Weiss theory, a ferromagnetic material presents local magnetic moment on the ions at all temperatures, the ferromagnets have two phases related with temperature, below the T_C the magnetic moments align parallel to each other, through an internal molecular field which is so strong that it magnetizes the material even in absence of an external applied field (spontaneous magnetization), originating a ferromagnetic state. Above the T_C the magnetic moments are disordered by thermal energy kT, and the effects associated with entropy resulting in a

paramagnetic state with no net magnetization. This theory has limitations to explain the ferromagnetic behavior in metals. For example the magnetic dipole moment on each atom or ion should be the same in both the ferromagnetic and paramagnetic phases. Experimentally this is not observed, and furthermore the magnetic dipole moment on each atom or ion should correspond to an integer number of electrons, which is not observed either.

Stoner band theory, on the other hand, is a better approach for metals. It is also based on the exchange energy: this energy is minimized if all the electrons have the same spin. Above T_C the material has the same number of up and down spin electrons, consequently there is no magnetic moment and below T_C exist a net magnetic moment because the up and down spin bands have different numbers of electrons.

In magnetic transition metals such as Fe, Ni and Co, there is a region of overlapping in the 3*d* and 4*s* bands at Fermi level. In this level the 4*s* bands are broad and have a low density of states. Furthermore the energy that is needed to promote a 4*s* electron into a vacant state is high so the 4*s* bands are not spin polarized. The 3*d* band is narrow and has a much higher density of states at the Fermi level. As there are many electrons near the Fermi level, the band energy required to reverse a spin is reduced, and therefore the exchange effect dominates. This exchange interaction produces a shift in the energy of the 3*d* band for electrons with one spin direction with respect to the band for electrons with the opposite spin direction, producing the exchange-split band structure [35].

In addition, there are other types of magnetic ordering such as antiferromagnetism and ferrimagnetism, these arrangements usually possess super exchange interactions, which are produced through non-magnetic ions (oxygen ions) by chemical-bonding.

Ferroelectric Effect

A ferroelectric material presents two phases related with temperature, at high temperatures it behaves as an ordinary dielectric, where an electric polarization $\boldsymbol{P}$ is induced by an external electric field $\boldsymbol{E}$, and at low temperatures has a spontaneous polarization, the direction of polarization can be switched by an external electric field. These materials possess domains and in an external electric field show a hysteretic response of both polarization and electric displacement $\boldsymbol{D}$. When the temperature of a ferroelectric tends to T_C the spontaneous *electric* polarization begins, which coincides with a divergence in the static *dielectric* permeability $\boldsymbol{\epsilon}$. Hence a small external electric field causes a large polarization.

The ferroelectricity is determined by a balance between the short-range repulsions of neighbor electron clouds and the bonding forces [35]. These short-range repulsions are in favor of a nonferroelectric symmetric structure and bonding forces might stabilize the ferroelectric phase.

Dipole moments are formed as a result of the relative displacement of anions and cations, prerequisite for ferroelectricity. A material must have a non-centrosymmetric arrangement of ions to exhibit spontaneous electric polarization. The ferroelectric ground-state is understood as a set of small atomic displacements from the centrosymmetric paraelectric phase.

Ferroelectric effect is observed in materials having a perovskite structure; this crystal structure is shown in Figure11 and Figure 12(a) (top view of a periodic array), the atoms represented by blue and green spheres are the cations and the pink atoms are the oxygen ions. The oxygen ions exert an electrostatic force on the cations, causing distortion of the crystal structure, this generates the electrical polarization in the material shown in Figure 12(b).

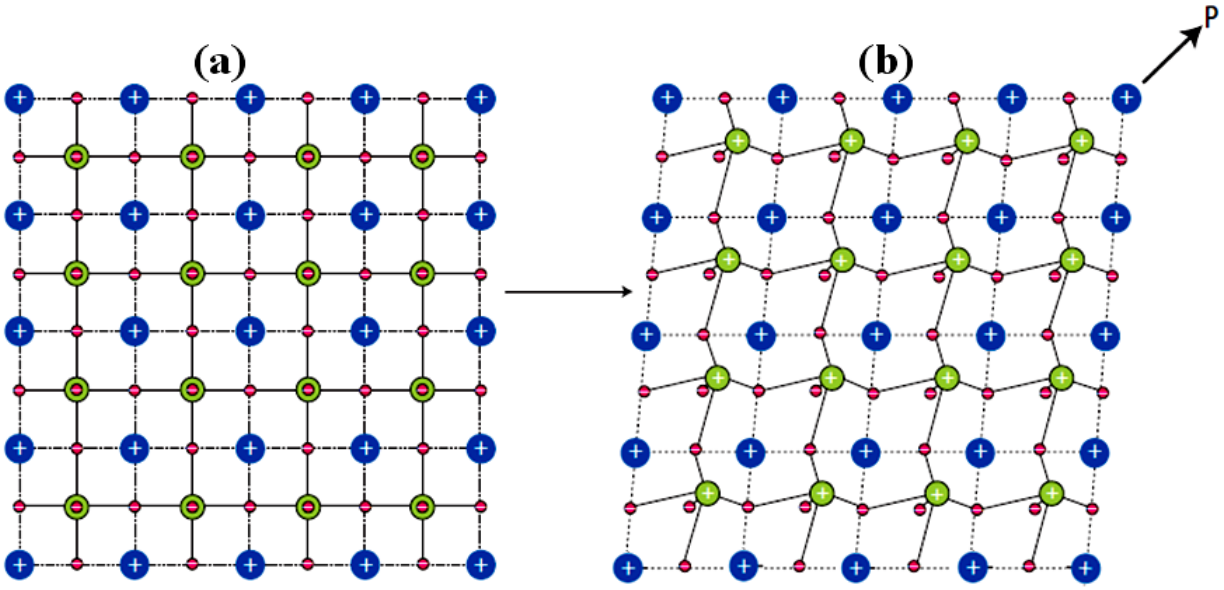

Figure 12. Ferroelectricity in typical perovskite manganites, such as $BaTiO_3$ the green Ti ion is shifted away from its position in the centre of the (pink) oxygen octahedral. This creates a ferroelectric polarization (P), but is incompatible with any spontaneous magnetic moment [36].

Piezoelectric Effect

All materials that present ferroelectricity are also piezoelectric, but not all piezoelectric are ferroelectric. Materials under mechanical stress or strain produce a reordering of the electric dipoles and as consequence occurs a spontaneous change in the charge polarization. Using a formal description the piezoelectric effect can be expressed, in the following equations:

$$\boldsymbol{D = \epsilon_T E + d_{33} T}$$

$$\boldsymbol{S = d_{33} E + s_E T}$$

where $\boldsymbol{T}$ and $\boldsymbol{S}$ represents stress and strain respectively, as well as $\boldsymbol{\epsilon_T}$ is the dielectric constant, $\boldsymbol{d_{33}}$ is the piezoelectric constant, and $\boldsymbol{s_E}$ is the material's compliance in the presence of a constant electric field. Electric displacement $\boldsymbol{D}$ and material's electric field have a direct dependence with stress and strain. In addition these relations describe the converse piezoelectric effect. This effect

occurs when a material physically changes shape in an external electric field $\boldsymbol{E}$. The increase in $\boldsymbol{T}$ and $\boldsymbol{S}$ on the material due to the change in the external electric field produces an altered shape.

Figures 13(a) and 13(b) show a scheme of the piezoelectric effect. Green spheres represent the cations and yellow spheres denote the anions. These materials possess an intrinsic polarization P_0 due to their lattice structure, as shown in Figure 13(a). When a material suffers mechanical stress the charge distribution within is altered producing a new polarization $\boldsymbol{P_f}$ as shown in Figure 13(b). So this can be written as:

$$\boldsymbol{P_f = P_0 + \Delta P}$$

The converse piezoelectric effect arises when an external electric field is applied, for example in the *z* axis direction as shown in Figure 13(c) y 13(d) represented in violet arrows. A shift occurs in the ions, cations in the applied field direction and anions in the opposite direction, producing a distortion in the physical shape of the piezocrystal, as can be seen in Figure 13(d). In general this distortion can be expressed:

$$x_f,y_f,z_f = x_0,y_0,z_0 + \Delta x,\Delta y,\Delta z$$

Ferroelectric materials always present the piezoelectric effect below the Curie temperature, since above this temperature the material does not exhibit net electric polarization. The piezoelectric effect is widely used in several applications since the crystal motion resulting from the applied electric field is both predictable and precise. Several materials with perovskite structure present piezoelectric effect one is the BFO.

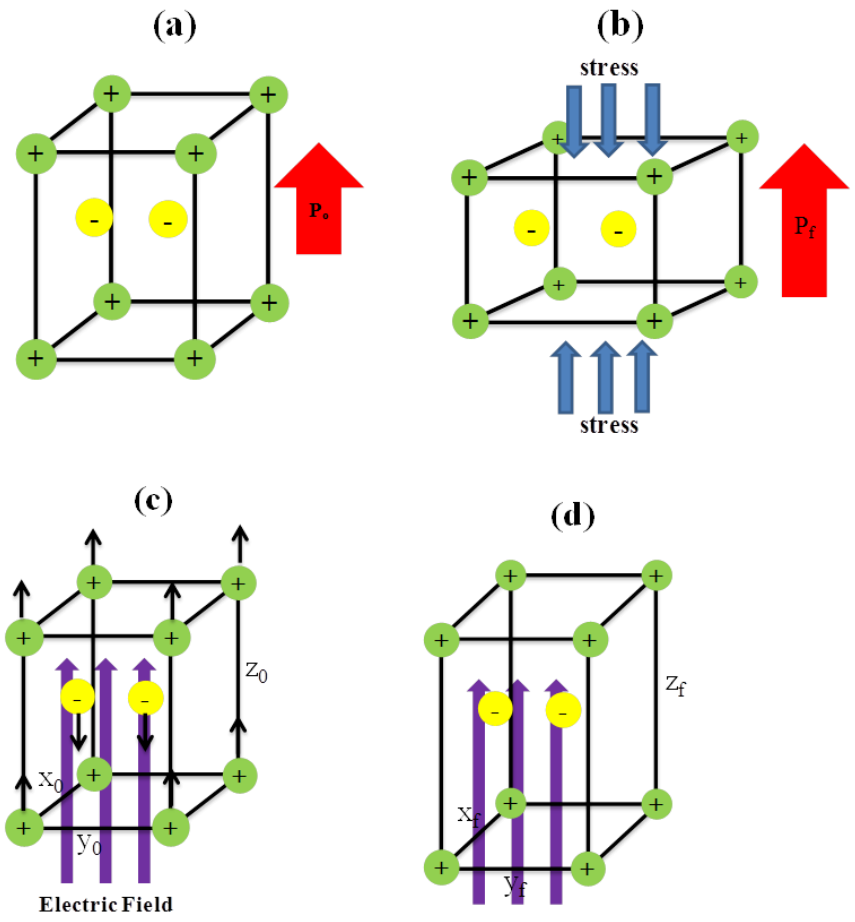

Figure 13. A piezoelectric effect scheme, (a) and (b), and the inverse piezoelectric effect, (c) and (d). (a) Intrinsic electric polarization of the material, (b) Applied stress causes the electric polarization strength to change; (c) An external electric field is applied to a piezoelectric, causing the ions to shift; (d) The shape of the crystal is altered due to the movement of ions.

2.1.3.1 $BiFeO_3$ (BFO)-Based Multiferroics

Multiferroic materials are being studied because of their promising applications in storage devices. Among them, BFO is receiving great attention because of its expected antiferromagnetic and ferroelectric behavior.

BFO Crystal structure

Bulk BFO exhibits a rhombohedrally distorted perovskite structure, Figure 14(a) with lattice parameter *a*=5.58Å and a rhombohedrical angle α=89.5º at room temperature, and belongs to space group R3c. BFO presents a ferroelectric polarization along [111] (pseudo-cubic) shown in Figure 14(b). In the hexagonal frame of reference, with the hexagonal c-axis parallel to the diagonals of the perovskite pseudo-cubic, the lattice parameters are *a*=5.58 Å, *c*=13.90 Å [37]. The oxygen ions has an octahedral arrangement with the octahedral oxygen rotated, this rotation angle is an important structural parameter. For an ideal cubic perovskite this angle would be 0º. To determine if the ions fit well into a perovskite structure this ratio can be used: $(r_{Bi} + r_O)/l$, where *r* is the ionic radius and *l* is the length of the octahedral edge. The Goldschmid tolerance factor [38] is analogous to the previous ratio and is defined as: $t = (r_{Bi} + r_O)/\sqrt{2}(r_{Fe} + r_O)$. When this ratio is smaller than one, the octahedral oxygen must buckle in order to fit into a cell that is too small. The Fe–O–Fe angle (154º-156º) [39,40] controls the super exchange interaction and the overlap between Fe and O, so it determines the magnetic ordering and conductivity.

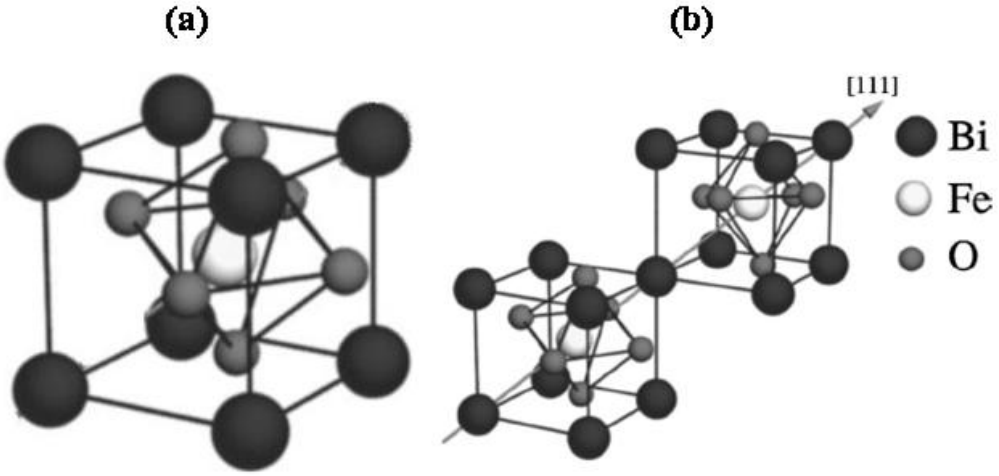

Figure 14. Schematic rhombohedrally distorted perovskite structure (a), and structure built up from two cubic perovskite unit cells. The cations are displaced along the [111] direction relative to the anions, and the octahedral oxygen rotate with alternating sense around the [111] axis (b), [41].

Magnetic Properties of BFO structures

The magnetic properties of BFO are governed by the Fe magnetic moments interactions. The Fe magnetic moments are coupled ferromagnetically within the pseudo-cubic (111) planes and antiferromagnetically (at Neel temperature ~ 643K) between adjacent planes, the so-called G-type antiferromagnetic order, that is, each Fe^{3+} spin is surrounded by six antiparallel spins on the nearest Fe^{3+} neighbors; this magnetic ordering has a short-rage. Furthermore there is a macroscopic magnetization (so called weak ferromagnetism), resulting of a canting of the antiferromagnetic sublattices due to symmetry when the magnetic moments are oriented perpendicular to the [111] direction. In addition, there is a spiral spin structure superimposed on the antiferromagnetic ordering, in this spiral spin structure the antiferromagnetic axis rotates through the crystal with an incommensurate long-wavelength period of 620 Å [42]. Through doping [43] the spiral spin structure is suppressed and this produces a cancellation of the macroscopic magnetization and consequently inhibits the observation of the linear ME effect [44].

Using numerical methods Spaldin *et al*. studied the weak ferromagnetism of BFO which is intimately connected with the symmetry of the system [45]. This weak ferromagnetism can only be produced if the sublattice magnetizations are oriented in the (111) plane in order to reduce the symmetry to the magnetic space group *Bb* or *Bb'*, which, apart from the primitive translations, contains only one glide plane. In this situation a canting of the magnetic sublattices does not reduce the symmetry and a weak ferromagnetism can occur. Moreover for the magnitude calculation of the weak ferromagnetism effect, Spaldin considered a homogeneous and collinear spin arrangement with the magnetic moments oriented in the (111) plane along either the *x*- or *y* axis in the coordinate system Figure 15(a), which allows the magnetic moments to relax freely

within the self-consistency cycle. The magnetic moments then cant away from the collinear direction (while remaining in the (111) plane) by an angle of about 1º Figure 15(b).

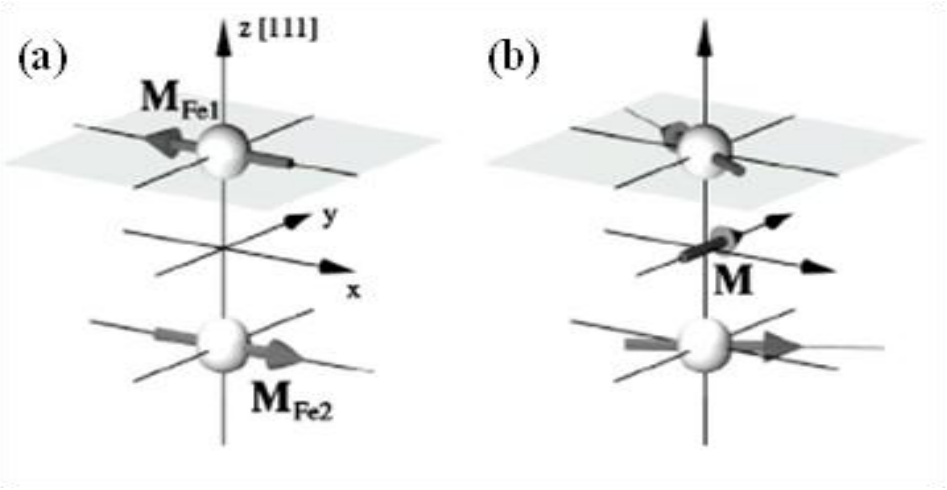

Figure 15. (a) Initial configuration of magnetic moments, $\boldsymbol{M}_{Fe1}$ and $\boldsymbol{M}_{Fe2}$, of the two iron atoms in the unit cell are oriented antiferromagnetically and collinearly in the (111) plane, allowing weak ferromagnetism by symmetry. (b) Magnetic structure including the spin-orbit interaction: The two iron magnetic moments rotate in the (111) plane so that there is a resulting spontaneous magnetization, $\boldsymbol{M}$ [41].

Also, Dzyaloshinskii and Moriya (DM) [45, 46] explained that the canting of the magnetic sublattice is produced by an antisymmetric spin coupling, known as the DM interaction, which results of the exchange interaction combined with spin orbit coupling. The DM interaction is expressed as

$$E_{DM} = -\frac{D}{2}.(M_{Fe1} \times M_{Fe2}) = -D(L \times M)$$

where $\boldsymbol{D}$ is a coupling vector analogous to the Heisenberg exchange constant J in the usual symmetric exchange interaction. The antiferromagnetic vector $\boldsymbol{L}=\boldsymbol{M}_{Fe1} - \boldsymbol{M}_{Fe2}$ is defined as the difference of the two sublattice magnetizations, and $\boldsymbol{M}=\boldsymbol{M}_{Fe1}+\boldsymbol{M}_{Fe2}$ is the resulting magnetization. From the form of E_{DM} it is clear that, for constant $\boldsymbol{D}$ and fixed orientation of $\boldsymbol{L}$,

the canting of the magnetic sublattices always occurs such that ***D*** (required by symmetry to be oriented along the [111] axis), ***L***, and ***M*** build up a right-handed system.

Ferroelectric Properties of BFO

Perosvkites form an important group considered as ferroelectrics. In these materials occurs a ferroelectric transition due to a balance between long-range Coulomb interactions and short-range repulsions. Bulk BFO is a well known ferroelectric [47] with a Curie temperature of 1100 K. The polarization in BFO bulk is produced along the diagonal [111] of a perovskite pseudo-cubic cell or along the diagonal [001] of a hexagonal cell, the first reports of polarization measurements were around 6 μC/cm^2. The spontaneous polarization along [111] is due to the *R*3*c* symmetry, and Bi, Fe, and O are displaced relatively to one another along this threefold axis. Bi and O have the largest relative displacement, consistent with a stereochemically active Bi lone pair [48]. High leakage current and small remanent polarization, are features of BFO. The high leakage current is produced due to a deviation from oxygen stoichiometry (oxygen vacancy), which originates a change in oxidation state of Fe ions (from Fe^{3+} to Fe^{2+}) in order to compensate for the charge of oxygen vacancies [49-50].

BFO, despite of its current leakage and small polarization in bulk, has been much appreciated at the nanoscale thanks to its magnetoelectric behavior [51], which makes it a potential candidate for new applications such as data storage and electronic devices. Besides, its limitations can be reversed performing synthesis processes under controlled atmosphere or suitable selection of doping species, which can avoid the large formation of oxygen vacancies as well as the formation of a single phase, leading to an improved ferroelectric property.

CHAPTER III: LITERATURE REVIEW

3.1 Literature review

3.1.1 ZnO-Based Diluted Magnetic Semiconductors

ZnO based DMS has been widely studied due to its peculiar properties, such as optical, electrical, magneto-optical and magnetic properties. ZnO based DMS has potential applications in technology, science and spintronics. Researches in different areas are trying to control structural, optical, electrical, and magnetic properties of these materials. Through the control of the synthesis process a multifunctional material could be obtained.

There is a lot of controversy among experimental researchers about the magnetic properties that exhibit these materials, due to some claims that the novel property is generated by nanoclusters present in the material. Other researchers claim that the novel property is produced by an effective incorporation of the dopants in the host principal.

A review of theoretical and experimental studies is presented here which suggests that doping of ZnO with transition metals (TM) or rare earth ions could induce room-temperature ferromagnetic and magneto-optical properties. Theoretical works have reported that II-VI DMS with Curie temperature above room temperature would exhibit a ferromagnetic behavior [12,52]. In the study of transition metals in ZnO based DMS realized by K. Sato [53] it is shown that the ferromagnetic state is most stable than the spin-glass state. Studies on the electronic structure of ZnO based DMS shows two self-consistent solutions due to the fact that there are two directions of the magnetic moment along the quantization axis, i.e., up and down directions. A solution corresponds to a ferromagnetic state in which all of the magnetic moments are parallel with each other, could be written as $(Zn,TM_x(\uparrow))O$, where x is the concentration of TM and (↑) is spin up

and other solution correspond spin-glass state in which the magnetic moments are pointed randomly at each other. Therefore, the system has no magnetization and can be written as $(Zn,TM_{x/2}(\uparrow),TM_{x/2}(\downarrow))O$ where (↓) is a spin down. Comparing the total energy of the ferromagnetic state with that of the spin-glass state, it is possible to judge which state is more stable. Naively, the total energy difference between these two states corresponds to T_C. Also Sato calculated energy differences to TM, the concentrations were 5%, 10%, 15%, 20% and 25%. The results of these studies suggest that the ZnO doped with V, Cr, Fe, Co, or Ni is a candidate for high-T_C ferromagnetic DMS.

K. Sato, *et al.*[54] have suggested that the ZnO doped with V, Cr, Fe, Co or Ni is a candidate for high-T_C ferromagnetic DMS. Therefore Sato *et al.* have claimed that magnetic behavior of DMS follows from the exchange interactions between spins of the band carriers and localized spins of magnetic ions (*sp-d* exchange) or between localized spins (*d-d* exchange). Many microscopic models have been used to explain the nature of these interactions-dominated mechanisms in II-VI DMS [55, 56].

In experimental works many researchers have reported the magnetic behavior of ZnO based DMS for more than a decade; e.g., L. El Mir, *et al.* [57] have reported the effects of vanadium concentration on electrical optical and magnetic properties of vanadium doped zinc oxide (VZO) thin films, where thin films were deposited by rf-magnetron sputtering. The rf generator operated at 13.56 MHz. The sputtering chamber was evacuated to a base pressure of 6×10^{-5} Pa before introducing the sputtering argon gas with 99.9999% purity without oxygen. The XRD patterns of thin films deposited onto glass substrates showed that the films were polycrystalline with a hexagonal structure and a preferred orientation with *c*-axis perpendicular to the substrates. All films showed a high transparency within the visible range with an average

transmittance of about 90%. Besides, the absorption edge of VZO films deposited with different vanadium concentrations shifts to a shorter wavelength. The blue shift of absorption edge was explained due to the increase of carrier concentrations. The magnetic properties were analyzed at 4 K and 300 K, the samples exhibited ferromagnetic and paramagnetic components. Due to the random orientation of the particles, no remnant magnetization was observed. After the subtraction of the diamagnetic and paramagnetic components it was observed that the ferromagnetic component deceases at T=300 K but is still present, which showed that the critical temperature of this phase is above 300 K. The ferromagnetic component had a saturation magnetization of 15 emu/cm^3. If the ferromagnetic behavior is assumed to be originates by a secondary phase, not detected by the X-ray diffraction, the volume of this phase can be roughly estimate as <1% of the total volume film. This would indicate a saturation magnetization of >1500 emu/cm^3 which is close to that of standard FM metals (Fe).

S. Karamat *et al.* [58] have reported magnetism in V doped ZnO in bulk form, prepared by solid state reaction techniques. Precursors ZnO and V_2O_5 powders were mixed and grinded properly. The mixture was then annealed at 700ºC for 8 h in air. The annealed powder thus obtained was pressed to form dense pellets and sintered for 14 h at low temperature at 900ºC in air. Magnetic properties were measured using a vibrating sample magnetometer for all the samples. The measurement indicated the overlapping of diamagnetic signal on ferromagnetic signal of samples. The cause of diamagnetic behavior in the samples was not clarified. Also, the consistency of central position of hysteresis with zero-field predicted the absence of anti-ferromagnetism. The M–H curves showed weak magnetic behavior for all samples. The observation of ferromagnetic behavior indicates that the V^{2+} ions have been substituted the Zn sites without changing the wurtzite structure of ZnO.

Jinghai Yang *et al.* [59] have studied the structure and magnetism of $Zn_{0.9}Co_{0.1}O$ DMS films, the films were deposited onto Si(100) substrates prepared by chemical solution deposition method. X-ray diffraction patterns for ZCO films confirmed the wurtzite structure. All the films were textured with a c-axis preferred orientation as was evidenced from strong (0 0 2) peak in XRD patterns, which also showed that the position of (0 0 2) peaks shifts to higher angles. The authors explained that this shift happens because the cobalt radius (0.074 nm) is a little smaller than Zn^{2+} (0.076 nm). The shift also revealed that there was no octahedral cobalt in the sample because the radius of octahedral cobalt is bigger that zinc, so the peaks of ZCO should shift to lower angles, which was opposite to their result. As a result, Co^{2+} substitutes for Zn^{2+} without changing the wurtzite structure. Magnetic properties showed ferromagnetic behavior at room temperature. They gave two possible explanations for the origin of ferromagnetism in Co-doped ZnO system. One possibility of the origin of ferromagnetism was the Co metal clusters, the other was the Co substitution on Zn sites. There were no Co clusters in the sample, so ferromagnetism in ZCO film was an intrinsic behavior of Co^{2+} substitution for Zn^{2+} in ZnO lattice. The ferromagnetic behavior could be explained on the formation of bound magnetic polarons.

Hiromasa Saeki *et al.* [60] have carried out experiments with vanadium doped ZnO at different concentrations (x= 0.05 to 0.15). The films were grown on α- Al_2O_3 (1120) substrates using a pulsed laser deposition at 300ºC in an oxygen ambient with a pressure of 10^{-5} - 10^{-4} Torr and laser energy density of 1 J/cm^2 . Ferromagnetic behavior at 300 K was observed for $Zn_{0.85}V_{0.15}O$ films measured; the films exhibited 200 Oe of coercivity and a saturation magnetization at 0.5 μ_B/V. This magnetic behavior was attributed to a double exchange mechanism [61].

N. Hoa Hong *et al.* [62] have reported magnetism in $Zn_{0.95}V_{0.05}O$ thin films at room temperature. The films were grown by the pulsed laser deposition (PLD) technique using a KrF

laser (λ = 248 nm) on R-cut sapphire (1102) substrates. The repetition rate was 3 Hz and the energy density was 2 J/cm^2. The substrate temperature was 600, 650 or 700ºC. During deposition, the oxygen partial pressure (Po_2) was kept as 10^{-1} Torr. Their results showed a temperature dependence of the magnetization that might indicate a spin-glass-like behavior.

Congkang Xu *et al*. [63] have reported ferromagnetic behavior in V-ZnO nanorods in the 10- 293 K range, which was attributed to exchange interaction between carriers and localized magnetic ions. Nonetheless, other factors such as the structural defects and growth conditions were shown to have a strong influence on the magnetic behavior.

M. Venkatesan *et al.* [64], have reported ferromagnetic behavior in Sc, Ti, V, Fe, and Co doped ZnO thin films. This ferromagnetic behavior was explained in terms of the spin-split donor impurity-band model. All samples were prepared by conventional pulsed laser deposition using a KrF excimer laser operating at 248 nm and a fluence of 1.8 J/cm^2. The oxygen pressure during deposition was varied from 1 to10^{-4} mbar. Film thickness was in the range 60–120 nm.

O. Toulemonde *et al*. [65] have reported the synthesis of Co^{2+} doped ZnO powder, with a cobalt concentration ranging from x = 0.005 to x = 0.1. The samples were prepared by a Pechini process and all calcined at 1000ºC for 10 h in air. The magnetic properties of the compounds were measured in a superconducting quantum interference device magnetometer from 2 to 10K at applied fields up to ±5T. Their results showed no hysteresis and no remanence indicating no long-range ferromagnetic ordering. The asymptotic magnetization reached at H = 5T drastically, then decreased with the cobalt concentration, supporting the view that antiferromagnetic interactions occur and they should be linked to the cobalt concentration matrix.

Moreover there are reports which claim that ferromagnetic behavior is not due to secondary phases which should exist at the doping limit. Ueda *et al.* [66] obtained a Curie temperature higher than room temperature for the Co-doped ZnO films grown by the pulsed-laser deposition technique, but its reproducibility was less than 10%.

Besides there are changes in other properties of doped ZnO; e.g., R. Slama *et al.*[67] have reported a study on optical properties for Vanadium-doped zinc oxide nanoparticles that have been synthesized by sol-gel method, the obtained powder was heated in a furnace under air conditions at 500ºC for 2h. All samples exhibited a red-shift of absorption edge and a significant enhancement of light absorption in the visible light region, therefore above 5% of doping secondary phases of vanadium oxides were observed.

S. Thota *et al.* [68], have reported the growth of Ni doped ZnO thin films on [0001] oriented Al_2O_3 substrates. The samples exhibited hexagonal wurtzite crystal structure with preferential growth of (0001) plane. A decrease in the *c* parameter with increase in nickel content *x* was also observed. The observed characteristic optical absorption bands in the UV–visible regions were attributed to *d–d* transitions from $3T_1$ (F) to $3A_2$ (F), $3T_1$ (P), and $3T_2$ (F) of the Ni^{2+} ions (occupying zinc sites in oxygen tetrahedral sites). This interpretation was supported by the observed gradual red-shift of optical band gap absorption edge with increase in *x*; typical values being ~3.27 and 3.05eV for x=0.01 and 0.163, respectively. The films exhibited hysteresis loops at room temperature with values of coercivity and remanence in the range 7.8–12 kA/m and 3.22–8.45 kA/m, respectively in the 2–16.3 at% Ni range. The electrical conductivity of the nickel doped samples was found to increase progressively with increase in nickel content and was explained on the basis of impurity *d*-band splitting.

Based on the above discussed information, the present work was focused on the systematic study of the structural, optical and magnetic properties of ZnO based DMS as a function of the dopant type (Co, Sc, V species) and concentration (x= 0.0 at% - 10 at%). The synthesis technique was designed to obtain a material without impurities and exhibiting room-temperature magnetic properties due to the effective incorporation of the dopant species in the ZnO host lattice in powders and thin films produced by a modified sol-gel technique.

3.3.2 $BiFeO_3$ (BFO)-Based Multiferroics

Multiferroics are materials that have coupled electric, magnetic, and structural order parameters that result in simultaneous ferroelectricity, ferromagnetism, and ferroelasticity. BFO is a compound with a perovskite structure that belongs to space group R3c, with a rhombohedral unit cell at room temperature [69, 70]. BFO is a well known multiferroic compound having simultaneous ferroelectric and weak ferromagnetic properties at room temperature. This material is a ferroelectric (T_C=1183 K) and antiferromagnetic (T_N=643 K), exhibiting weak magnetism at room temperature due to a residual moment from a canted spin structure [69]. BFO has two order parameters: the spontaneous polarization is oriented in the direction [111] of the pseudo-cubic perovskite unit cell and G-type antiferromagnetic ordering appears when the magnetic moments of iron ions, preserving a locally antiparallel orientation, are turned in a spiral oriented along the direction [$\mathbf{10\bar{1}}$]. Recently, the detection of a giant magneto electric (ME) effect (an electric field can induce change in magnetization [69]) and of a giant magneto capacitance (the appearance of electric polarization under the action of a magnetic field [71]) have been confirmed in BFO films. The practical application of multiferroic BFO still faces different challenges, e.g. weak

magnetic characteristics, lower magnetoelectric coupling coefficients, wide differences in ferroic transition temperatures and a high leakage current [72-74]. J. Wang *et al.* [69] were the first to report the highest remanent polarization (P_r, 50 to 60 $\mu C/cm^2$) in BFO thin films grown by PLD onto single crystal $SrTiO_3$ (100) substrates. This value is an order of magnitude higher than the highest reported value of 6.1 $\mu C/cm^2$ for bulk BFO. The corresponding magnetic properties showed an appreciable saturation magnetization of ~150 emu/cm^3 and a coercive field of ~200 Oe.

K. Young *et al.* [75] have reported $BiFeO_3$ thin films that showed enhanced electrical properties with low leakage current density value of ~ 10^{-4} A/cm^2 at a maximum applied voltage of 31V. This enhanced electrical resistivity allowed the authors to obtain giant ferroelectric polarization values such as saturation polarizations of 110 and 166 $\mu C/cm^2$ at room temperature and 80K, respectively. The thin films were grown on $Pt/TiO_2/SiO_2/Si$ substrates by pulsed-laser deposition.

However, a spontaneous magnetization in BFO has been observed due to transition metal, lanthanides, alkali earth metal doping of BFO host. This enhancement in magnetization has been attributed to valence fluctuations between Fe^{2+} and Fe^{3+} ions or to spin canting [76]. The incorporation of more than one rare earth ion into the BFO host (co-doping) has been proposed as an effective way to overcome the above mentioned limitations in bare BFO. Uniyal *et al*.[76] have observed electrical polarization hysteresis loops and spontaneous magnetic moment at room temperature in $Bi_{0.9-x}La_{0.1}Pr_xFeO_3$ (x= 0-0.2). The samples were in powdered forms and synthesized via a solid-state route at 820ºC. The presence of Pr ions enhanced the dielectric properties and caused a systematic increase in both the ferroelectric and ferromagnetic

properties. The direct dependence of the polarization on the magnetic field evidenced the magneto-electric coupling in these materials.

Moreover some works have reported an improvement of other BFO electrical properties, e.g., S. Lee *et al*. [77] have reported the synthesis of $BiFe_{1-x}Mn_xO_3$ (x= 0.1; 0.2; 0.308; 0.438; 0.5) films deposited by combinatorial pulsed laser deposition technique using two stoichiometric targets of $BiMnO_3$ and $BiFeO_3$. The deposition temperature and oxygen pressure were 823 K and 3 $x10^{-3}$ Torr, respectively. The local piezoelectric coefficient for a $BiFe_{0.9}Mn_{0.1}O_3$ thin film (d_{zz}~ 9.7 *p*m/V) was appreciably larger than that of $BiFe_{0.8}Mn_{0.2}O_3$ (d_{zz}~2.7 *p*m/V). It was also confirmed that the piezoelectric coefficient decreased with larger x the decreasing rate was drastically reduced above $x \sim 0.4$.

P. Singh *et al*. [78] have reported magnetic and electric properties of epitaxial Sr-doped $BiFeO_3$ thin film grown on $SrRuO_3/SrTiO_3$ (001) substrates by pulsed laser deposition at different oxygen pressures. Films deposited at high oxygen pressure exhibited ferroelectric behavior but without any signature of clear ferromagnetism at room temperature. The $Bi_{0.75}Sr_{0.25}FeO_3$ thin films grown at low oxygen pressure showed ferroelectric loops with a remnant polarization of $2P_r$ =86.13μC/cm^2 and coercive field of $2E_C$= 75.5 kV/cm.

X. Wang *et al.* [79] have produced $Bi_{1-x}Ce_xFeO_3$ (BCFO) films with x = 0, 0.05, 0.10 and 0.15 by a sol–gel deposition method followed by annealing at 500ºC in air. The films deposited on $LaNiO_3/Si(100)$ substrates with $x < 0.15$ consisted of a single phase with dense and smooth surface. A noticeable improvement of hysteresis loops with better squareness than that of BFO film was obtained for the 5 molar percent Ce-substituted BCFO film. The remnant polarization and the coercive field were 71 μC/cm^2 and 103 kV/cm, respectively, under a maximum applied

field of 245 kV/cm. The leakage-current density of the 5 molar percent Ce-substituted BFO thin film was significantly decreased; the leakage-current density was 2.2×10^{-7} A/cm^2 at 300 kV/cm. Moreover, the dielectric constant for the film with x = 0.05 were substantially enhanced. These results demonstrated that Ce substitution could be a simple and effective method to obtain BFO films exhibiting a large ferroelectricity.

Besides its annealing under controlled atmosphere, the properties of BFO can be improved by controlling defects in the structure; bismuth ferrite usually presents oxygen vacancies. S. K. Singh *et al.* [80] have reported a study of an enhanced polarization and reduced leakage current in $BiFeO_3$ thin films, BFO films were formed by depositing sol-gel chemical solution on Pt/Ti/SiO2/Si(100) and Pt/sapphire(0001) structures. The films were annealed at 550ºC for 5 min in nitrogen atmosphere. The polarization versus electric field on BFO films were measured at RT and 80 K. The hysteresis loops with the remnant polarization *Pr* larger than 100 μC/cm^2 were observed at RT, although the exact *Pr* value was difficult to determine because of the existence of the leakage current component. The coercive field was approximately 0.4 MV/cm, which means that BFO films require a high applied electric field to get polarization. On the other hand, the leakage current at RT increases when the electric field higher than 0.25 MV/cm is applied. These two factors were origins of the non-saturated *P-E* hysteresis loop at RT. S. K. Singh obtained a saturated rectangular-shaped hysteresis loops at 80 K, which was much better than those at RT.

Based on the available information, this part of the research addressed the systematic study of the structural, optical and magnetic properties of BFO as a function of the type of dopant species (Pr or Co ions) and their concentration. The main challenge was the development of suitable sol-gel based synthesis protocols to obtain a single phase without the parasitic phases

that usually presents this material. Cobalt ions could influence the magnetic properties of the doped BFO, whereas the actual incorporation of Pr species in the BFO lattice could be conducive to the enhancement of the corresponding ferroelectric properties.

CHAPTER IV: EXPERIMENTAL

A modified sol-gel approach to synthesize well-crystallized pure and doped ZnO and BFO nanocrystalline powders and thin films was developed. The attachment of ZnO and BFO onto different types of substrate was optimized by selecting suitable organic agents to control the viscosity of precursor solutions and improve the attachment of the material to the substrate surface.

4.1 ZnO-Based Powders and Films

4.1.1 Materials

Pure and Co-, Sc- and V- doped ZnO powders and films were synthesized by the sol-gel technique. Zinc acetate [$Zn(CH_3COO).2H_2O$, purity 98%], cobalt acetate [$Co(CH_3COO)_2.4H_2O$ purity 99%], scandium nitrate [$Sc(NO_3)_3.\ 5H_2O$, purity 99.9%] and vanadium chloride [VCl_3, purity 97%] were used as-received. Suitable amounts of these reagents were used according to the dopant atomic fractions, which ranges between 1 at% and 10 at%. Ethanol was used as solvent and monoethanolamine was used as viscosity-controlling additive. The concentration of total metals (Zn+dopant) was kept constant at 0.2 mol /L in all tests. The substrates used were Quartz and Silicon (100), provided by Quartz Plus Inc. and Addison Engineering Inc. respectively. The Quartz substrates were cleaned by ultrasonication in acetone then washed with ethanol and deionized water before spin- coating. The Silicon substrates were cleaned with kimwipes and high pressure air before spin- coating.

4.1.2 Synthesis of Powders and Thin Films

Powdered samples were synthesized by dissolving suitable amounts of Zn and dopant salts in ethanol and subsequent heating at 120ºC for twelve hours to assure the complete removal

of the solvent. The obtained solid precursor was then annealed in air for 1 hour in the temperature range between 400ºC and 500ºC. Annealed powders were submitted for characterization. The synthesis of thin films started by dissolving the above mentioned precursor salts in ethanol. Next, monoethanolamine at a ratio of MEA/Zn=1:1 was added to 10mL of the metal precursor solution to control its viscosity. The resulting solution was then heated up to 150ºC for 1hour to obtain a clear solution to be added drop-wise onto a clean quartz substrate and spin-coat at 3000 rpm for 20 s. After each coating cycle, produced films were pre-dried for 5 minutes at two different temperatures (80ºC and 200ºC) to remove organic residues. These spin-coating/drying cycles were repeated for twenty times to thicken the films. The spin-coated films were then annealed in air for one hour at temperatures of 500ºC and 550ºC. The heating rate was 10ºC / min for each sample.

In Figure 16 the stages that were followed to obtain pure and doped ZnO powders and thin films are shown.

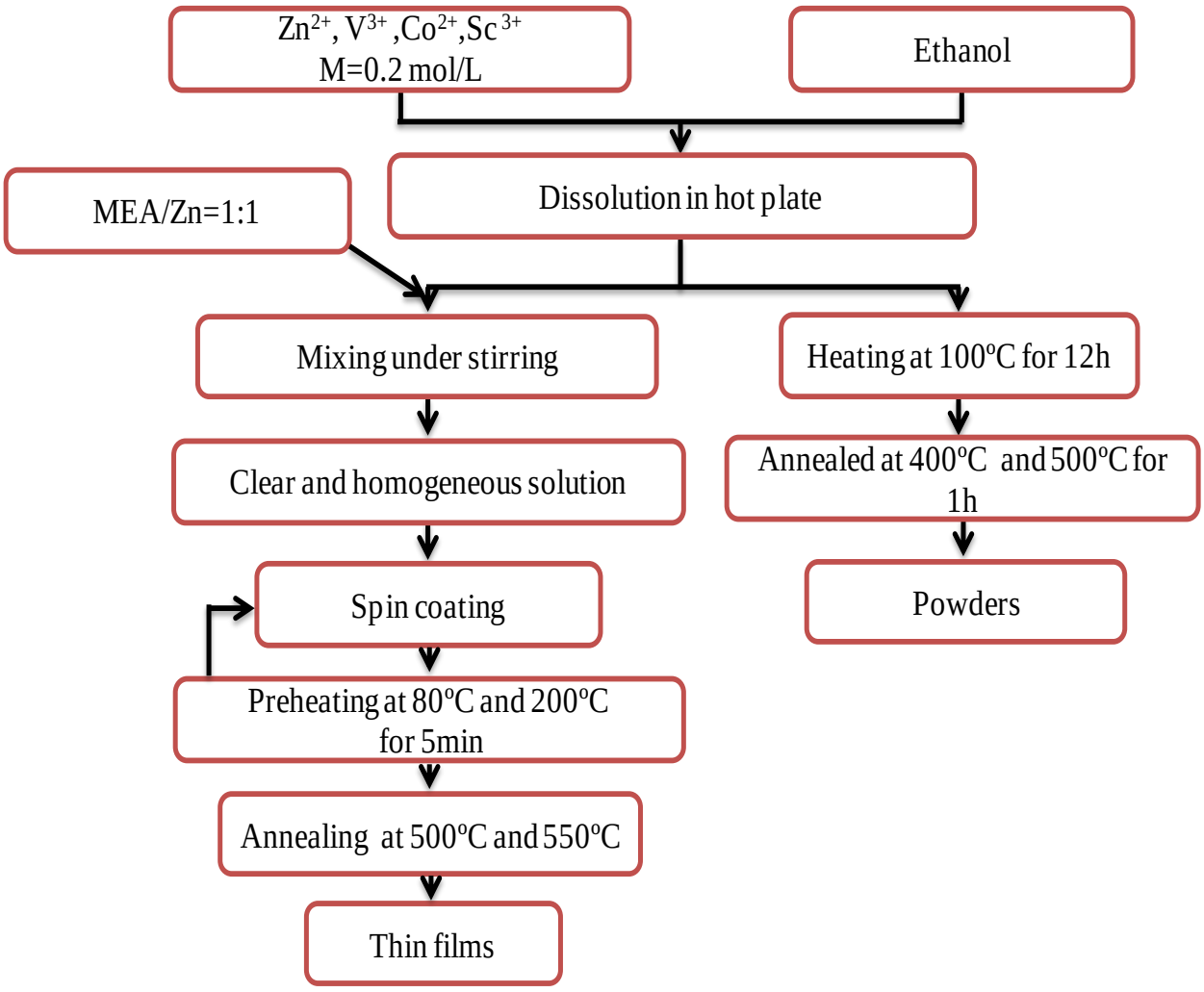

Figure 16. Flow chart of the synthesis process of pure and doped ZnO powders and thin films.

4.2 Synthesis of BFO Thin Films

4.2.1 Materials and Procedures

Pure and doped bismuth ferrite thin films were synthesized in acetic acid medium. Bismuth nitrate [$Bi(NO_3)_3.5H_2O$, purity 99.9%], Iron nitrate [$Fe(NO_3)_3.9H_2O$, purity 99.9 %],

cobalt acetate [$Co(CH_3COO)_2.4H_2O$ purity 99%] and Praseodymium nitrate [$Pr(NO_3)_3.6H_2O$, purity 99.99 %] were used as precursor salts. Acetic acid was used as solvent and glycol was used as a viscosity-controlling additive. The concentration of total metals (Bi, Fe + dopant) was kept constant at 0.08 mol /L in all tests. The substrates used were platinum ($Pt/TiO_2/SiO_2/Si$), provided by Radiant Technologies Inc. The platinum substrates were cleaned with kimwipes and high pressure air before spin- coating.

4.2.2 Synthesis of Thin Films

Film samples were synthesized by dissolving suitable weights of the precursor salts according to the stoichiometry $Bi_{1-x}M_xFeO$ (M= Pr) and $BiFe_{1-x}N_xO$ (N= Co) to achieve the desired atomic percentages, *x* in the range 0-4 at%. The synthesis of thin films started by dissolving the above mentioned precursor salts in acetic acid. Next, 1mL of glycol was added to 4mL of the metal precursor solution to control its viscosity. The resulting solution was then stirred at room temperature for 1hour to obtain a clear solution that was added drop-wise onto clean platinum substrates and spin-coated at 3000 rpm for 15 seconds. After each coating cycle, produced films were pre-dried for 3 minutes at two different temperatures (100ºC and 220ºC) to remove organic residues. These spin-coating/drying cycles were repeated for twenty times to thicken the films. Spin-coated films were then thermally treated in air for two hours for pure and praseodymium doped films and three hours for cobalt doped films at 500ºC. The heating rate was 10ºC / min in all experiments.

In Figure 17 the stages that were followed to obtain pure and doped BFO thin films are shown.

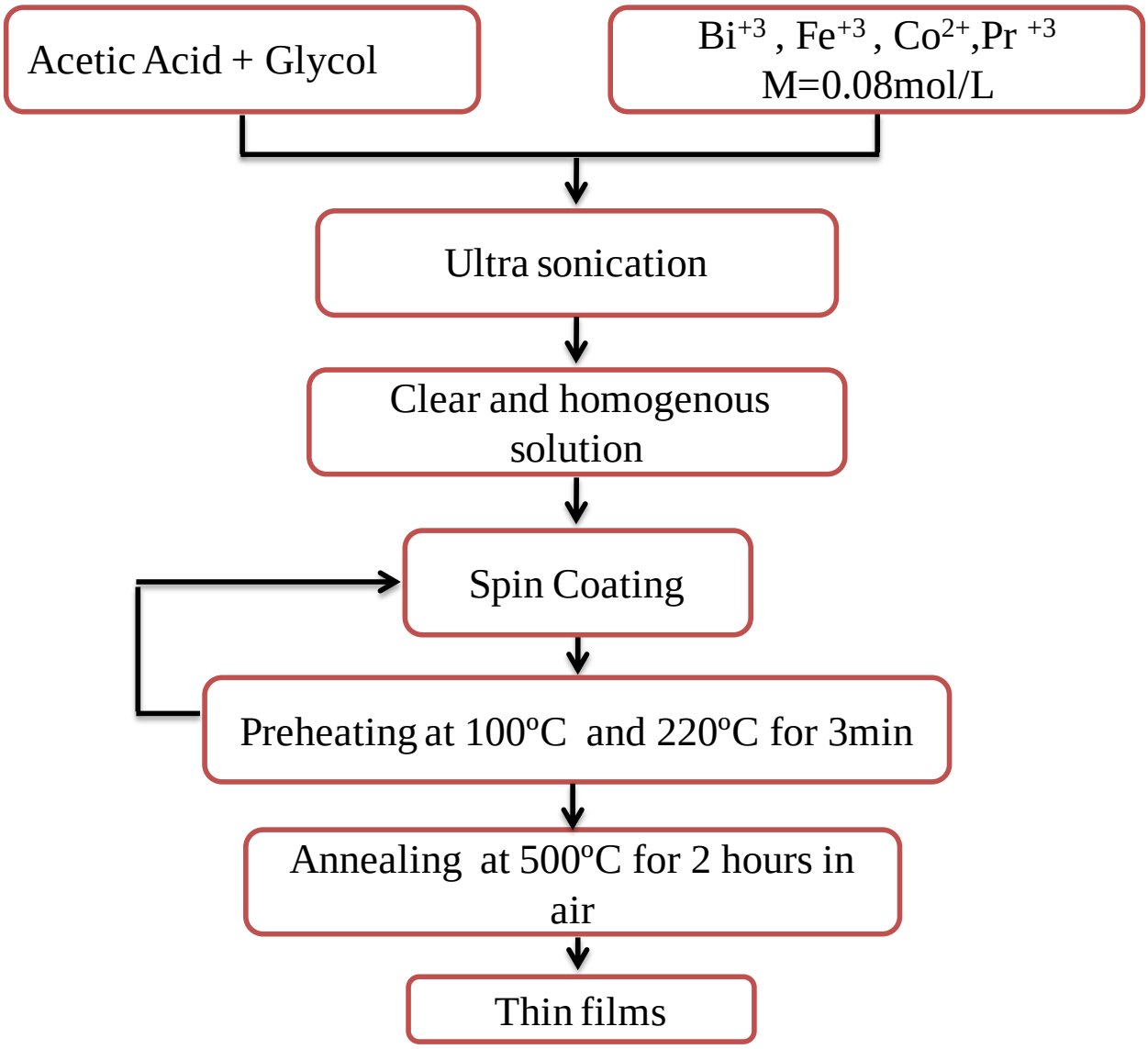

Figure 17. Flow chart of the synthesis process of pure and doped BFO thin films

4.3 Materials Characterization

The structure of produced powders and films was determined by X-ray diffraction using a SIEMENS D500 unit with a Cu-Kα radiation. Thermo-gravimetric analyses (TGA) were carried out in air inside a TGA/SDTA851 Mettler-Toledo unit to determine the crystallization temperature of the oxides. Optical properties of powders and films were measured using a UV-

vis DU 800 spectrophotometer and a Fluoromax2 Photo-spectrometer, respectively. The excitation wavelength for photoluminescence measurements was 342 nm. Magnetic properties were measured in a superconducting quantum interference device (SQUID) and in a vibrating sample magnetometer (VSM) Lake Shore 7410 and electrical properties were measured using a RT 6000 HVS ferroelectric tester (Radiant Technologies, Inc.).

4.3.1 X-Ray Diffraction

For the analysis of the structural properties of the samples a X-ray diffractometer with CuK_α (λ=1.5406Å) radiation was utilized. For ZnO-based DMS powders and thin films all measurements were carried out at 40 kV and 40 mA in the range of $25^o \leq 2\theta \leq 75^o$. The scanning step and sampling time were 0.020^o and 1 second per step, respectively.

To determine the average crystallite size *t* the Debye-Scherrer's equation (1) was used [81] for the principal peaks which correspond to the crystallographic planes (100), (002) and (101) of the ZnO host.

The peaks instrumental broadening was neglected based on the good agreement between microspcopy size and Scherre's average crystallite size in nanocrystalline ZnO [82].

$$t = \frac{0.95\lambda}{B\cos\theta} \qquad (1)$$

where λ represents the wavelength of the X-ray radiation, B is the full width at half maximum (FWHM) of the diffraction peak (in radians) and θ is the Bragg angle. To determine the lattice parameters *a* and *c*, the peak corresponding planes (100) and (002) and the relation for the lattice spacing equation (2) [81] between planes of a hexagonal closed packed lattice were used.

$$\frac{1}{d_{hkl}^2} = \frac{4}{3}\left(\frac{h^2 + hk + k^2}{a^2}\right) + \frac{l^2}{c^2} \qquad (2)$$

where *a* and *c* are the lattice parameters, *h*, *k*, and *l* are Miller indices and *d* is the lattice spacing between the planes (*hkl*). The spacing is related to the diffraction angle through Bragg's law equation (3):

$$2dsen\theta = n\lambda \qquad (3)$$

where λ is the X-ray wavelength, θ is the diffraction angle, and *n* is the diffraction order (*n*=1). The ZnO hexagonal unit cell has two lattice parameters (*a*= 3.249Å and *c*=5.207 Å) [25].

To analyze the structural properties of BFO samples the same instrument was utilized. All measurements were carried out at 40 kV and 40 mA in the range of $20^o \leq 2\theta \leq 60^o$. The scanning step and sampling time were 0.020º and 1 second per step, respectively. Again, to determine the average crystallite size *t* the Debye-Scherrer's equation was used and utilized the non-overlap peak of the BFO host which corresponds to the crystallographic plane (102). To determine the lattice parameter *a* the following equation (4) [83] was used:

$$\frac{1}{d_{hkl}^2} = \frac{(h^2 + k^2 + l^2)sen^2\alpha + 2(hk + kl + hl)(\cos^2\alpha - \cos\alpha)}{a^2(1 - 3\cos^2\alpha + 2\cos^3\alpha)} \qquad (4)$$

where *a* is the lattice parameter, *h*, *k*, and *l* are the Miller indices and d_{hkl} is the lattice spacing for the planes (*hkl*), α=89.5º. The lattice spacing can be calculated using Bragg's law. The BFO Rhombohedral unit cell has a lattice parameter (*a*= 5.58Å).

4.3.2 Absorption Spectroscopy

ZnO is a direct band gap semiconductor. This means that the maximum in the valence band and the minimum in the conduction band occur at the same value in momentum space (k=0). Valence electrons can move into the conduction band by absorption of a photon leaving a hole in the valence band and then creating electron-hole pairs, as is schematically shown in Figure 18. If the electron-hole pair is bound through electrostatic interactions it is called exciton.

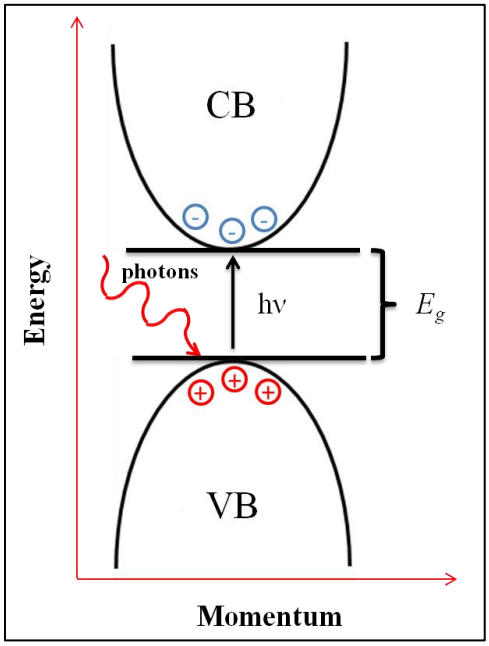

Figure 18. Direct band gap semiconductor

To determine the experimental value of the band gap of ZnO-based DMS in thin films an indirect calculation was made, starting from the absorbance measured at the range from infrared to ultraviolet in a UV-vis DU 800 spectrophotometer.

It is known that when a light beam travels through a medium, part of the beam is reflected, part is transmitted, and the rest is absorbed by the material. The absorption ability of a material is

measured through its absorption coefficient **α,** defined in terms of the intensity change of a light beam per unit distance that the beam traveled through the medium as represented in equation (5)

$$\frac{dI(\lambda)}{dx} = -\alpha(\lambda)I(\lambda) \qquad (5)$$

Solving this first order differential equation the following expression can be obtained equation (6):

$$\ln(\frac{I_0}{I}) = \alpha x \qquad (6)$$

where x is the distance that a light beam travels in the medium, which in our case is the film. From equation (6) the first term is the absorbance:

$$A = \ln(\frac{I_0}{I}) = \alpha x \qquad (7)$$

Hence:

$$\alpha = \frac{A}{x} \qquad (8)$$

Then the absorption coefficient due to interband transition near the band-gap, is well described by Tauc's Equation [84]:

$$\alpha h\nu = B(h\nu - E_g)^n \qquad (9)$$

where B is a constant, $h\nu$ is the photon energy, and E_g is the optical gap. In the second term in equation (9) the exponent is n= ½ because ZnO presents a direct transition. Combining equations (8) and (9):

$$(\alpha h\nu)^2 = (\frac{A}{x} h\nu)^2$$

and

$$(\alpha h\nu)^2 = B^2(h\nu - E_g)$$

Then from the experimental data we can get the band gap value relating these equations.

4.3.3 Photoluminescence Spectroscopy

To analyze the optical properties of ZnO-based DMS powders and thin films, a Shimadzu RF 5301 PC Spectro fluoro-photometer instrument was used. The photoluminescence measurements of bare and doped ZnO samples were at room temperature and excitation wavelength was 342nm. The spectrum of all samples showed a luminescence peak around 390 nm, corresponding to the UV emission characteristic of ZnO.

The optical properties of a semiconductor have their origins in the intrinsic and extrinsic defects. Intrinsic defects are proper of the principal host while the extrinsic defects are related to dopants and impurities. These defects influence emission processes.

Luminescence is any light emission through processes different from blackbody radiation and is non-equilibrium process that requires external excitation. Photoluminescence (PL) is a mean of light emission. For semiconductors, it is a result of photo-excitation through incident-photon absorption that promotes an electron from the valence band toward the conduction band. This leaves a hole in the valence band and through momentum-conserving processes, since the photon momentum is negligible, the electron–hole pairs are generated. In this mechanism of photo-excitation, the electron usually has excess energy and relaxes non-radiatively in typically 15-25 *p*s[85], to the band edge through inter-or-intra-sub band scattering and then recombines with the hole radiatively by emitting a photon, as represented schematically in Figure 19 [86], or non-radiatively by lattice vibrations, towards trapping states generated by impurities, dopants or defects. These trapping states lie in between the conduction and valence band, [87] as presented in Figure 20.

ZnO has an emission in the UV region. This emission is considered as principal for ZnO and it is produced in the near band edge (NBE). This means a radiative emission due to electron–hole

recombination. Usually this band is affected by dopants which produce a quenching effect. This quenching effect occurs when the electron jumps into trapping states and then moves to the valence band through non-radiative transitions.

Depending on the synthesis process, this material can present other emissions in the visible region produced by deep-level transitions, usually attributed to defects present in the structure. Some research attributes this emission to defects such us oxygen vacancies or zinc interstitials but these defects cannot be measured to corroborate these attributions. Hence, these effects are not well-understood and still controversial. Recently, theoretical researchers have developed calculations to study structural defects and inferred that the main factor for these emissions can be attributed to zinc vacancies because their formation requires lower energies than the other defects such us zinc interstitials, zinc anti-sites or oxygen vacancies [88]. PL is commonly employed in extracting important physical properties and performing materials characterization.

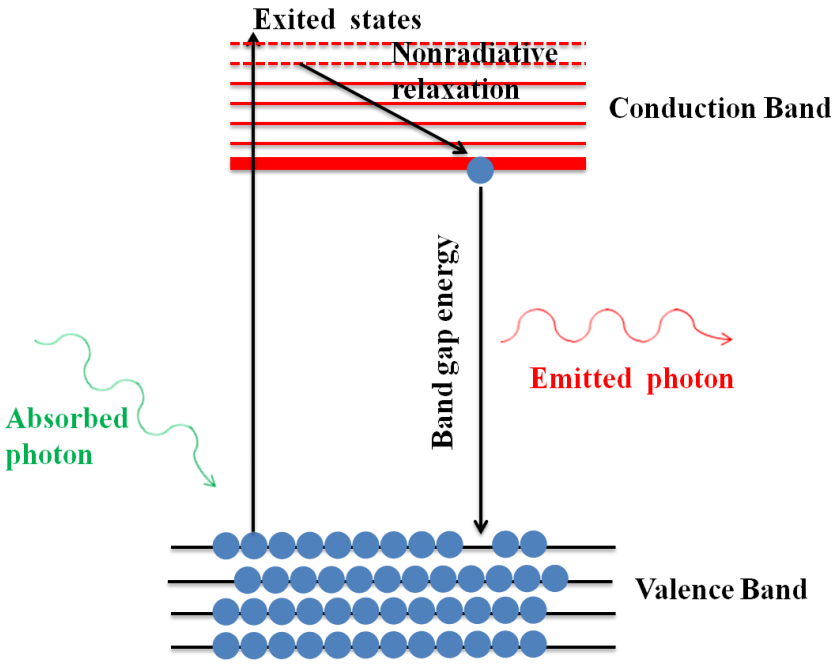

Figure 19. Radiative electron-hole recombination scheme

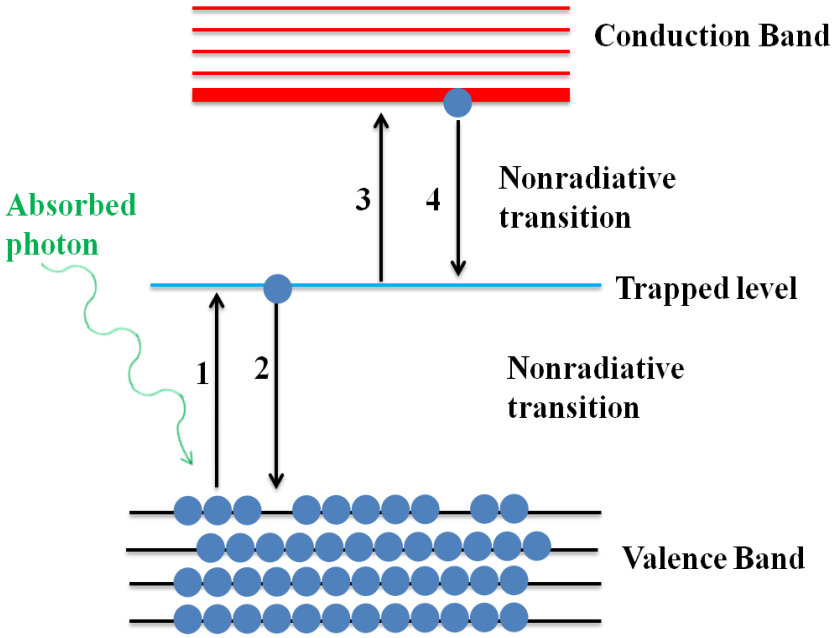

Figure 20. Non-radiative electron-hole recombination scheme, (1) hole emission (an electron jumps from the valence band to the trapped level), (2) hole capture (an electron moves from an occupied trap to the valence band, a hole disappears), (3) electron emission (an electron jumps from trapped level to the conduction band), (4) electron capture (an electron moves from the conduction band to an unoccupied trap) [87].

CHAPTER V. RESULTS AND DISCUSSION

5.1 Bare and doped ZnO powders and films

5.1.1 Bare and Co- doped ZnO powders and films.

5.1.1.1 Bare and Co- doped ZnO powders

A. Thermogravimetric Analyses

Figure 21 shows the TGA profiles for the precursor powders containing Co ions at atomic percentages between 0 at% and 10 at%. The shape of these profiles suggests a single thermal decomposition path which ends at approximately 350ºC. The fact that a single decomposition path was observed suggests the feasibility of achieving atomic blending of the dopants in the host oxide phase

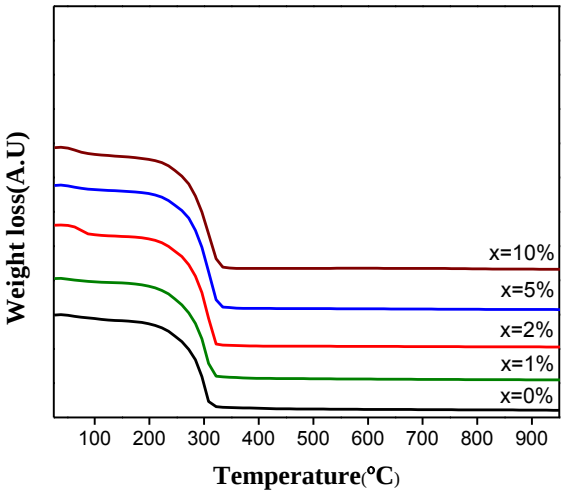

Figure 21. TGA profiles for precursor solids containing various atomic percentages, *x*, of pure and Co- doped ZnO. The heating rate was 10ºC / minute.

B. Structural Properties:

Figure 22 shows the XRD patterns of cobalt doped ZnO powders synthesized by the sol-gel method at different dopant concentration of Co ions, Figure 22(a) at annealing temperature of 400ºC and Figure 22(b) at 500ºC for 1hour on Air in all tests. All the peaks corresponding to

wurtzite structure of ZnO were observed. The absence of other isolated phases may suggest the possible incorporation of Co^{2+} within the ZnO host. However, considering that the ionic radius of Co^{2+} (0.72Å) is similar that Zn^{2+} (0.74Å), a complete incorporation of Co ions in the ZnO host could be suggested. The corresponding lattice parameters show a random behavior with the dopant concentration *x* as observed in Figure 23(a) and Figure 23(b). Moreover, all the XRD peaks do not present a shift and appear more or less on the same angular position.

The lattice parameter values exhibited a random variation with the nominal Co^{2+} contents, *x*, no appreciable effect on *c* and *a* parameters was observed con respect to pure ZnO. In addition the average crystallite size, estimated by using Scherrer's equation, varied between 25.90±0.15 and 30.43±1.15 nm when the annealing temperature was increased from 400ºC to 500ºC for pure ZnO. As can be seen in Table 1 the incorporation of the Co species does not influence appreciable changes the average crystallite size. Moreover, it can be seen in the diffraction patterns that there is not a noticeable widening in the peaks respect to the pure material.

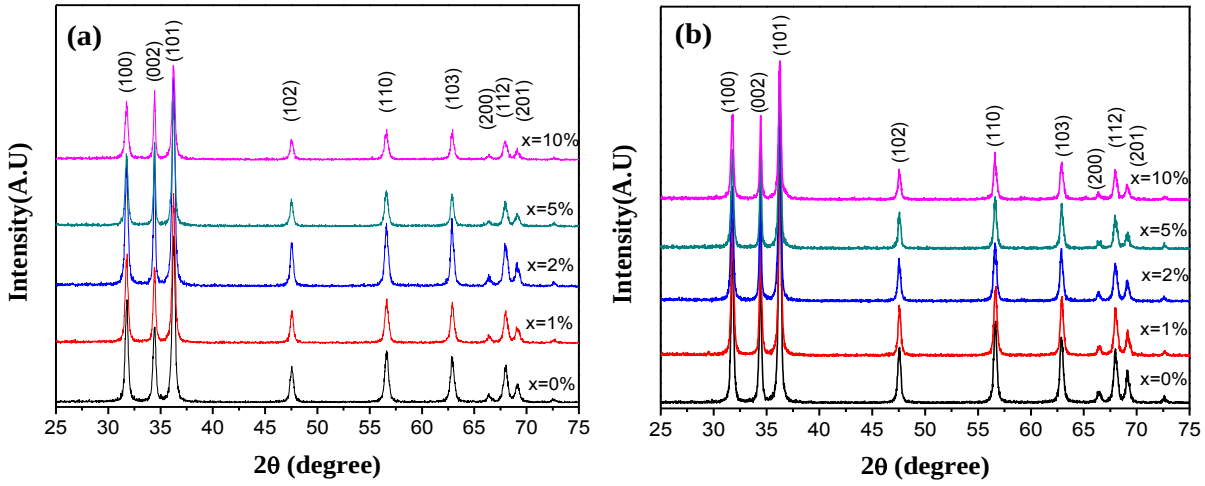

Figure 22. XRD patterns of Co^{2+}-doped ZnO powders synthesized at various dopant atomic percentages, *x*. The corresponding annealing temperatures were 400ºC (a), and 500ºC (b).

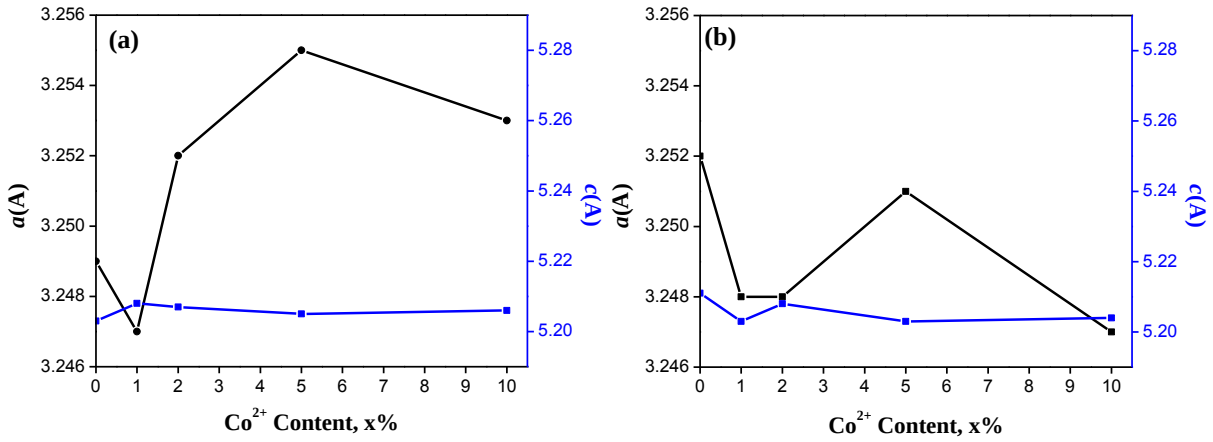

Figure 23. Variation of the lattice parameters of ZnO powders with Co^{2+} ions content, *x*. The corresponding annealing temperatures were 400ºC (a), and 500ºC (b).

Table 1 Average crystallite size (± stdev) nm of Cobalt doped ZnO powders.

x= Co at%	T=400ºC	T=500ºC
0%	25.90 ± 0.15	30.43 ± 1.15
1%	28.54 ± 3.14	30.66 ± 3.54
2%	28.53 ± 3.15	30.67 ± 3.63
5%	30.00 ± 4.02	32.08 ± 2.41
10%	29.42 ± 4.63	31.32 ± 2.88

C. Optical Properties

Figure 24 shows the room-temperature PL spectra of pure and Co-doped ZnO powders at different dopant concentrations and annealed at 400ºC (a), and 500ºC (b). The principal emission band is in the UV region centered on 390 nm and was clearly identified in all samples. No other band in the visible region was observed in our samples. This fact may suggest that the developed synthesis route did not favor the creation of defects in the structure usually associated with the

luminescence in the visible region. However, a strong dependence of the emission band intensity as function of Co concentration was evidenced. The intensity of this emission band decreases as the dopant concentration increases, this suggest a quenching-by-concentration effect. This quenching in photoluminescence has been observed in other systems [89] when the concentration of the dopant becomes so high that the probability of non-radiative transition through trapping states exceeds the probability of radiative transition. It causes the excitation energy to start migrating through lattice vibrations [90]. The major decrease in the principal emission was observed in Co- (5 at%) doped ZnO at 400ºC, the decrease was 86% relative to pure ZnO. The quenching of UV emission band is presented qualitatively in the Figure 25(a). To samples annealed at 500ºC the major decrease was 87% for Co- (5 at%) doped ZnO, the quenching of UV emission band is shown in the Figure 25(b).

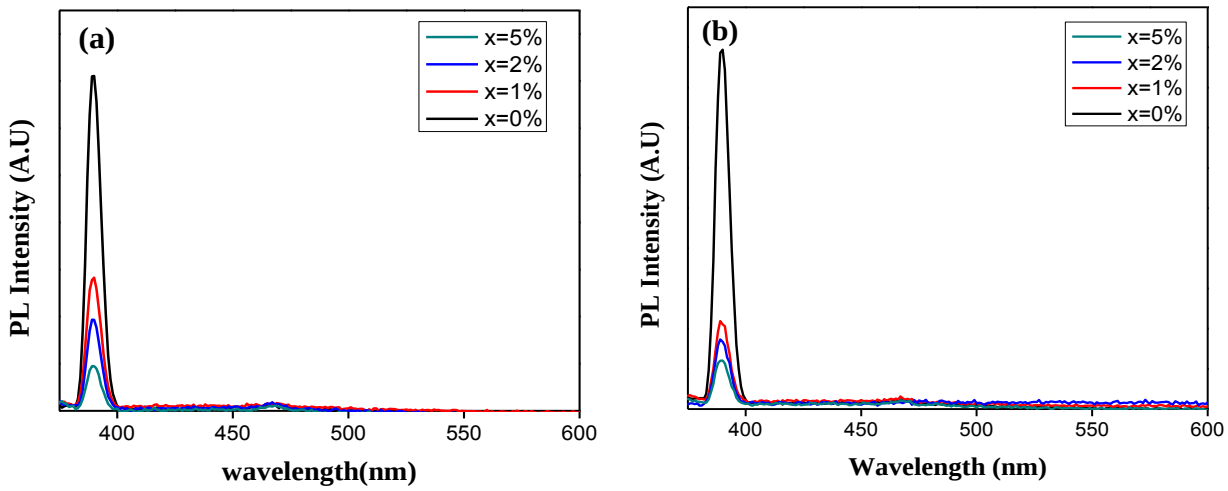

Figure 24. Room-temperature PL spectra for Co^{2+}-doped ZnO powders, at different dopant concentrations *x*, annealed at 400ºC (a), and annealed at 500ºC (b).

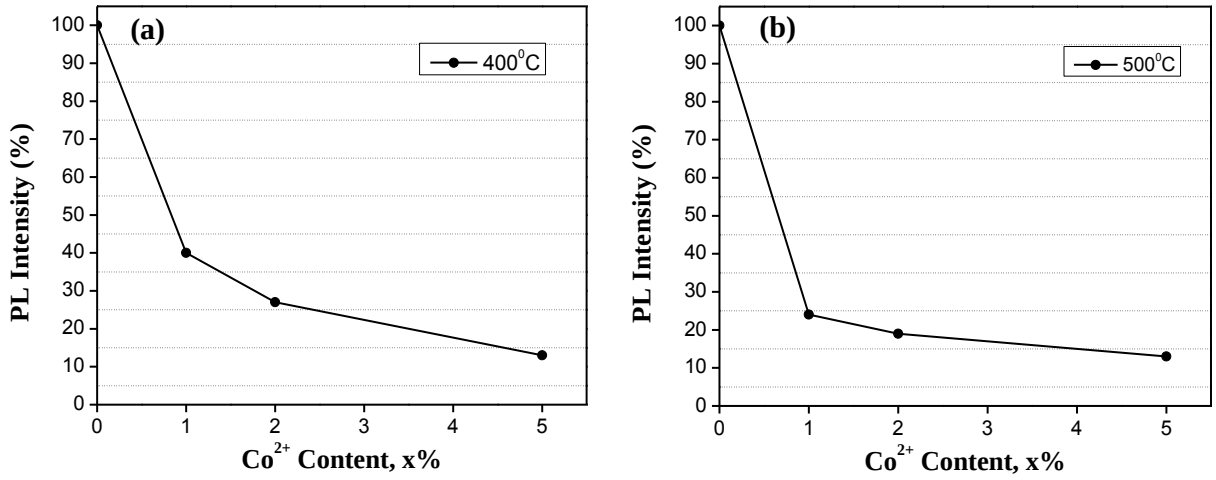

Figure 25. Room-temperature PL relative intensity for Co^{2+}-doped ZnO powders, at different dopant concentrations *x*, annealed at 400ºC (a), and annealed at 500ºC (b).

Furthermore the quenching in the UV emission is not dependent on the annealing temperature but depends only on the dopant concentrations. In both cases 5 at% is the dopant concentration threshold to retain optical property for this synthesis process.

D. Magnetic Properties.

Figure 26 shows measurements at different dopants level M-H loops of Co^{2+} doped ZnO powders annealed at 500ºC for 1hour. Subtraction of the diamagnetic components was made to all the samples except to 5 at% measurement. These samples exhibited a weak ferromagnetic behavior with coercivity and saturation magnetization values shown in Table 2. The sample doped with 5 at% of Co exhibited a predominant paramagnetic behavior, which became more pronounced at larger external magnetic fields. Similar trends were observed by other researchers in Co-doped ZnO [91]. Available literature suggests that ferromagnetism in DMSs would be established only at concentrations that lie far below the percolation threshold (x_p maximum level

of doping). The percolation threshold is associated with nearest-neighbor cation coupling and above of this threshold there is a change in the magnetic features of the DMSs like present a paramagnetic response [17]. This ferromagnetic behavior could be attributed to the super exchange interaction through oxygen (TM-O^{2-}-TM), where TM are the Co^{2+} ions, or to the exchange interaction between electron's spins of carriers and localized spin of Cobalt ions, which contribute with $6\mu_B$/ion. Furthermore Sato and Katayama-Yoshida [92] predicted that the ferromagnetic state Co^{2+} (d^7) in Co-doped ZnO could be stabilized by *s*–*d* hybridization, pointing to the possibility that high-Curie-temperature ferromagnetic materials could be realized in *n*-type ZnO as well. This weak ferromagnetic behavior cannot be attributed to the presence of parasite phases as oxides since there is good spectroscopic evidence that divalent cobalt does indeed substitute on the tetrahedral sites of the wurtzite structure [66,93], with a wide solid solubility range.

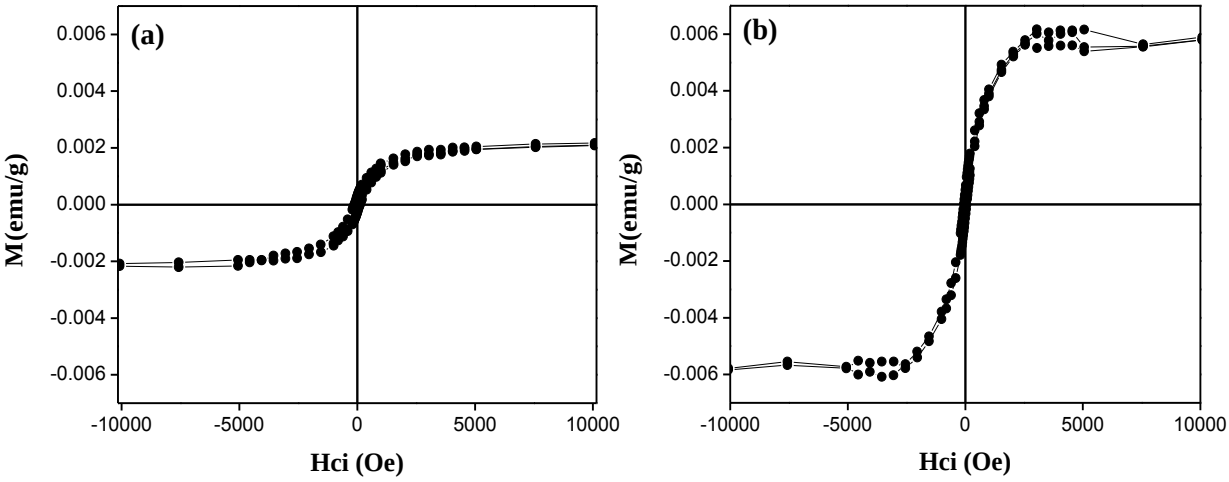

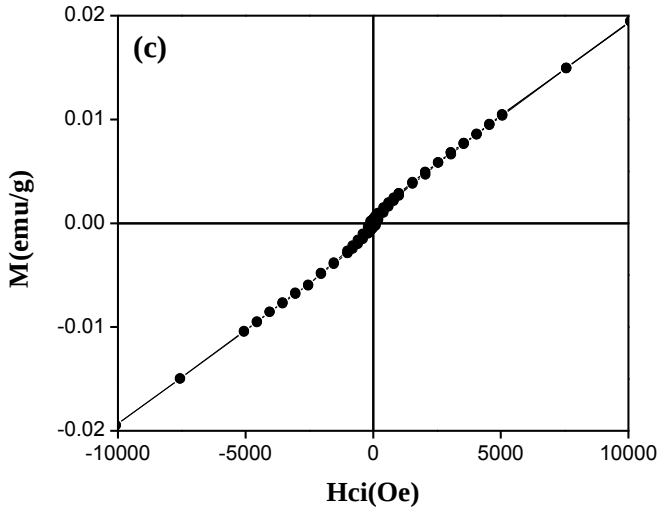

Figure 26. Room-temperature M-H loops of Co^{2+} doped ZnO powders, at different concentrations of Cobalt ions and annealing temperature of 500ºC, 1% (a), 2% (b), and 5% (c).

Table 2 Magnetic properties at room temperature of Cobalt doped ZnO powders. The annealing temperature was 500ºC.

x= Co at%	Coercivity (Oe)	Maximum Magnetization (emu/g)
1%	117	0.002
2%	66	0.006

5.1.1.2 Bare and Co- doped ZnO films

A. Structural Properties

The X-ray diffractograms recorded from the Co-doped ZnO/Quartz thin films (0, 1, 2, and 5 at%) annealed at 500ºC and 550ºC are shown in Figure 27. These thin films have 20 layers and a thickness around 1000 nm measured with a profilometer. All diffractions peaks correspond to the host ZnO phase with a hexagonal wurtzite structure. The absence of impurity phases suggests the actual incorporation of Co^{2+} (0.72 Å) in the Zn^{2+} (0.74 Å) site. This incorporation of Cobalt ions into the oxide lattice was also suggested by the slight but noticeable shift in the (002) XRD peak from 34.431 to 34.502, when the Co^{2+} doping level was increased from 0 to 5 at% and

annealed at 500ºC. And a shift from 34.469º to 34.516º for films at the same conditions but annealed at 550ºC. A similar shift in cobalt doped ZnO films has been described by Jinghai Yang *et al*. [59] explaining that this shift happens because the cobalt radius is a little smaller than Zn^{2+}. The shift also revealed that there was no octahedral cobalt in the sample because the radius of octahedral cobalt is bigger that zinc, so the peaks of ZCO should shift to lower angles, which was opposite to their result, since Co^{2+} substitutes for Zn^{2+} without changing the wurtzite structure. Also in our case these shifts to the right obey to a decrease in the lattice parameter *c* from 5.205Å (pure ZnO) to 5.195Å for the 5 at% Co-doped ZnO annealed at 500ºC. A similar behavior was observed for the films annealed at 550ºC. The average crystallite size is shown in Table 3, and it is observed that Co ions do not present an effect on the average crystallite size similar to the results for Co doped ZnO powders. The preferential growth of the (002) plane of the hexagonal ZnO unit cell, was clearly evidenced in those samples synthesized in presence of Co ions.

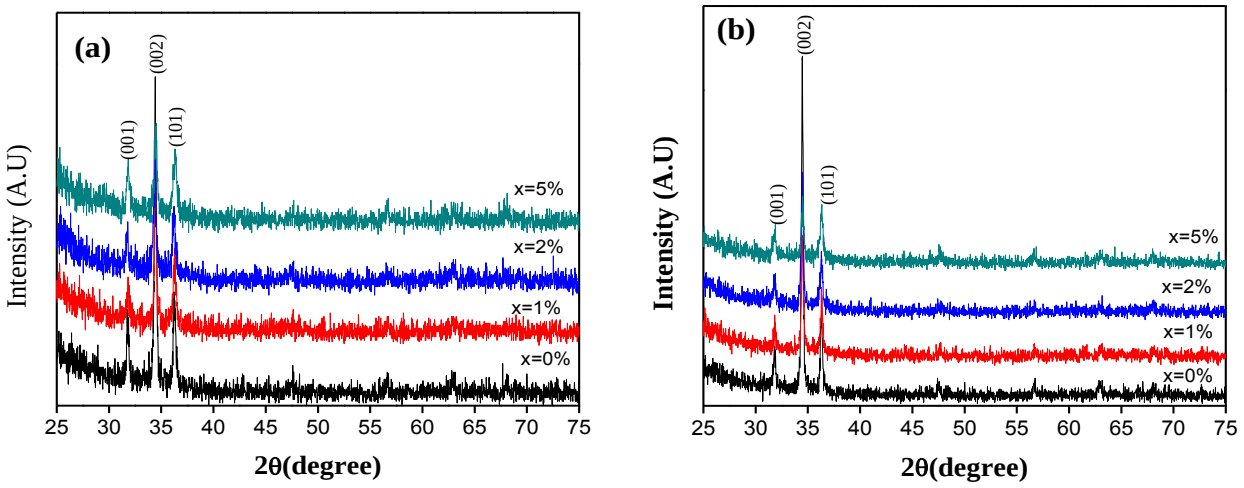

Figure 27. XRD patterns of Co^{2+} -doped ZnO/quartz films synthesized at various dopant atomic percentages, *x*. The corresponding annealing temperatures were 500ºC (a), and 550ºC (b).

Table 3 Average crystallite size (± stdev) nm of Cobalt doped ZnO/quartz films.

x= Co at%	T=500ºC	T=550ºC
0%	24.43±0.14	27.72±1.54
1%	23.12±1.24	25.45±0.77
2%	26.02±1.47	24.43±0.14
5%	21.53±1.54	21.74±2.84

B. Optical Properties

B.1 Absorbance measurements

The UV-vis spectra of doped and pure ZnO/quartz films at different concentration ions of Co^{2+}, clearly showed the absorption peak corresponding to an exciton. Figure 28(a) shows films annealed at 500ºC, and Figure 28(b) at 550ºC. In both cases the absorption peak was slightly blue-shifted when larger contents of Co^{2+} species were contained in the films. This effect can be attributed to dopants, which produce superficial defects causing changes in the optical properties [94]. Also this blue-shift in the absorption peak is usually attributed in ZnO based DMS by many researchers to the Moss-Burstein effect [95,96], which is related to an apparent increase in the band-gap. This effect takes place when the carrier concentration exceeds conduction band edge density of states, due to doping, moving the Fermi level above the donor sates. As the doping concentration is increased, more donor states are generated and place the Fermi level higher in energy until it lies within the conduction band above the occupied donor states. Pauli principle, when an electron is excited from the valence band cannot fill these states because are occupied and only can go to a higher empty state inside the conduction band, consequently then blue shifts can be observed in the measurements [97].

The band gap energy was estimated using Tauc's relationship [84]. The extrapolation to determine the band gap values is presented in Figure 29(a) 500ºC, and Figure 29(b) 550ºC. The

band gap energy was in the range of 3.27 eV – 3.32 eV for pure and Co 5 at% doped ZnO films respectively annealed at 500ºC and samples annealed at 550ºC showed a similar behavior. These band gap values are close to bulk value 3.3 eV. Our results agree with the work performed by D. Paul Joseph *et al.* [98], who have reported the blue shift in Co doped ZnO. The band gap values as a function of the dopant concentration are presented in Table 4.

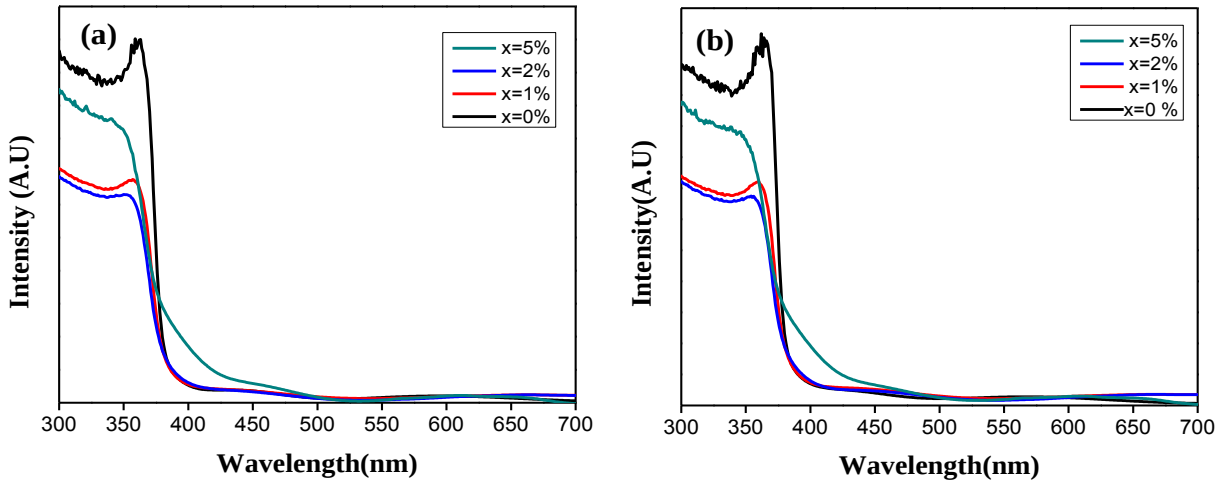

Figure 28. UV-Vis of Co^{2+}-doped ZnO/quartz films synthesized at various dopant atomic percentages, *x*. The corresponding annealing temperatures were 500ºC (a), and 550ºC (b).

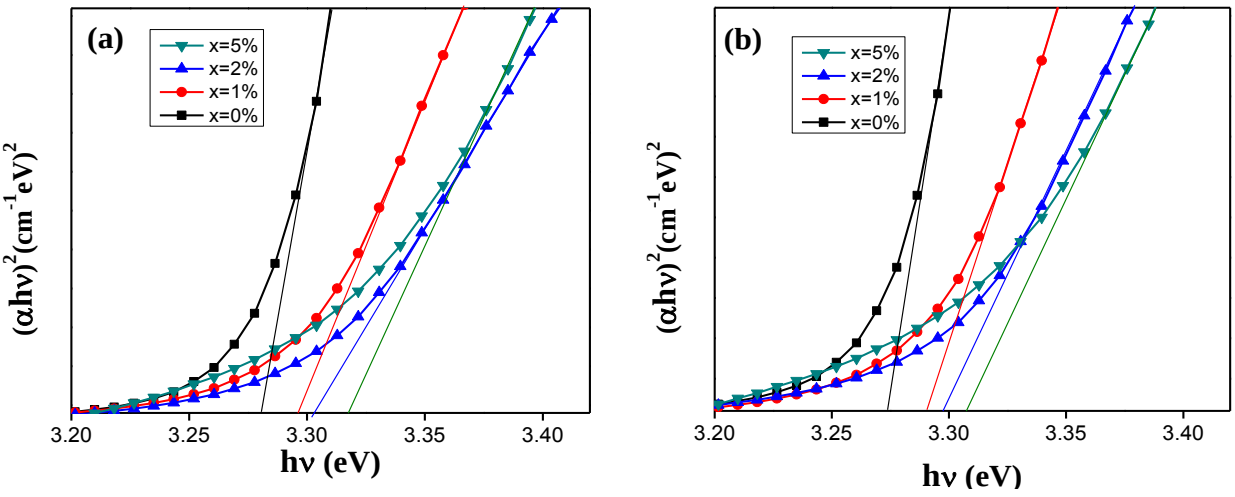

Figure 29. Estimation of the optical band gap energy of pure and Co-doped ZnO films at different concentration and annealing temperature: 500ºC (a), and 550ºC (b). The samples were annealed for 1 hour.

Table 4 Estimated Band gap energy values of Cobalt doped ZnO/quartz films.

x= Co at %	E_g(eV) at 500ºC	E_g(eV) at 550ºC
0%	3.27	3.27
1%	3.29	3.28
2%	3.30	3.29
5%	3.32	3.31

B.2 Photoluminescence measurements

Figure 30 shows the room-temperature PL spectra of pure and Cobalt doped ZnO/quartz thin films annealed at 500ºC (a) and 550ºC (b). The spectra were recorded with an excitation wavelength of 342 nm. As seen, an evident emission band in the UV region centered on 390 nm was clearly identified in all samples. Other band in the visible region is only present in pure ZnO. This band is usually attributed to lattice defects, but the type of defect is controversial, most of the times this visible band is attributed to oxygen vacancies [99,100]. Recently, theoretical works attribute this band to zinc vacancies because this type of defect needs lower formation energy than oxygen vacancies or zinc interstitials [88]. This idea lead us to the following interpretation: an actual substitution of the dopant species in the zinc sites was produced vanishing the zinc vacancies (which are present in pure ZnO) and therefore dropping the visible emission in the doped samples. In addition, many researchers suggest that the intensity of the UV and Visible emission bands is related to superficial defects including surface band bending, native surface defects states, surface roughness and grain size [101-104].

A strong dependence of the UV emission band intensity on the Co concentration was evidenced; this ban intensity became negligible to 5 at% Co, suggesting a quenching-by-dopant concentration effect. This quenching in photoluminescence has been observed in other works [105, 106]. Furthermore A. Wang *et al.* [107] have reported for Co- doped ZnO films that the intensity of the UV emission peaks decreases with the doped concentration increasing. These

authors suggest that this could be due to the inferior quality sample, as well as more defect states below the conduction band occurred by Co doping, so that some of the excited electrons in the conduction band relax to the defect states, leading to decrease in UV emission intensity. Therefore it is inferred from our results that, at high dopant concentrations there is a higher probability of trapping states formation, since these trapping states originate a migration of the excitation energy through the lattice, as was discussed in the previous photoluminescence section. In the analysis for the principal emission we observed in Co- (5 at%) doped ZnO at 500ºC a decrease of 89% in the UV emission intensity relative to pure ZnO. The quenching of UV emission band is presented qualitatively in Figure 31(a). For samples annealed at 550ºC the major decrease was 96% for Co- (5 at%) doped ZnO, since this sample presented a higher crystallinity and consequently the probability of trapped states is higher. The quenching of UV emission band is shown in Figure 31(b).

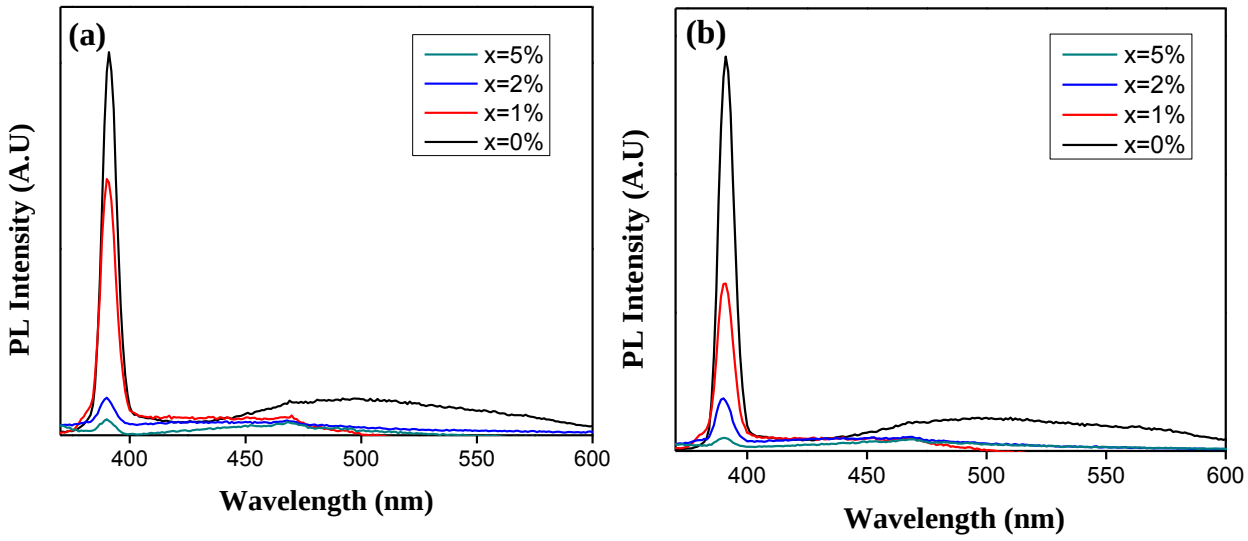

Figure 30. Room-temperature PL spectra of Co^{2+}-doped ZnO/quartz films synthesized at various dopant atomic percentages, *x*. The corresponding annealing temperatures were 500ºC (a), and 550ºC (b).

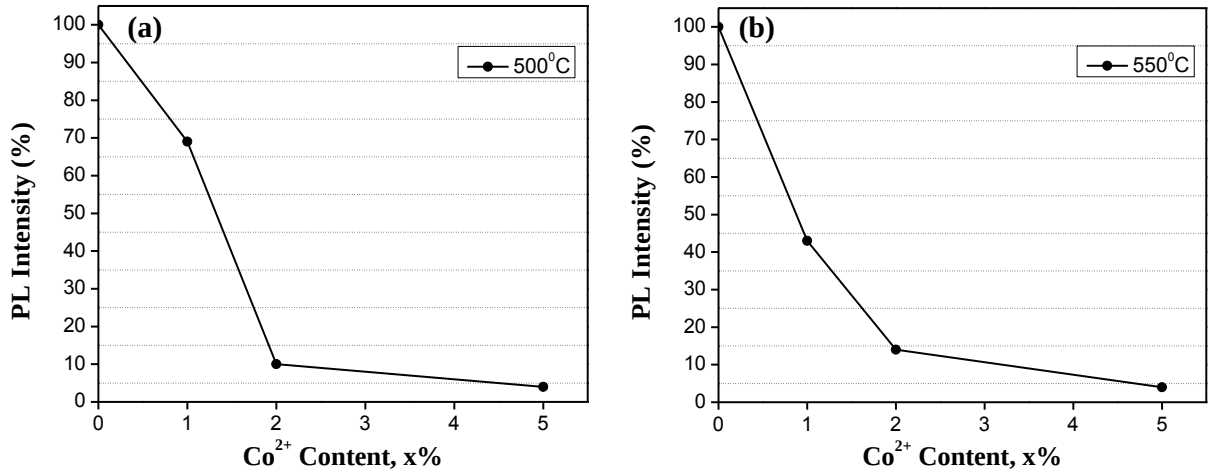

Figure 31. Room-temperature PL relative intensity for Co^{2+}-doped ZnO films, at different dopant concentrations *x*, annealed at 500ºC (a), and annealed at 550ºC (b).

5.1.2 Bare and Sc- doped ZnO powders and films

5.1.2.1 Bare and Sc- doped ZnO powders

A. Thermogravimetric Analysis

Figure 32 shows the TGA profiles for the precursor powders containing Sc ions at atomic percentages between 0 at% and 10 at%. The weight loss as a function of temperature is shown, the first slight amount of weight loss corresponds to the evaporation of adsorbed water and solvent at the range 100ºC-200ºC, The second step represents the most important weight loss and can be attributed to the removal of residual precursors at the range 200ºC-350ºC. After 350ºC the samples reach a stable phase, in our case a possible oxide formation. The shape of these profiles suggests a single thermal decomposition path which ends at approximately 350ºC.

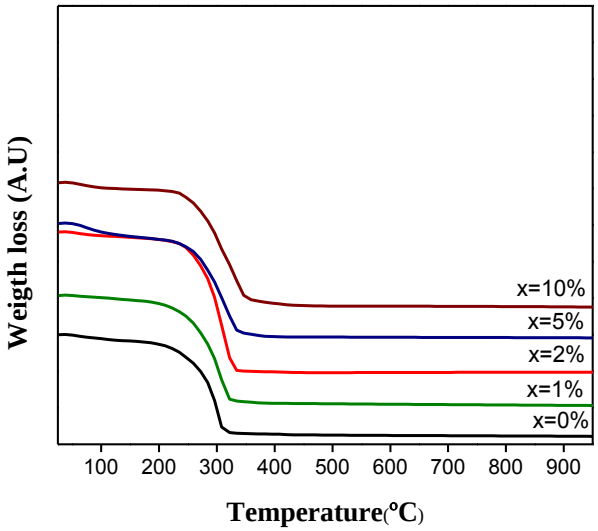

Figure 32. TGA profiles for precursor solids containing various atomic percentages, *x*, of pure and Sc- doped ZnO. The heating rate was 10ºC / minute.

B. Structural Properties

Figure 33 shows XRD patterns of scandium doped ZnO powders synthesized by the sol-gel method at different dopant concentration of Sc ions, Figure 33(a) at annealing temperature of 400ºC and Figure 33(b) at 500ºC for 1hour on Air in all samples. All peaks corresponding to the wurtzite structure of ZnO were observed. The absence of other isolated phases may suggest the possible incorporation of Sc^{3+} within the host ZnO. However, considering that the ionic radius of Sc^{3+} (0.745Å) is equal that Zn^{2+} (0.74Å). The corresponding lattice parameters show a random behavior with the concentration *x* in Figure 34(a) and Figure 34(b) similar to the behavior in the cobalt doped ZnO system. No appreciable effect on *c* and *a* parameters was observed with respect to pure ZnO. Moreover all the XRD peaks do not show a shift and remain in the same angular position. Therefore, although actual incorporation of Sc^{3+} ions into the ZnO produces a noticeable decrease in the crystallite growth, this can be attributed to the fact that Sc ions originate an effect in the reaction kinetics, slowing the growth process of crystallite. The average

crystallite size crystals for pure and doped ZnO at the two annealing temperatures are shown in Table 5.

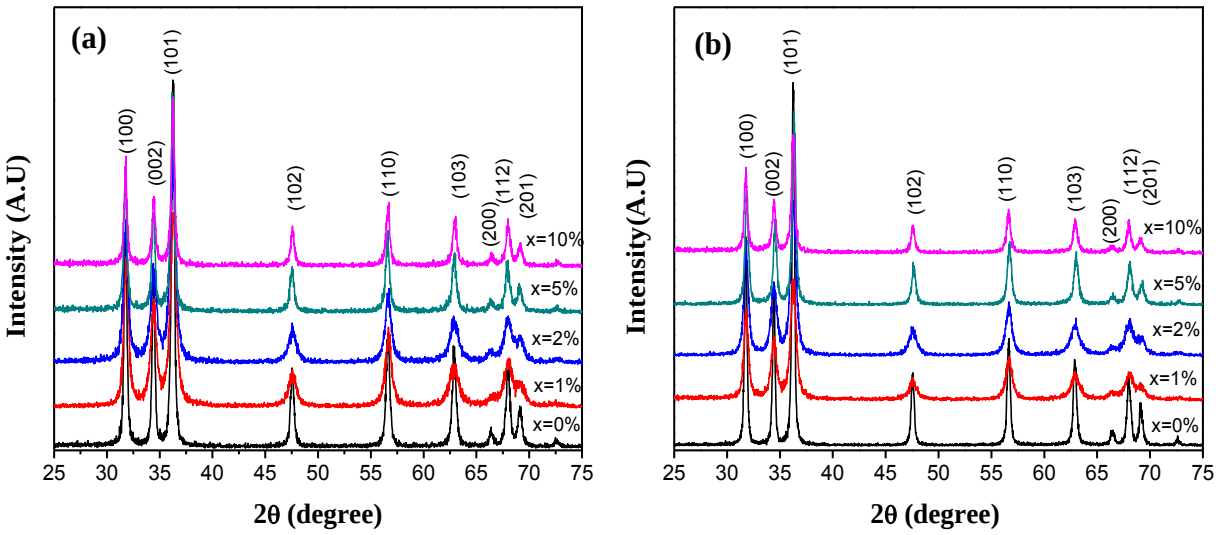

Figure 33. XRD patterns of Sc^{3+} -doped ZnO powders synthesized at various dopant atomic percentages, *x*. The corresponding annealing temperatures were 400ºC (a), and 500ºC (b).

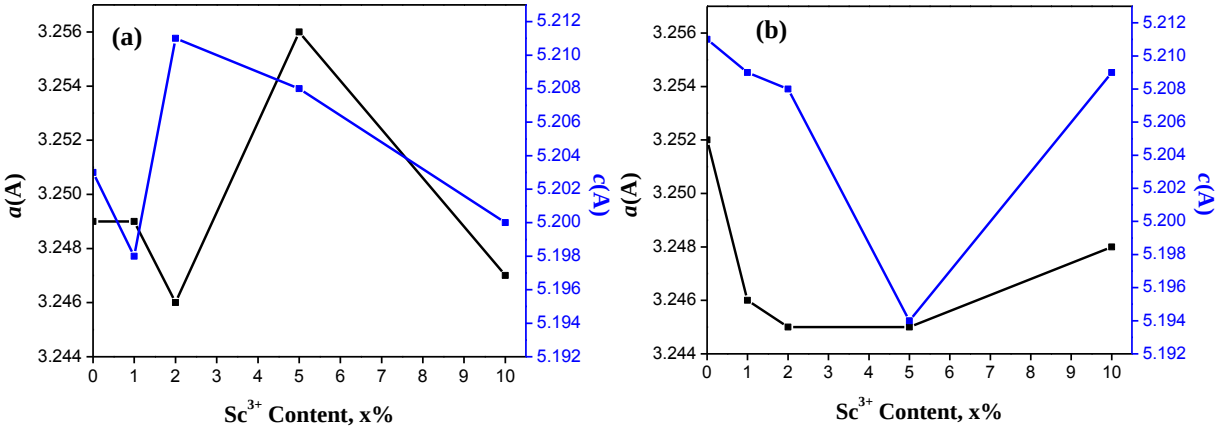

Figure 34. Variation of lattice parameters of ZnO powders with Sc^{3+} ions content, *x*. The corresponding annealing temperatures were 400ºC (a), and 500ºC (b).

Table 5 Average crystallite size (± stdev) nm of Scandium doped ZnO powders.

x = Sc at%	T=400ºC	T=500ºC
0%	25.90 ± 0.15	30.43 ± 1.15
1%	15.31 ± 1.63	16.08 ± 1.65
2%	16.02 ± 1.03	15.84 ± 1.22
5%	20.77 ± 0.12	20.77 ± 0.11
10%	20.77 ± 0.13	20.80 ± 0.97

C. Optical properties

Figure 35 shows the room-temperature PL spectra of pure and Sc-doped ZnO powders at different dopant concentrations and annealed at 400ºC Figure 35(a), and 500ºC, Figure 35(b). Like in Cobalt systems only, an emission band in the UV region centered on 390 nm was clearly identified in our samples. No additional emissions in the visible region were observed. This suggests that our samples do not present structural defects because the synthesis process is the same than for cobalt system. Also, a strong dependence of the principal emission band intensity on the Sc concentration was again evidenced. The intensity of this emission band decreases as dopant concentration increases, this suggest a quenching-by-concentration effect [106]. The major decrease in the principal emission was observed in Sc- (5 at%) doped ZnO at 400ºC, the decrease was 76% with respect to pure ZnO, the quenching of UV emission band is presented qualitatively in Figure 36(a). In samples annealed at 500ºC the major decrease was 90% for Sc- (5 at%) doped ZnO, the quenching of UV emission band is shown in Figure 36(b). This drastic decrease in the UV intensity of Sc- (5 at%) doped ZnO could be also attributed to the smaller crystallite size respect to the pure ZnO powder [108].

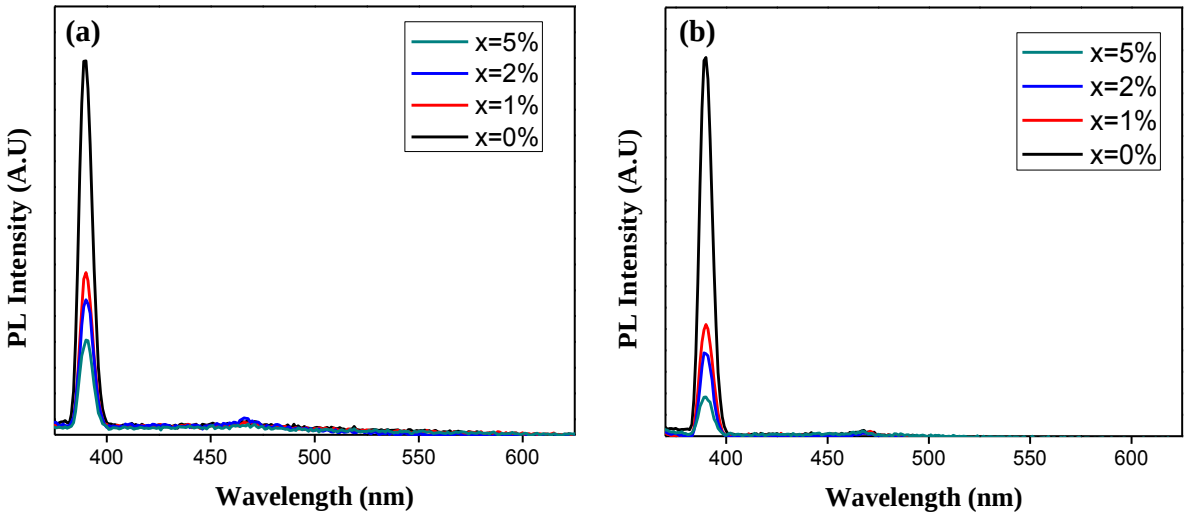

Figure 35. Room-temperature PL spectra for Sc^{3+}-doped ZnO powders, at different dopant concentrations *x*, annealed at 400ºC (a), and annealed at 500ºC (b).

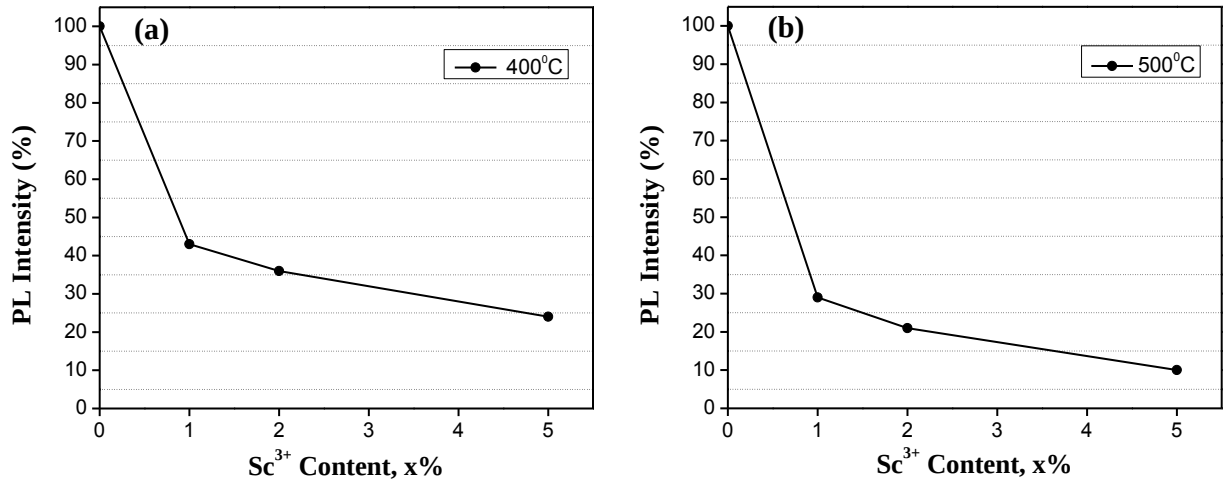

Figure 36. Room-temperature PL relative intensity for Sc^{3+}-doped ZnO powders, at different dopant concentrations *x*, annealed at 400ºC (a), and annealed at 500ºC (b).

D. Magnetic properties

Figure 37 shows measurement at different dopants level of M-H loops of Sc^{3+} doped ZnO powders annealed at 500ºC for 1 hour for each sample. A subtraction of the diamagnetic contribution was made to all the samples. These samples exhibited a weak ferromagnetic behavior with coercivity and saturation magnetization values shown in Table 6. This effect is not evident since the calculation of the effective magnetic moment to Sc^{+3} is zero, no electrons in the

d-shell, so it would not be expected a direct contribution to ferromagnetic behavior. This magnetic behavior can be possibly attributed to structural defects as discussed in literature. Various materials such as carbon, hexaborides (AB_6, A= Ca, Ba, Sr), HfO_2 have been studied which present a ferromagnetic response at room temperature despite having a d^0 shell. There have also been reports that Sc^{3+}-or Ti^{4+}-doped ZnO present ferromagnetism at room temperature as shown in Figure 38 [64] and also these ions possess a d^0 shell. Among all the hypotheses to explain the ferromagnetism in these systems a common feature is the presence of lattice defects [109]. This hypothesis proposes that intermediate states in the gap of semiconductors can be created due to defects and are sufficiently numerous to induce the formation of an 'impurity band'.

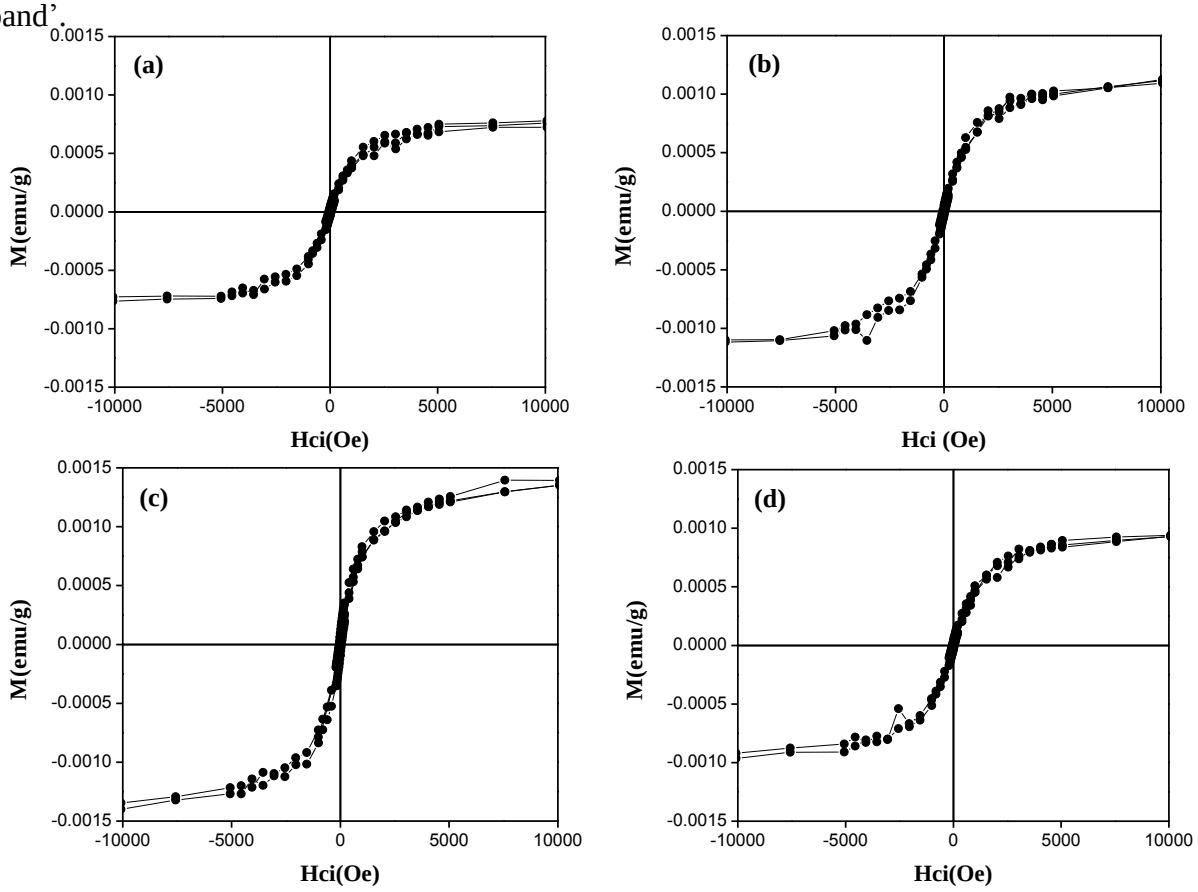

Figure 37. Room-temperature M-H loops of Sc^{3+} doped ZnO powders, at different concentrations of Scandium ions and annealing temperature at 500ºC: 1% (a), 2% (b), 5% (c), and 10% (d).

Coey proposes that defect states are those that originate magnetic moments associated with molecular orbitals localized in the vicinity of the defects [109]. Then, as these sates arise the impurity band needs to mediate a long-range ferromagnetic interaction between them. Also, the impurity band is not necessarily metallic; this band can propagate the exchange provided the localization length is less than the distance between the defects. On this basis, the ferromagnetic behavior in Sc-doped ZnO could be considered a consequence of the overlapping with the impurity band that leads to some population of the empty 3d band. This change induced in the 3d band would be responsible of the spin polarization of the impurity band and the establishment of a d^{ε} ferromagnetism, where $\varepsilon<<1$. [109]. Figure 39 describes the proposed mechanisms.

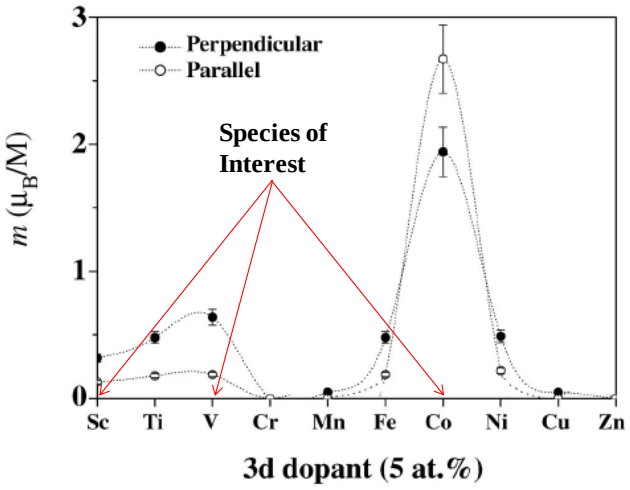

Figure 38. Magnetic moment of ($Zn_{1-x}M_xO$) films, *M*= Sc*;* Ti*; . . . ;* Cu*;* Zn, measured at room temperature. Solid circles are for the field applied perpendicular to the film plane and open circles are for the field applied in the plane of the film. The moment is expressed as μ_B/M [64].

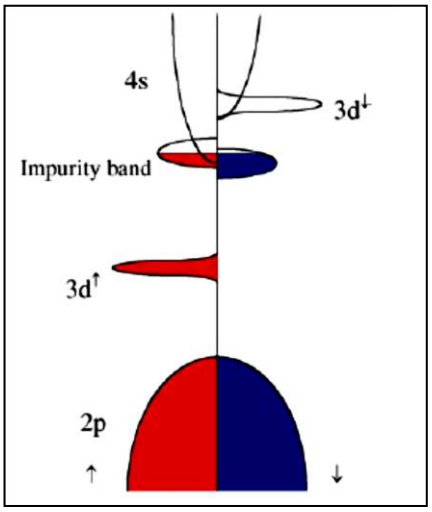

Figure 39. Population of an unoccupied *"d" band* by overlap with an impurity band, which leads to spin splitting [109]

Table 6 Magnetic properties at room temperature of Scandium doped ZnO powders. The annealing temperature was 500ºC.

x = Sc at%	Coercivity (Oe)	Maximum Magnetization (emu/g)
1%	50	0.0007
2%	49	0.0011
5%	50	0.0013
10%	50	0.0009

5.1.2.2 Bare and Sc- doped ZnO films

A. Structural properties

The XRD patterns of Sc-doped ZnO/Quartz thin films synthesized at various dopant concentrations and annealing temperatures of 500ºC and 550ºC are shown in Figure 40(a) and Figure 40(b), respectively. The films reported a thickness of around 1000 nm. All diffractions peaks correspond to the ZnO host, which exhibits a hexagonal wurtzite structure. The absence of secondary phases suggests the actual incorporation of Sc^{3+} (0.745Å) to the Zn^{2+} (0.74Å) sites. In this case, the incorporation of Sc ions made the average crystallite size decrease as is presented in the Table 7. This suggests that the Sc ions influence in the kinetic reaction lowering the crystal

growth and it can also be noticed in the widening of the peak in the diffractograms. The lattice parameters for pure and doped systems did not exhibit a drastic variation; *a* and *c* values were 3.249 Å and 5.205 Å, respectively. This can be a consequence that the ionic radii are similar for Scandium ions and Zinc ions. The enhanced intensity of the (002) peak, observed in the XRD patterns of Sc-doped ZnO films, may indicate the promoted growth of this plane in the films since thermodynamically this direction is the most favorable because of the lower surface energy of the (002) plane [110].

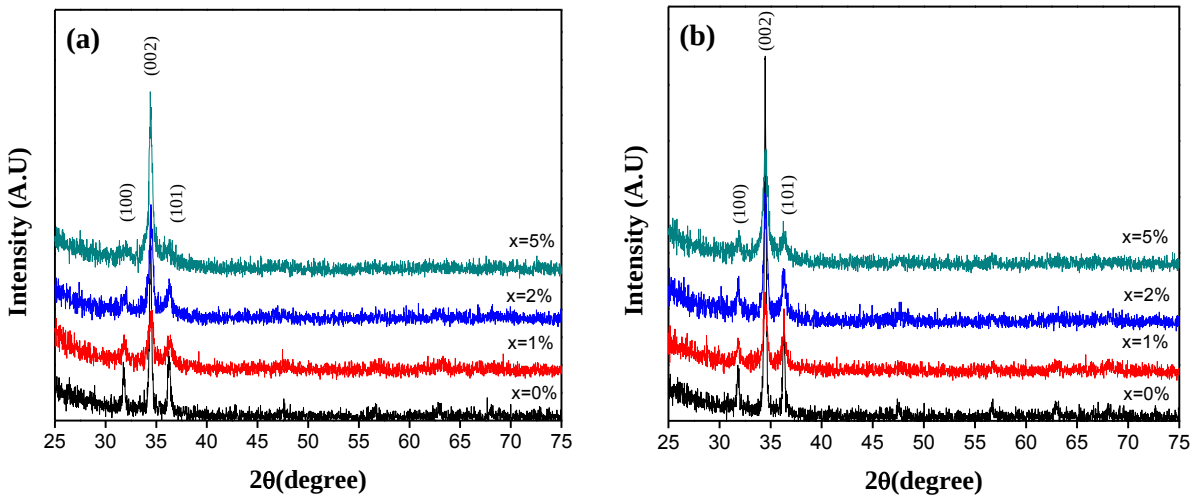

Figure 40. XRD patterns of Sc^{3+} -doped ZnO/quartz films synthesized at various dopants atomic percentages *x*. The corresponding annealing temperatures were 500ºC (a), and 550ºC (b).

Table 7 Average crystallite size (± stdev) nm of Scandium doped ZnO/quartz films.

x = Sc at%	T=500ºC	T=550ºC
0%	24.43±0.14	27.72±1.54
1%	14.14+1.64	16.63+0.60
2%	16.05+0.86	16.61+0.10
5%	17.52	14.38

B. Optical Properties

B.1 Absorbance measurements

The UV-vis spectra of pure and Sc^{3+} doped ZnO/quartz films at different concentrations clearly showed the absorption peak corresponding to an exciton with annealed temperatures at 500ºC Figure 41(a), and 550ºC Figure 41(b). In both cases the absorption peak was slightly blue-shifted when larger contents of Sc^{3+} species were contained in the films, a similar result was obtained by Sharma et al. [111]. One of the reasons for this effect is due to the fact that the doping species slows the crystal growth, which is in agreement with the XRD results. Also it can be related to the Moss-Burstein effect discussed previously. The band gap energy was estimated using Tauc's relationship [84]. The extrapolation to determine the band gap values is presented in Figure 42(a) 500ºC and Figure 42(b) 550ºC. The band gap energy was in the range of 3.27eV – 3.30 eV for pure and Sc 5 at% doped ZnO films respectively annealed at 500ºC. For samples annealed at 550ºC there was not an evident change in the band gap value, since all samples exhibited band gap values are close to bulk value 3.3eV. These results suggest that our samples retain the intrinsic semiconductor properties. The band gap energy was estimated as in the previous case, as shown in the Table 8.

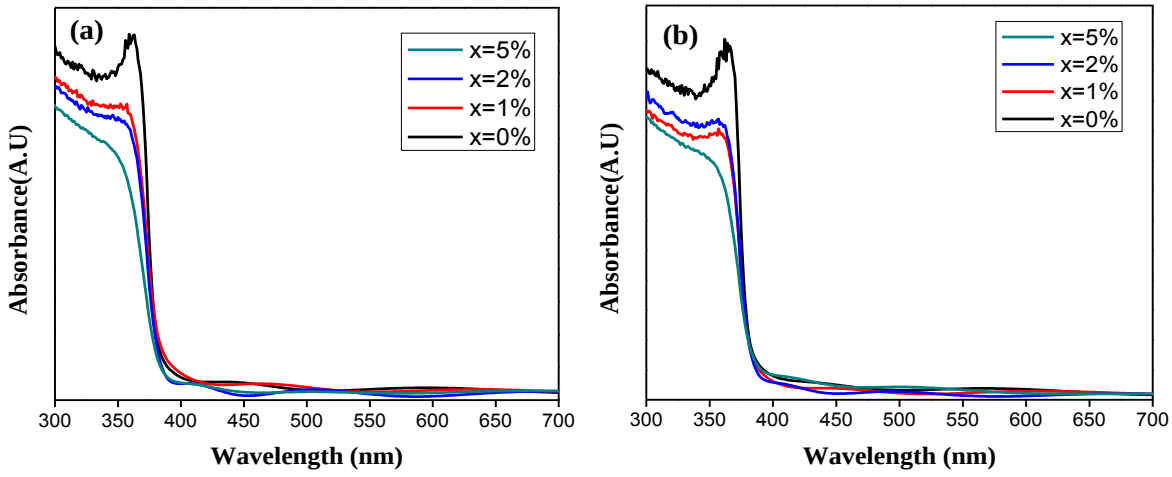

Figure 41. UV-Vis of Sc^{3+}-doped ZnO/quartz films synthesized at various dopants atomic percentages *x*. The corresponding annealing temperatures were 500ºC (a), and 550ºC (b).

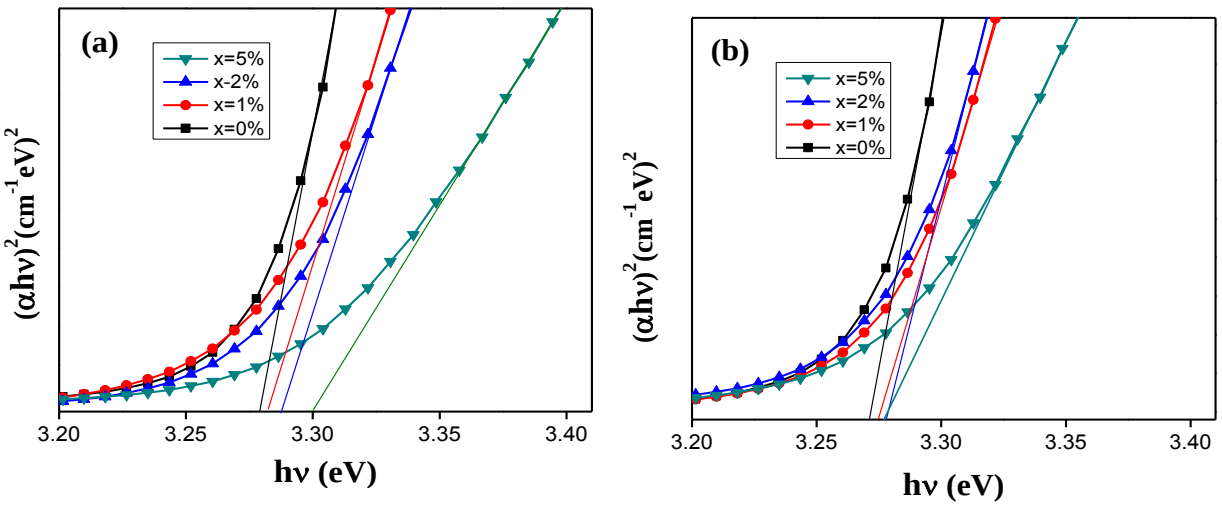

Figure 42. Optical band gap of pure and Sc-doped ZnO films at different concentration *x*, and annealing temperature at 500ºC (a), and 550ºC (b), for 1 hour in both cases.

Table 8 Estimated band gap values of Scandium doped ZnO/quartz films.

x = Sc at%	E_g(eV) at 500ºC	E_g(eV) at 550ºC
0%	3.27	3.27
1%	2.28	3.28
2%	2.28	3.28
5%	3.30	3.28

B.2 Photoluminescence measurements

Figure 43 shows the room-temperature PL spectra of pure and Scandium doped ZnO/quartz thin films annealed at 500ºC (a) and 550ºC (b). The spectra were recorded for an excitation wavelength of 342 nm. As seen, an evident emission band in the UV region centered on 390 nm was clearly identified in all samples. However, a strong dependence of the UV emission band intensity on the Sc concentration was evidenced. This emission band presents a quenching effect, due to trapping states formation produced by the dopant species as in the previous case for Co dopant ZnO films. It also can be attributed to a decrease in the average crystallite size

corroborated by XRD diffraction. The Sc doped ZnO films did not presented a visible band as in the Cobalt system and this vanishing band can suggest an actual substitution of the Sc dopants in the ZnO host.

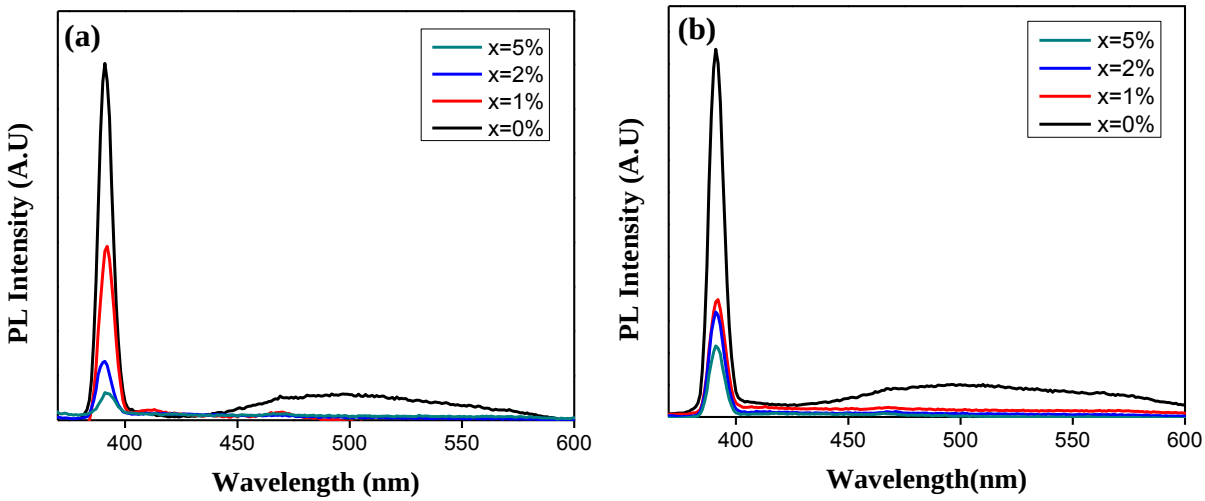

Figure 43. Room-temperature PL spectra of Sc^{3+}-doped ZnO/quartz films synthesized at various dopant atomic percentages *x*. The corresponding annealing temperatures were 500ºC, (a), and 550ºC, (b).

The major decrease in the UV principal emission was observed in Sc- (5 at%) doped ZnO at 500ºC. The decrease was 92% with respect to pure ZnO. The quenching of UV emission band is presented qualitatively in the Figure 44(a). For samples annealed at 550ºC the major decrease was 80% for Sc- (5 at%) doped ZnO, the quenching of UV emission band is shown in Figure 44(b).

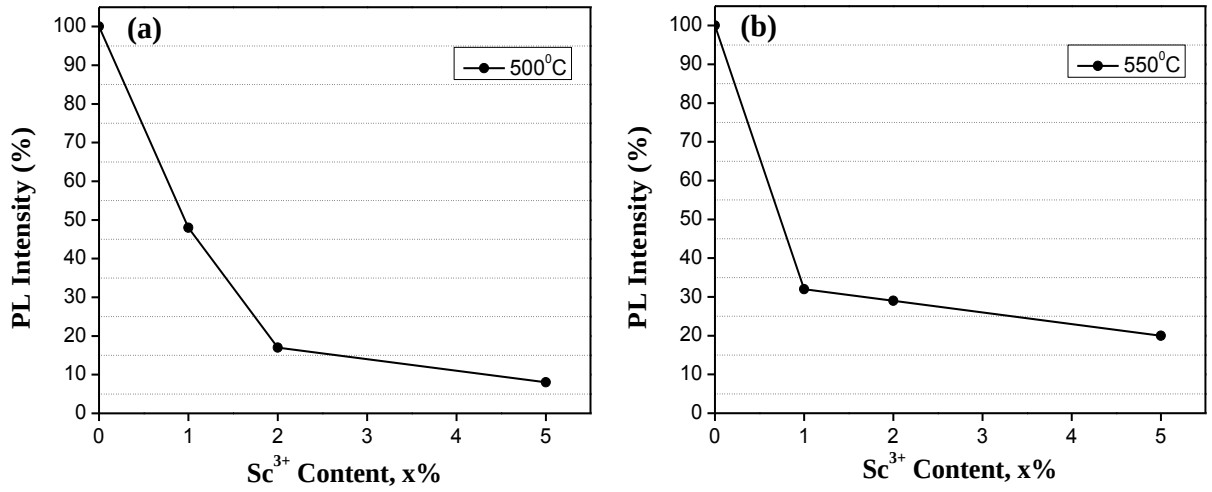

Figure 44. Room-temperature PL relative intensity for Sc^{3+}-doped ZnO films, at different dopant concentrations *x*, annealed at 500ºC (a), and 550ºC (b).

5.1.3 Bare and V- doped ZnO powders and films

5.1.3.1 Bare and V- doped ZnO powders

A. Thermogravimetric Analysis

Figure 45 shows the TGA profiles for the precursor powders containing V ions at atomic percentages between 0 at% and 5 at%. The shape of these profiles suggests a single thermal decomposition path which ends at approximately 350ºC at 0% and 2%. Two thermal decompositions were observed at 3%, 4% and 5%. This behavior could have a little phase of Vanadium Oxide. In all cases the biggest precursor decomposition is produced before 400ºC. This suggests that most of the organic composites in the samples were eliminated, and above 400ºC there is a formation of host oxide phase. Accordingly, annealing temperatures above 400ºC were selected for all subsequent tests.

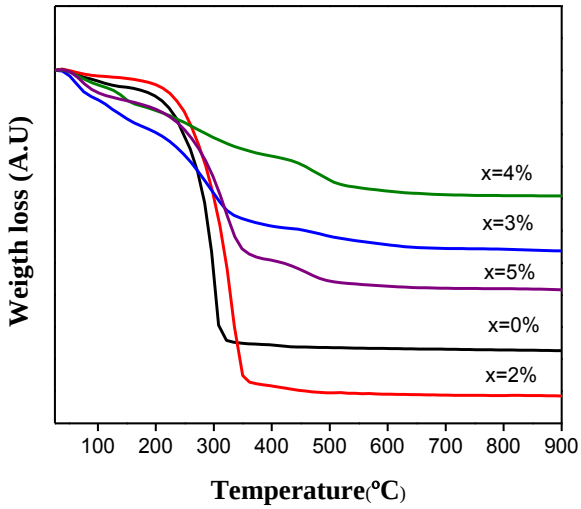

Figure 45. TGA profiles for precursor solids containing various atomic percentages *x*, of pure and V- doped ZnO. The heating rate was 10ºC / minute.

B. Structural properties

The X-ray diffractograms recorded from the V-doped ZnO powders (0, 2, 3, 4, and 5 at%) annealed at 400ºC and 500ºC for 1hour on air are shown in Figure 46(a) and Figure 46(b). All diffractions peaks correspond to the host ZnO phase with a hexagonal wurtzite structure. Minor amounts of isolated vanadium oxide were detected in samples synthesized with 4 and 5 at% V after annealing at 500ºC. Similar vanadium oxides were also observed by other researchers [58,112]. The incorporation of V^{3+} ions into the ZnO host lattice results in the average crystallite size to decrease from 25.90±0.15 nm to 13.27±0.56 nm and from 30.43±1.15 nm to 13.3±0.88 nm for annealing temperatures of 400ºC and 500ºC, respectively, and this effect can be corroborated with the widening of the diffraction peaks. Vanadium ions would retard the oxide crystallization process, in Table 9 presents a complete analysis for pure and doped ZnO at different concentrations of V ions and at the two annealing temperature. Furthermore the ionic radius of V^{3+} (0.78Å) is similar to Zn^{2+} (0.74Å), the exchange between V and Zn species produce distortions on the lattice of the ZnO unit cell. Also a noticeable shift to the left is observed in the

peaks (from 31.857º to 31.728º at 400ºC, and from 31.824º to 31.776º at 500ºC). This effect is produced by an effective incorporation of vanadium ions into the ZnO host principal. Figure 47(a) and Figure 47(b) show the detailed XRD analysis performed to verify the actual incorporation of the vanadium ions into the ZnO host. The shift of the diffraction peaks to lower diffraction angles with the increase in dopant concentration was clearly observed, corroborating our interpretation. The corresponding lattice parameters showed an increase with the concentration *x*, as is observed in Figure 48(a) and Figure 48(b).

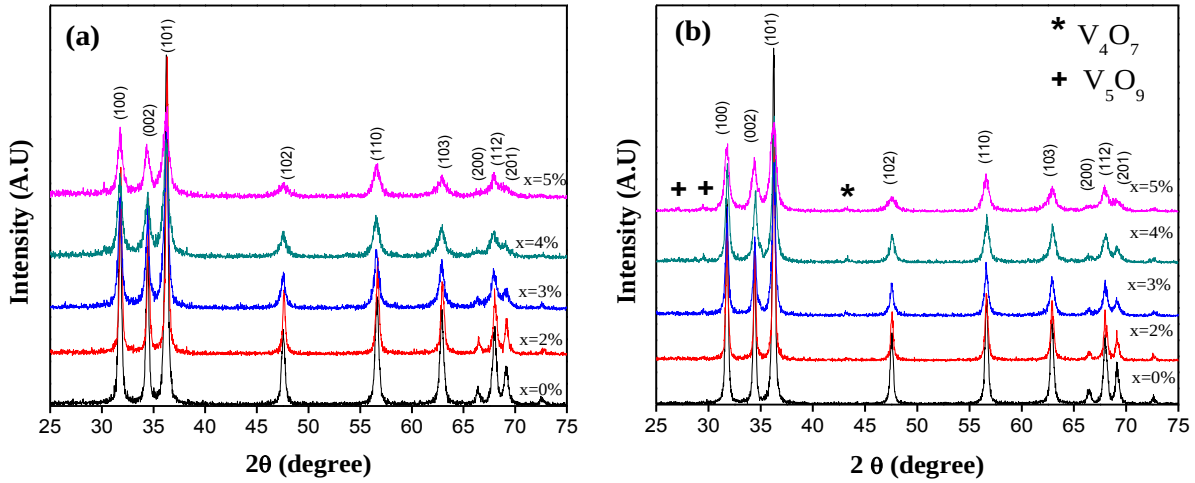

Figure 46. XRD patterns of V^{3+} -doped ZnO powders synthesized at various dopant atomic percentages *x*. The corresponding annealing temperatures were 400ºC (a), and 500ºC (b).

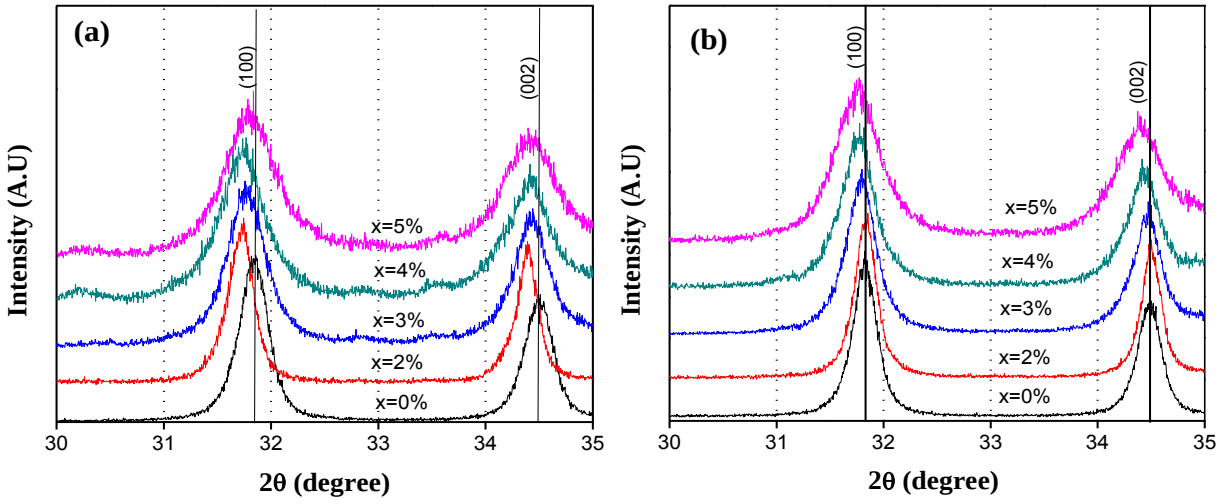

Figure 47. Detail of the XRD patterns of V-ZnO powders synthesized at various dopant atomic percentages. The corresponding annealing temperatures were 400ºC (a), and 500ºC (b).

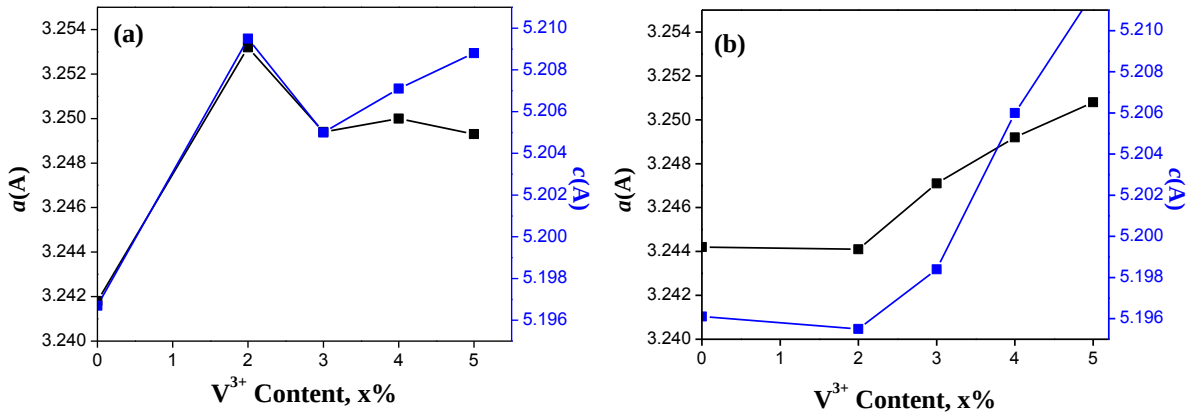

Figure 48. Variation of lattice parameters of ZnO powders with V^{3+} ions content *x*. The corresponding annealing temperatures were 400ºC (a), and 500ºC (b).

Table 9 Average crystallite size (± stdev) nm of Vanadium-ZnO powders.

x = V at%	T=400ºC	T=500ºC
0%	25.90 ± 0.15	30.43 ± 1.15
2%	15.39 ± 0.09	15.58 ± 0.26
3%	14.66 ± 0.23	15.02 ± 0.24
4%	13.70 ± 0.26	14.66 ± 0.22
5%	13.27 ± 0.56	13.30 ± 0.87

C. Optical properties

Figure 49 shows the room-temperature PL spectra of pure and V- doped ZnO powders at different dopant concentrations and annealed at 400ºC Figure 49(a), and 500ºC Figure 49(b). Here the only evident emission band in the UV region centered on 390 nm corresponds to the excitation recombination related to near-band edge emission of ZnO [113-115]. This radiative process was clearly explained in the Material Characterization section. This fact may corroborate that the developed synthesis route to powders did not favor the creation of defects in the structure usually associated with the luminescence in the visible region. However in the samples at 3% and 4% an emission in the visible region is observed. This can be attributed to the native defects

[116], e.g. the zinc vacancies due to incomplete incorporation of the dopants in the ZnO host principal. This fact would be corroborated by the presence of impurity phases in the samples as shown in the XRD patterns. This visible emission band has been reported by R. Slama [117] as corresponding to deep levels in ZnO. Furthermore the intensity of UV emission band decreases as V concentration increases. This suggests a quenching-by-concentration effect. A prominent decrease the UV emission band of 58 % with respect to pure ZnO for V- (4 at%) doped ZnO at 400ºC was observed. The quenching of UV emission band is presented qualitatively in Figure 50(a). In samples annealed at 500ºC, all the doped samples displayed a decrease in the UV emission band with the increase of the dopant concentrations, the quenching of UV emission band is shown in Figure 50(b).

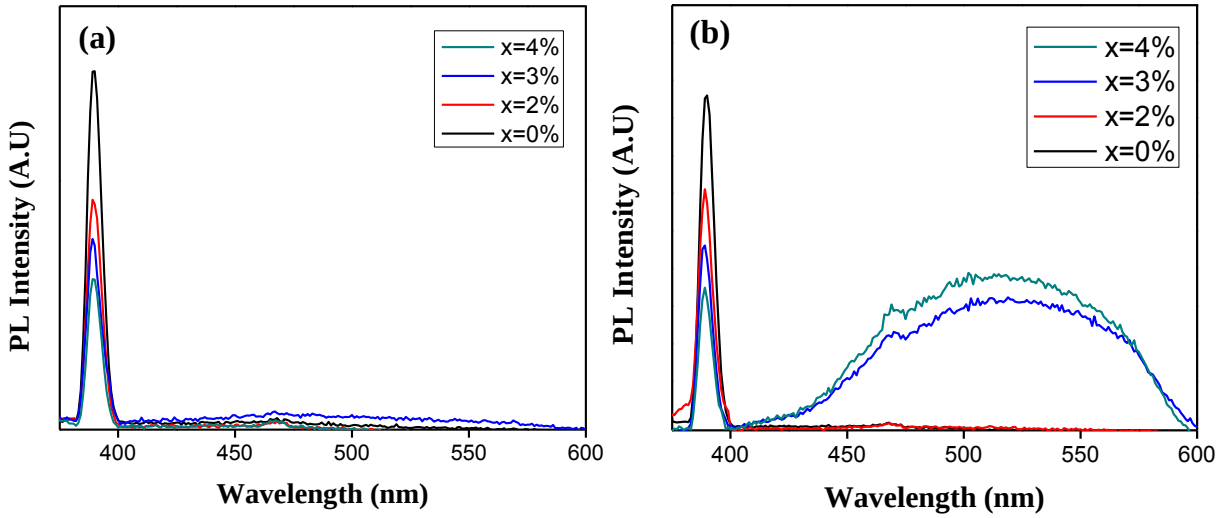

Figure 49. Room-temperature PL spectra for V^{3+}-doped ZnO powders, at different dopant concentrations *x*, annealed at 400ºC (a), and annealed at 500ºC (b)**.**

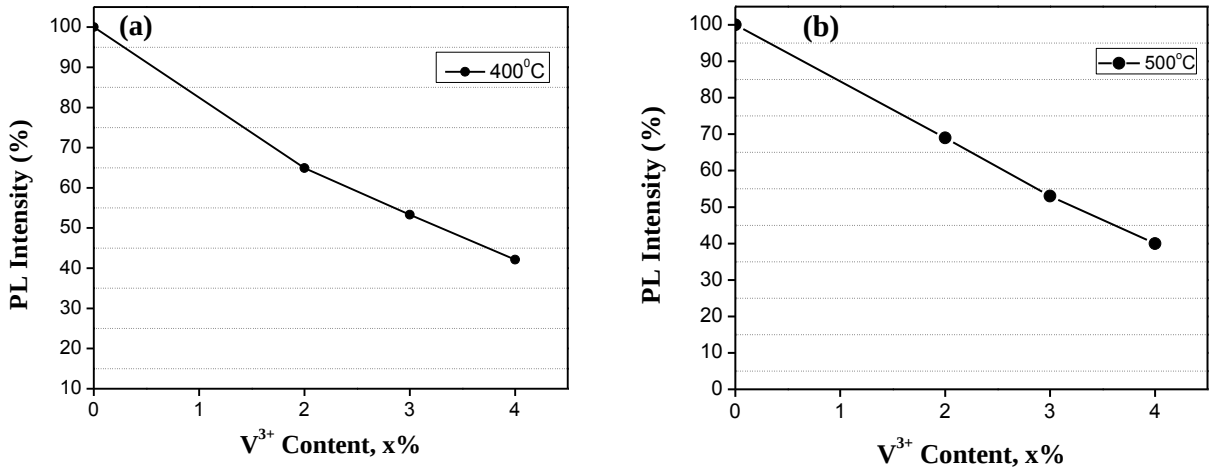

Figure 50. Room-temperature PL relative intensity for V^{3+}-doped ZnO powders, at different dopant concentrations *x*, annealed at 400ºC (a), and 500ºC (b).

D. Magnetic properties

Room-temperature M-H loops for V-doped ZnO powders annealed at 500ºC with different Vanadium concentrations are shown in Figure 51. These samples exhibited a weak ferromagnetic behavior with coercivity and saturation magnetization values shown in Table 10. This ferromagnetic behavior may be attributed to the super exchange interaction through oxygen (TM-O^{2-}-TM), where TM are the V^{3+} ions. The localized spin of Vanadium contribute with $4/3\mu_B$ per ion to the saturation magnetization. The observed ferromagnetism cannot be attributed to probable secondary phases of vanadium oxide (V_4O_7 and V_5O_9) due to their non-magnetic contribution [118,119]. Consequently the ferromagnetism observed can be attributed to the actual incorporation of V ions in the ZnO host, and this can be explained in terms of the bound magnetic polarons by J. Coey *et al.* [17], who proposed for this cases that the ferromagnetism is mediated by shallow donor electrons that form bound magnetic polarons, which overlap to create a spin-split impurity band. These mechanisms were explained in chapter II. Moreover this ferromagnetic order through bound magnetic polarons in oxide DMSs was experimentally confirmed by [120,121]. The ferromagnetism through bound magnetic polarons in our samples

can be attributed to the structural defects [122,123] formed in the annealing process, such us zinc vacancies. This fact is in agreement with the visible emission band displayed in the PL spectra in our samples. If the concentration of defects exceeds the percolation threshold, the superficial defects can overlap many dopant ions and close defects, inducing a ferromagnetic coupling between the dopant spins [124]. Therefore, the magnetic interaction between V ions at room temperature is ferromagnetic and mediated trough zinc vacancies.

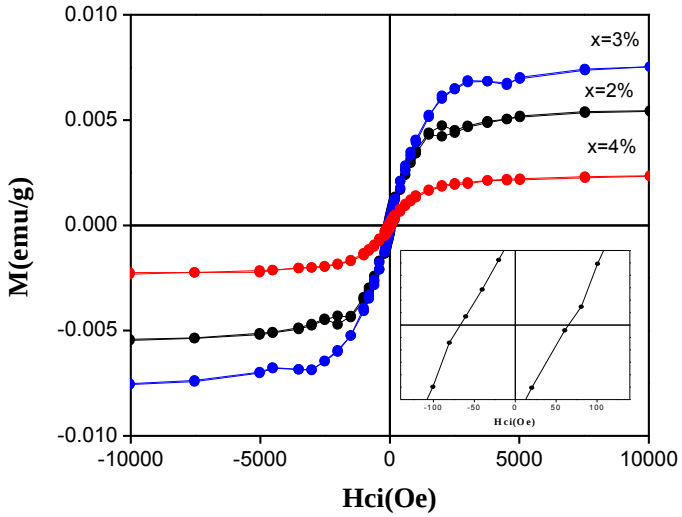

Figure 51. Room-temperature M-H loops of V^{3+} doped ZnO powders and annealing at 500ºC, with different concentrations of Vanadium ions.

Table 10 Magnetic properties at room temperature of Vanadium doped ZnO powders. The annealing temperature was 500ºC.

x = V at%	Coercivity (Oe)	Maximum Magnetization (emu/g)
2%	65	0.005
3%	48	0.008
4%	48	0.002

Figure 52 shows the M-H loops, measured in a SQUID system, of (V-2%) doped ZnO powders annealed at 500ºC. A subtraction of the diamagnetic contribution was made to all the samples except at 2 K measurement. These samples exhibited a weak ferromagnetic behavior with

coercivity and saturation magnetization values shown in Table 11. Furthermore magnetization increases from 0.0055 emu/g to 0.38 emu/g when the temperature decreases from 300K to 2K respectively. This effect is due to the fact that the super –exchange interaction tries to overcome the thermal disorder, hence as the temperature decreases the thermal fluctuations minimize consequently the magnetization increases [125]. Hiromasa Saeki has reported an increment in the saturation magnetization at low temperatures in V-doped ZnO [126].

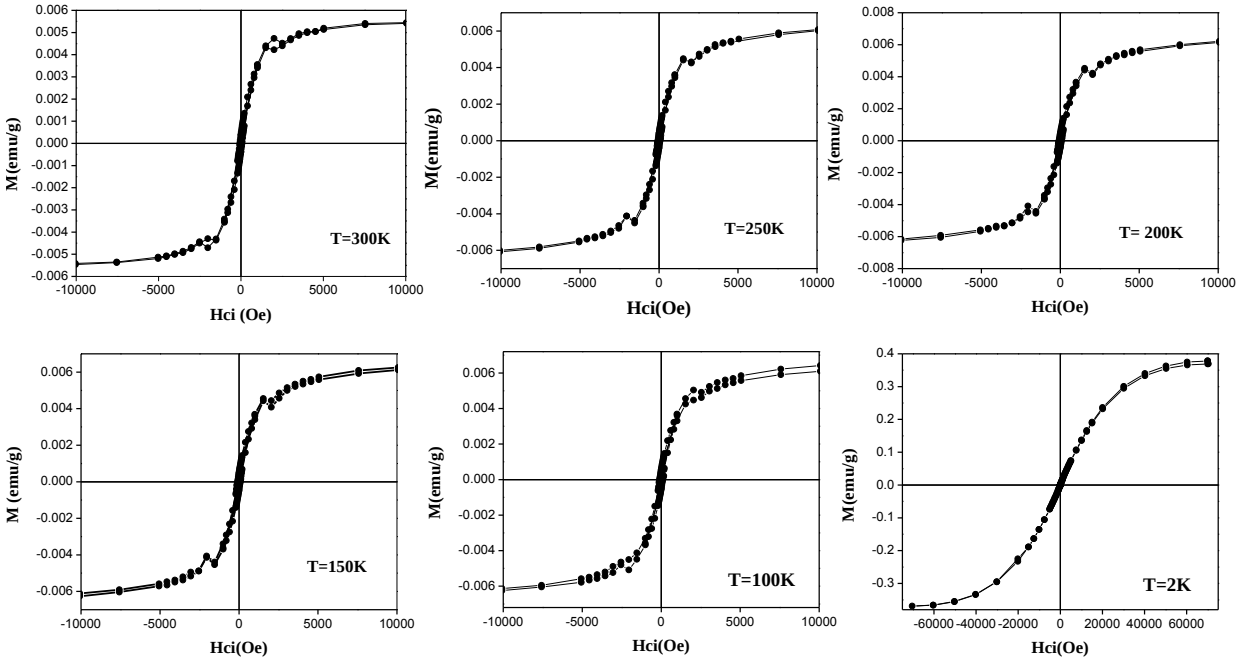

Figure 52. SQUID M-H loops at different temperatures of (V-2 at%) doped ZnO powders annealed at 500ºC.

Table 11 Magnetic properties at low temperature of (V-2 at%) doped ZnO powders annealed at 500ºC.

Temperature (K)	Coercivity (Oe)	Maximum Magnetization (emu/g)
300	65	0.0050
250	70	0.0060
200	78	0.0062
150	87	0.0063
100	100	0.0063
2	46	0.38

5.1.3.2 Bare and V- doped ZnO films

A. Structural properties

The X-ray diffractograms recorded from the V-doped ZnO/Quartz thin films (0, 2, 4, and 6 at%) annealed at 500ºC and 550ºC are shown in Figure 53(a) and Figure 53(b) respectively. The films have 10 layers and a thickness around 600 nm. All diffraction peaks were assigned to the well-crystallized ZnO wurtzite phase. The absence of impurity phases suggests the actual incorporation of V^{3+} (0.78 Å) in the Zn^{2+} (0.74 Å) sites.

This incorporation of V ions into the oxide lattice was also suggested by the slight but noticeable shift in the (002) XRD peak from 34.55º to 34.50º, when the V^{3+} doping level was increased from 0 to 6 at%. The 'c' lattice parameter was increased from 5.190Å (pure ZnO) to 5.202Å for the 6 at% V-doped ZnO sample and annealed temperature of 500ºC and a similar behavior was observed in the samples annealed at 550ºC. The incorporation of V-dopants caused the average crystalline size to decreases as shown in Table 12. The preferential growth of the (002) plane of the hexagonal ZnO unit cell was clearly evidenced in those samples synthesized in presence of V ions, and suggested the formation of columnar crystals in the corresponding films.

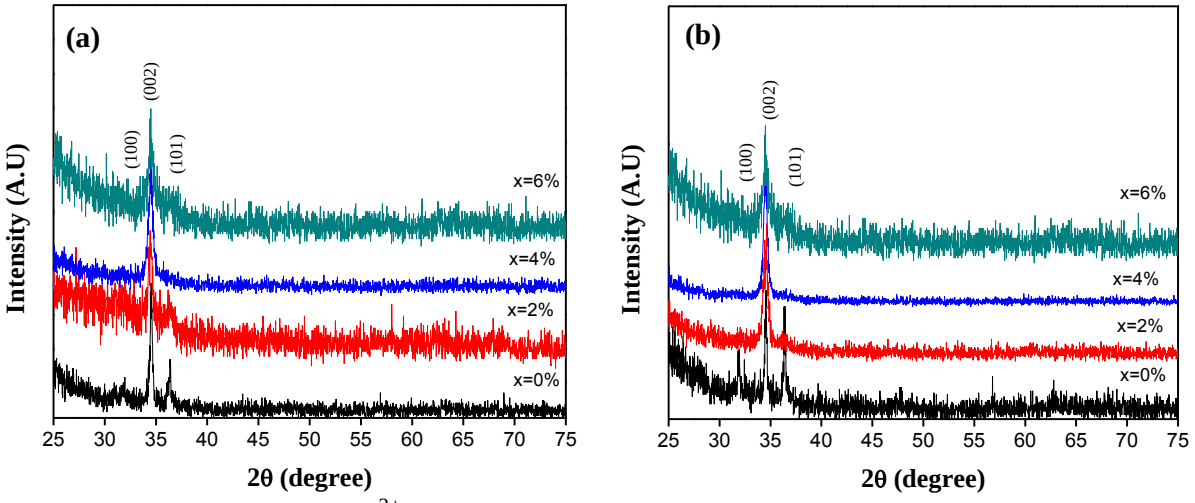

Figure 53. XRD patterns of V^{3+} -doped ZnO/quartz films synthesized at various dopant atomic percentages *x*. The corresponding annealing temperatures were 500ºC (a), and 550ºC (b).

Table 12 Average crystallite size (± stdev) nm of Vanadium doped ZnO/quartz films.

x = V at%	T=500ºC	T=550ºC
0%	25.7±0.10	28.50±1.02
2%	17.32	14.85
4%	14.84	15.99
6%	16.63	14.86

B. Surface morphology analyses by SEM

An SEM image recorded from the surface of a pure ZnO film is shown in Figure 54(a). The film was found to be uniform and approximately 1 μm thick as illustrated in the inset. Figure 54(b) is an SEM image recorded from a 4 at% V-doped ZnO film. Both samples were annealed at 500ºC for 1 hour. The micrographs evidence the nanocrystalline nature of the films and the effect of V-doping and the annealing temperature on the size of the grain with an average grain size of 46 ± 19.23 nm and 36 ± 20.7 nm for pure and 4 at% V-doped ZnO films respectively. These results are in agreement with the XRD data.

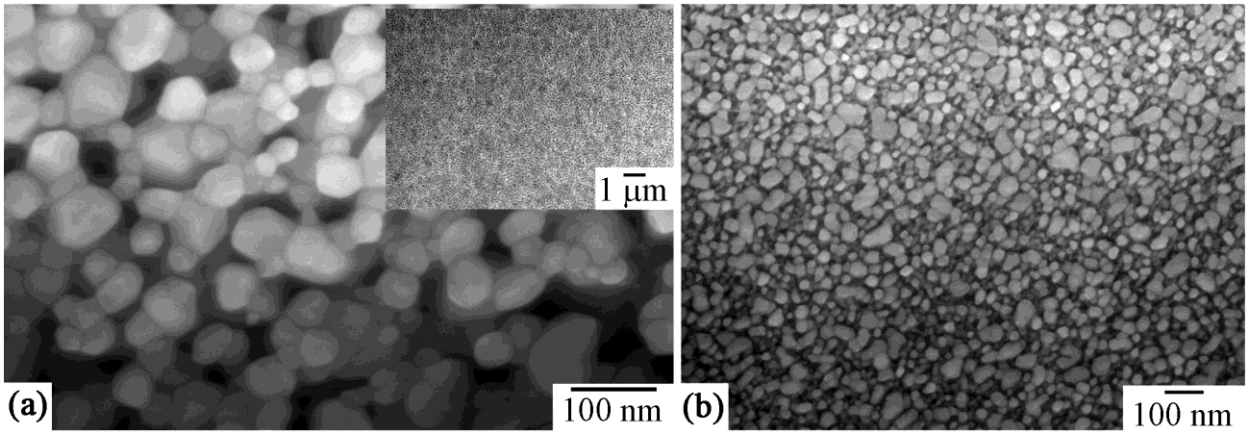

Figure 54. SEM images showing the morphology of pure ZnO film (a); compared to 4 at% V-doped ZnO film (b). The two samples were annealed at 500ºC for 1 hour.

C. Optical properties

C.1 Absorbance measurements

The UV-vis spectra recorded of pure and V-doped ZnO/quartz films at different concentration of V^{3+} ions are displayed in Figure 55 with annealed temperature of 500ºC (a), and 550ºC (b). The absorption peak was slightly blue-shifted from 373 nm to 365 nm when the concentration of V^{3+} ions in the films increased in the 0-6 at% range. These shifts according to the literature can be related to many factors such as thickness, grain size, structural parameter, lattice strain, carrier concentration, and presence of impurities or other defects, and even deviations from stoichiometry [94,127,128]. However in our samples the one of the main reasons for the increase seems to be the increasing dopant concentration (Moss-Burstein effect) and the decrease of the average crystallite size, a fact that can be confirmed by the above discussed XRD measurements. The band gap energy values were estimated using Tauc's relationship and are presented in Table 13. The extrapolation to determine the band gap values is plotted in Figure 56(a) 500ºC and Figure 56(b) 550ºC. The band gap energy was in the range of 3.27eV – 3.35 eV for pure and V-6 at% doped ZnO films respectively annealed at 500ºC and for samples annealed at 550ºC in the range of 3.27 eV- 3.32 eV. In all the samples the band gap values are similar to the ZnO bulk value 3.3 eV.

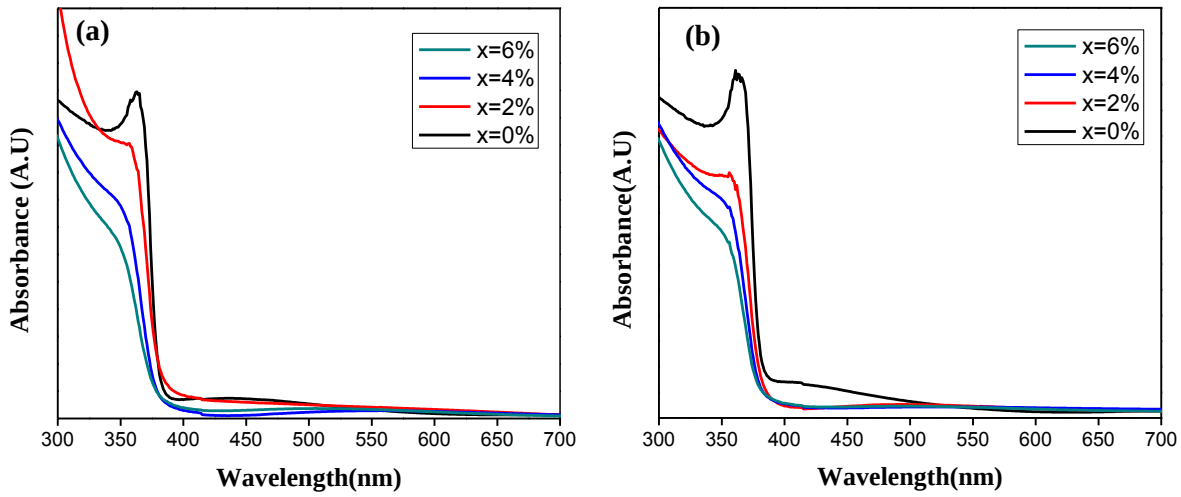

Figure 55. UV-Vis of V-doped ZnO/quartz films synthesized at various dopant atomic percentages *x*. The corresponding annealing temperatures were 500ºC (a), and 550ºC (b).

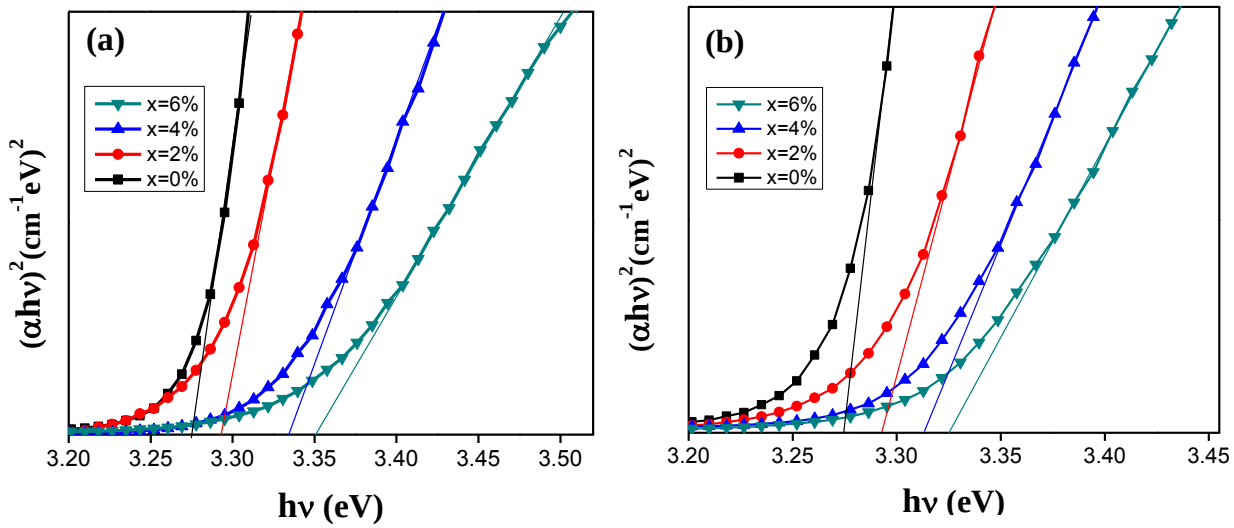

Figure 56. Optical band gap of pure and V-doped ZnO films at different concentration *x*, and annealing temperature 500ºC (a), and 550ºC (b), for 1 hour in both cases.

Table 13 Estimated Band gap of Vanadium doped ZnO/quartz films.

x = V at%	E_g(eV) at 500ºC	E_g(eV) at 550ºC
0%	3.27	3.27
2%	3.29	3.29
4%	3.33	3.31
6%	3.35	3.32

C.2 Photoluminescence measurements

Figure 57 shows the room-temperature PL spectra of pure and Vanadium doped ZnO/quartz thin films, annealed at 500ºC (a), and 550ºC (b), the spectra were recorded with the same excitation wavelength of previous samples. A strong emission band centered on 390 nm in the UV region is observed and attributed to the radiative annihilation of excitons with a very short life-time. This UV band was observed in all the samples. As can be seen, the intensity of the main emission band was strongly dependent on the dopant concentration. Again the emission band in the visible region, related to structural defects, was not observed for doped samples because of the elimination of zinc vacancies due to the actual incorporation of the V ions in the ZnO host. Furthermore, an evident decrease in the main emission band intensity with the increase of V^{3+} concentration is observed and can be attributed to a quenching-by concentration effect due to the trapped states formation, and also by the decrease on average crystallite size which can be evidenced by the XRD diffractograms. The quenching in the UV emission band was strongest in the V- (4 at%) doped ZnO annealed at 500ºC with a decrease of 80% with respect to the pure films and a decrease of 88% for V- (4 at%) doped ZnO at 550ºC. The quenching of UV emission band is presented qualitatively in Figure 58(a) and Figure 58(b) for films annealed at 500ºC and 550ºC respectively. This quenching in the UV emission band was also observed by J. Luo [129] at dopant concentrations higher than 3.5% of Vanadium concentration in doped ZnO films.

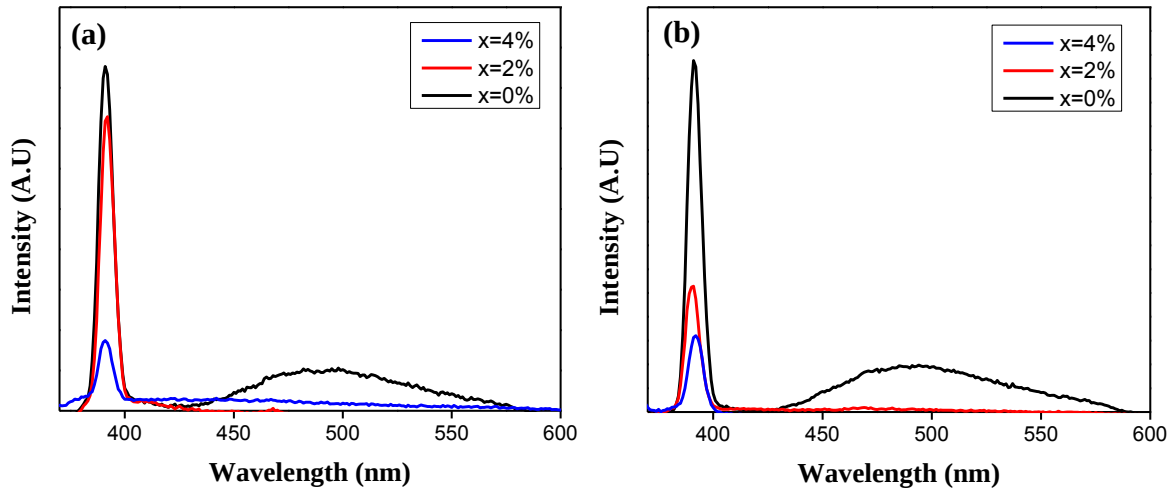

Figure 57. Room-temperature PL spectra of V^{3+}-doped ZnO/quartz films synthesized at various dopant atomic percentages *x*. The corresponding annealing temperatures were 500ºC (a), and 550ºC (b).

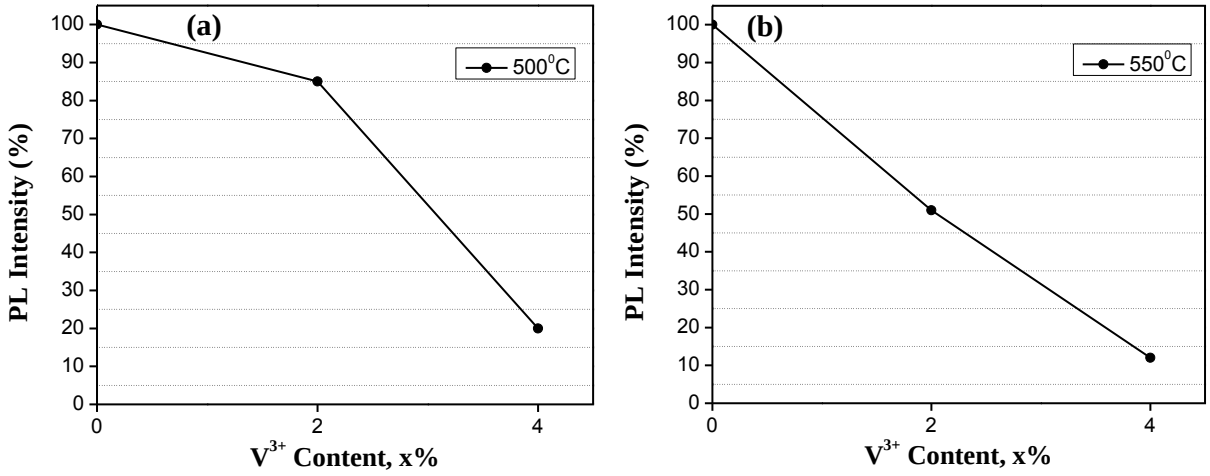

Figure 58. Room-temperature PL relative intensity for V^{3+}-doped ZnO films, at different dopant concentrations *x*, annealed at 500ºC (a), and 550ºC (b).

D. Magnetic Measurements

Figure 59 shows room-temperature M-H loops of V^{3+} doped ZnO/Si(100) films, at different concentrations of Vanadium ions and annealing temperatures (a) 500ºC and (b) 550ºC. These samples were grown in silicon substrates. The hysteresis loops at room temperature in all the samples, displayed weak ferromagnetic, which evidence that the critical temperature of this

material is above room temperature. A similar effect was reported by L. Mir [130]. The origin of the ferromagnetism in our V-doped ZnO films can be explained through a carrier-induced ferromagnetism (RKKY or double exchange interaction explained in chapter II) as was suggested by H. Saeki [60]. Saeki explained that in V-doped films it is not possible that other phases of vanadium oxides which are non-magnetic or antiferromagnetic can originate ferromagnetic responses, and concluded that the actual incorporation of V ions into the ZnO host results on carrier induced ferromagnetism as a likely explanation. Moreover, in our samples there is not a systematic effect of dopants concentration on the magnetization. The saturation magnetization and coercivity values are presented in Tables 14 and 15.

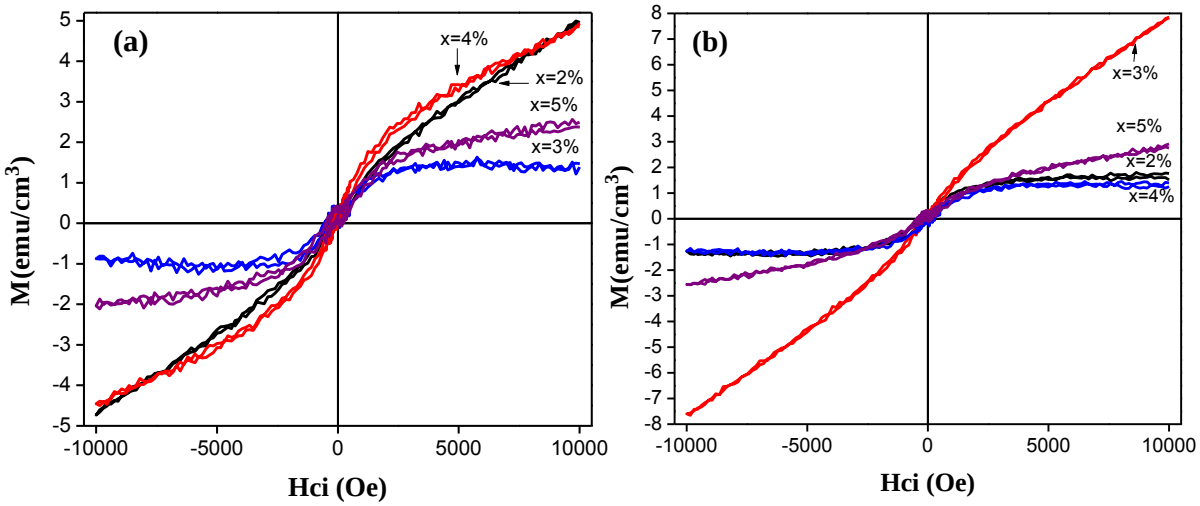

Figure 59. Rom-temperature M-H loops of V^{3+} doped ZnO films, at different concentrations *x*, and annealing temperature, 500ºC (a), and 550ºC (b).

Table 14 Magnetic properties at room temperature of Vanadium doped ZnO/Si(100) films, annealing temperature 500ºC.

x= V at%	Coercivity (Oe)	Maximum Magnetization (emu/cm^3)
2%	100	No saturation
3%	150	1.38
4%	133	No saturation
5%	220	2.45

Table 15 Magnetic properties at room temperature of Vanadium doped ZnO/Si(100) films, annealing temperature 550ºC.

x = V at %	Coercivity (Oe)	Maximum Magnetization (emu/cm^3)
2%	170	1.74
3%	151	No saturation
4%	220	1.32
5%	260	2.67

Concluding Remarks

XRD results suggested the actual incorporation of cobalt dopants in the ZnO host. PL measurements evidenced a quenching of the intensity of the main emission peak. The incorporation of Co was also conducive to the magnetic response in as-synthesized powders. The maximum coercivity was 117 Oe for the Co (1 at%)-ZnO samples annealed at 500ºC. In turn, Co-doped ZnO films exhibited a preferential growth along the (002) plane. Pure films exhibited two emission bands corresponding to the UV and visible regions characteristic of ZnO, whereas the doped samples exhibited only the emission band in the UV region. The magnetic response in these doped films was not as evident as in the case of powders.

The quenching-by-concentration effect in luminescence was also observed in the Sc-doped samples. However, a weak but noticeable ferromagnetic behavior (coercivity up to 50 Oe) became evident in the Sc-5 at% sample annealed at 500ºC. In addition, Sc-doped ZnO films exhibited a preferential growth along the (002) plane and a quenching effect in the PL due to dopant concentration. The magnetic response was negligible in the doped films.

Vanadium doped ZnO powder exhibited an interesting behavior compared with the previous two systems, it achieved the maximum value in the saturation magnetization, 0.008emu/g, and a coercivity of 48 Oe for the 3 at% V sample annealed at 500ºC. A successive quenching in the

optical properties, as a function of the dopant level concentration, was not observed in the doped samples annealed at 500ºC, retaining excellent optical properties. This system presented small parasitic phases at dopant levels higher than 3%. The optimal sample corresponds to 2 at% V doped ZnO annealed at 500ºC with a saturation magnetization of 0.005 emu/g and coercivity of 65 Oe. For this reason a systematic analysis was made to study the magnetic properties at low temperatures where the highest saturation magnetization value was 0.38 emu/g at 2 K. In turn the vanadium doped ZnO/Si(100) films retain the optical properties, and also display a novel ferromagnetic response at room temperature. For the samples 5 at% V doped ZnO annealed at 500ºC a maximum coercivity of 220 Oe was obtained, and for the sample at the same dopant level annealed at 550ºC the coercivity was 260 Oe. In this sense this material becomes an excellent candidate for spintronic applications.

5.2 Bare and doped BFO films.

5.2.1 Bare Pr^{3+}-doped $BiFeO_3$ thin films

A. Structural measurements

The X-ray diffractograms were recorded for $Bi_{1-x}Pr_xFeO_3$/Pt thin films (0, 1, 2, 3, and 4 at%) annealed at 500ºC for 2 hours and are displayed in Figure 60. All diffraction peaks were assigned to the well-crystallized BFO rhombohedral phase. The absence of impurity phases suggests the actual incorporation of Pr^{3+} (1.13Å) in the Bi^{3+} (1.17Å) site, this fact can be corroborated by the systematic shift towards larger angles by increasing the dopant concentration from 0 to 4 at%. Furthermore, this apparent incorporation of Pr-dopants caused the average crystalline size to increase from 28 nm in pure BFO to 40 nm in the Pr (4 at%) doped BFO films.

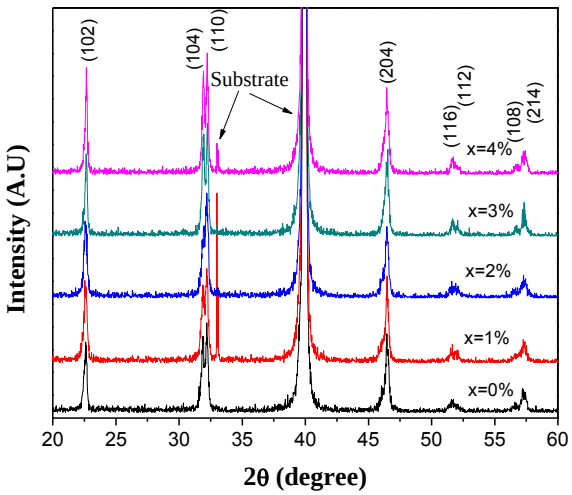

Figure 60. XRD patterns of pure and Pr^{3+}- substituted BFO/Platinum films synthesized at different atomic percentages *x*, annealed for 2 hours at 500ºC.

B. Film Surface Morphology Analyses by AFM

Figure 61 shows the AFM images of pure (a) and Pr (1 at%) doped BFO films (b). The film was found to be homogeneous with no evidence of cracking. The images evidenced the nanocrystalline nature of the films. The corresponding roughness values were 3.503 nm and 7.294 nm.

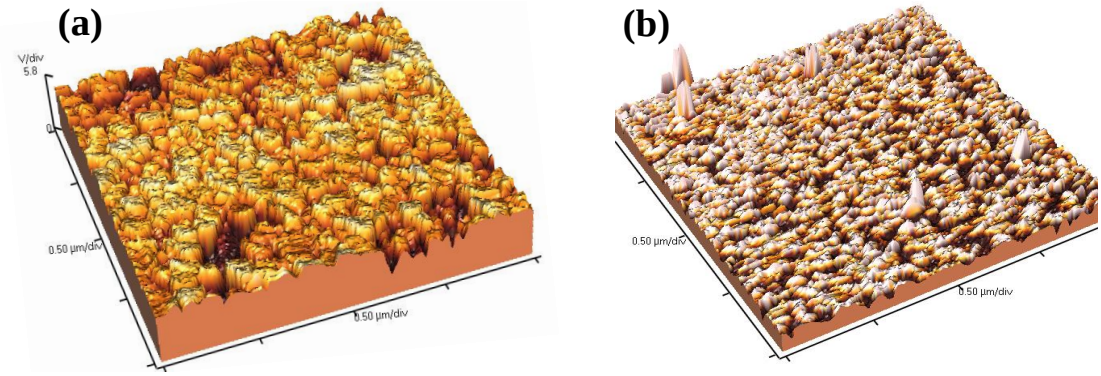

Figure 61. AFM images showing the morphology of pure BFO film (a), compared to 1 at% Pr doped BFO film (b). The two samples were annealed at 500ºC for 1 hour.

C. Magnetic properties

The magnetic hysteresis loops (M-H) of pure and doped $BiFeO_3$/Pt thin films, measured by VSM at room temperature, are shown in Figure 62. Pure BFO film showed weak hysteresis loop. Despite the fact that Bismuth ferrite has a short-range antiferromagnetic order, the weak

ferromagnetic behavior exhibited is attributed to the fact that the spins are not perfectly antiparallel so there is a weak canting moment of the sub-lattices producing a macroscopic magnetization [37, 41]. Also this weak ferromagnetism in pure BFO films has been reported in experiments [131-133]. But this phenomenon is still controversial [131,134] this weak ferromagnetism can be an intrinsic magnetic property or an extrinsic one, due to impurities like hematite or magnetite. The coercivity observed for these impurities is around 450 Oe and 25 Oe for hematite and magnetite respectively [131, 135]. Furthermore N. Kumar [131] has reported that the coercivity value for pure BFO films lies between those for hematite and magnetite concluding that these impurity phases are not presented in the material. Similar to Kumar's results, the coercivity value in our pure BFO films (166 Oe) also lies in between the values for hematite and magnetite, consequently the weak ferromagnetism in our samples cannot be attributed to those impurities. This fact can also be confirmed by XRD patterns, which does not display these kind of impurity phases.

Furthermore the doped samples also exhibited a weak ferromagnetic response and a diamagnetic trend for the samples with the Pr concentration level higher than 1%. This suggests an actual substitution of Pr ions in the BFO host, since these ions do not contribute to magnetization. The coercivity in the samples is in the range of 166 Oe for pure BFO to 428 Oe for Pr (4 at%) doped BFO, the increase in coercivity can be attributed to the crystal growth accordingly with the XRD results.

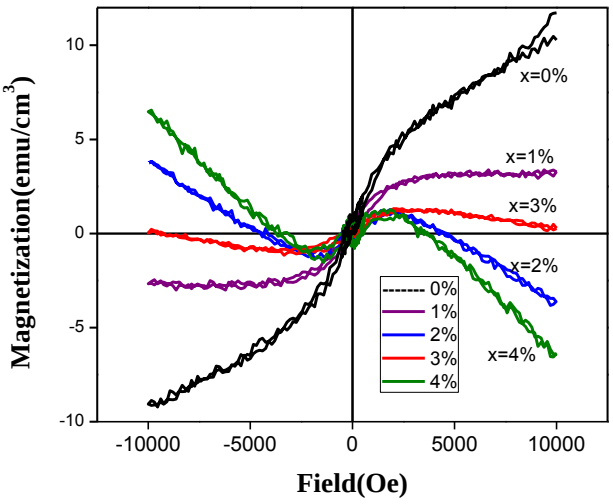

Figure 62. Room-temperature M-H loops for Pr doped $BiFeO_3$/Pt films synthesized at different Praseodymium atomic percentages *x*. The magnetic field was applied perpendicular to the film plane.

D. Ferroelectric measurements

The ferroelectric response was tested using RT 6000 HVS probe. The top Silver (Ag) electrodes, of diameter 80μm were deposited by RF sputtering. It was measured ferroelectric response of BFO and Praseodymium doped BFO films. All samples were applied a frequency range from 100 Hz to 1 KHz and a voltage range from 1 V to 9 V for each frequency. Figure 63 presents the measurements made at 7 V and 1 KHz for pure BFO and Pr-doped BFO, since these parameters showed the best response. The ferroelectricity of BFO rises from the relative displacements of Bi to the Fe-O octahedron along the direction [111] in the pseudo-cubic cell.

The ferroelectric response in BFO is still controversial since very large polarization, like 10 times the bulk value [69,136,137], and smaller than the bulk polarization values [131] have been reported. This large polarization reported has been attributed to the high-quality of the films. A weak ferroelectric behavior was observed in our pure and doped-BFO thin films, with a predominant paraelectric response in all the samples. The highest remnant polarization achieved

in this system was 3.69 μC/cm^2 in 3 at% Pr-doped BFO, while for pure BFO a remnant polarization of 1.96 μC/cm^2 was recorded.

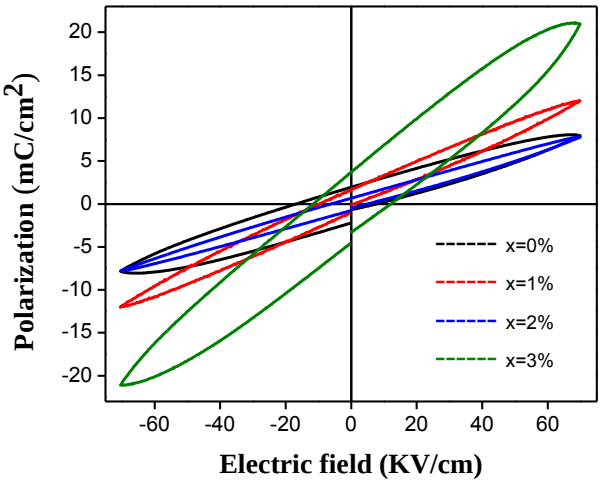

Figure 63. Room-temperature ferroelectric hysteresis loop, for Pr-substituted BFO/Pt films synthesized at different Pr^{3+} atomic percentages.

Our results are in agreement with the work reported by Kumar [131] in Pr-doped BFO films, where he observed a weak ferroelectricity at room temperature, and a very small increase of the remnant polarization with the increase of the Pr contents.

5.2.2 Bare and Co^{2+}-doped $BiFeO_3$ thin films

A. Structural properties

The X-ray diffractograms were recorded for $BiFe_{1-x}Co_xO_3$/Pt thin films (0, 1, 2,3 and 4 at%) annealed at 500ºC for 2 hours in pure BFO and 3 hours in doped BFO. All diffraction peaks were assigned to the well-crystallized BFO rhombohedral phase (Figure 64). The absence of impurity phases suggests the actual incorporation of Co^{2+} (0.72Å) in the Fe^{3+} (0.67Å) site. There is no systematic shift in the peak (102), which appears more or less in the same angular position.

Furthermore, the incorporation of Co-dopants does not cause an effect in the average crystalline size, getting 28 nm for pure BFO and around 31 nm for the doped samples in all dopant concentration levels.

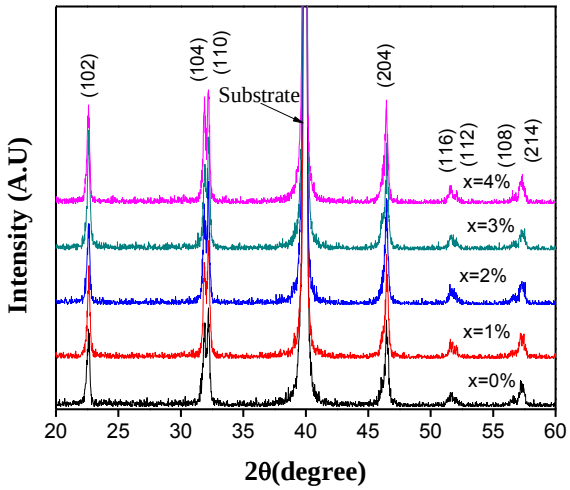

Figure 64. XRD patterns of pure and Co^{2+}- substituted BFO/Platinum films synthesized at different atomic percentages *x*, annealed at 500ºC for 3 hours.

B. Magnetic Measurements

The magnetic hysteresis (M-H) of pure and Co doped BFO/Pt thin films, measured by VSM at room temperature, is shown in Figure 65. In this case a weak ferromagnetic behavior in all the samples is observed. This can be attributed to the actual incorporation of the Co ions in the BFO host. There was no variation in coercivity with respect to the pure films. The coercivity value of the pure films was 166 Oe, and this can be related with the fact that in these films the average crystal size. Pure and doped BFO films, was around the same value and it can be seen in the XRD results.

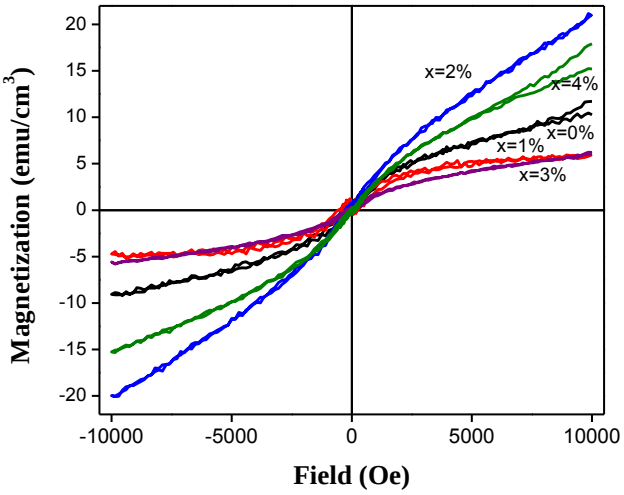

Figure 65. Room-temperature M-H loops for Co doped $BiFeO_3$/Pt films synthesized at different Cobalt atomic percentages *x*. The magnetic field was applied perpendicular to the film plane.

C. Ferroelectric Measurements

The ferroelectric response was tested using a RT 6000 HVS probe. The top Silver (Ag) electrodes, of diameter 80 μm, were deposited by RF sputtering. The ferroelectric response of BFO and Cobalt doped BFO films was measured. All the samples were applied a frequency range from 100 Hz to 1 KHz and a voltage range from 1 V to 9 V for each frequency. Figure 66 presents the measurements made at 5 V and 1 KHz for pure BFO and Co-doped BFO, since these parameters showed the best response. A weak ferroelectric behavior is observed with a predominant paraelectric response in all the samples, the highest remnant polarization achieved in this system was 4.65 $\mu C/cm^2$ in 2 at% Co-doped BFO, while for pure BFO a remnant polarization of 0.69 $\mu C/cm^2$ was recorded.

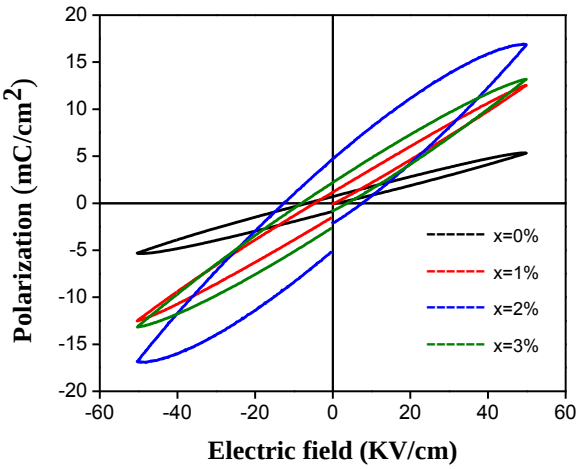

Figure 66. Room-temperature ferroelectric hysteresis loop for Co-substituted BFO/Pt films synthesized at different atomic percentages *x*.

Concluding Remarks:

In the analysis of BFO thin films the effect of the doping with two transition metal ions Co^{2+} and Pr^{3+} was evaluated. In both systems a well crystallized cubic rhombohedral structure of BFO were observed, and all the samples exhibited magnetic and ferroelectric responses.

In the system Pr doped BFO a control in the parasitic phases was achieved, the XRD patterns do not show any trace of Bi-oxides, Fe-oxides or oxides related to the dopants. This suggests the actual substitution of the Pr ions in the Bi sites. All the samples exhibited a weak ferromagnetic behavior. The maximum coercivity achieved was 428 Oe for Pr (4 at%) doped BFO annealed at 500ºC. Furthermore, the dopants play an important role in the electrical properties, a weak ferroelectric response with a predominant paraelectric behavior was accomplished. This can be attributed to high current leakage produced by the oxygen vacancies. The maximum remnant polarization achieved was 3.69 $\mu C/cm^2$ in Pr (3 at%) doped BFO annealed at 500ºC and this

sample had a magnetic coercivity of 366 Oe. Therefore this is the optimal sample achieved in the Pr system.

The substitution of the Co ions in the Fe sites also presents a cubic rhombohedral structure of BFO without parasitic phases; this system shows a similar behavior in magnetic and electrical properties of the Pr system. All the samples in the cobalt system present a weak ferromagnetic behavior, with a coercivity value around the pure films value annealed at 500ºC of 166 Oe. The samples exhibited non saturated hysteresis loop of Polarization versus electric field with a weak ferroelectric response and a predominant paraelectric trend at room temperature. The optimal sample was achieved for Co (2 at%) doped BFO annealed at 500ºC with a remnant polarization of 4.65 $\mu C/cm^2$ and magnetic coercivity of 163 Oe.

CHAPTER VI: GENERAL CONCLUSIONS

Pure and Cobalt, Scandium and Vanadium-doped ZnO powder and thin films were successfully synthesized via sol gel approach.

A dilute magnetic semiconductor for the powder in the samples annealed at 500ºC and different dopant concentrations was obtained. The achieved results become this ZnO based DMS in an important material due to the coexistence of the optical properties with a ferromagnetic response at room temperature. The vanadium doped ZnO system is the most interesting compared with the two others because it achieved a maximum saturation magnetization value of 0.008emu/g at room temperature for the 3 at% V sample annealed at 500ºC and a coercivity of 48 Oe. The Vanadium system presents small parasitic phases at dopant levels higher than 3% therefore the optimal sample corresponds to 2 at% V doped ZnO annealed at 500ºC with a saturation magnetization of 0.005 emu/g and coercivity of 65 Oe. For this reason a systematic study was made of the magnetic properties at low temperatures in this sample, and an increase in the saturation magnetization values until 0.38emu/g at 2 K was observed.

A DMS in thin films was developed with V doped ZnO/Si(100), at 500ºC and 550ºC. The films exhibited a weak ferromagnetic behavior at room temperature keeping good optical properties. For the samples 5 at% V doped ZnO annealed at 500ºC a coercivity of 220 Oe was obtained and for the same dopant level annealed at 550ºC the coercivity was 260 Oe. In this sense this material becomes an excellent candidate for spintronic applications.

Were successfully synthesized pure and Praseodymium and Cobalt doped BFO multiferroic thin films. A control over the parasitic phases of Bi-oxides and Fe-oxides was accomplished getting a single phase of BFO in all the samples. A weak ferroelectric and ferromagnetic behavior was

also achieved. The simultaneous coexistence of ferroelectric and ferromagnetic properties opens the possibility of magnetoelectric coupling at room temperature. The magnetoelectric features at room temperature of this material may be highly useful in numerous devices. These materials are promising candidates for applications in data storage devices, spintronics, and magnetoelectric sensor devices.

Our results suggest the actual substitution of the Pr ions in the Bi sites. All samples in this system exhibited a weak ferromagnetic behavior, the maximum coercivity achieved was 428 Oe in Pr (4 at%) doped BFO annealed at 500ºC. The maximum remnant polarization achieved was 3.69 μC/cm^2 in Pr (3 at%) doped BFO annealed at 500ºC, and this sample had a magnetic coercivity of 366 Oe therefore this is the optimal sample in the Pr system.

The substitution of the Co ions in the Fe sites also presents a cubic rhombohedral structure of BFO without parasitic phases. All the samples in the cobalt system present a weak ferromagnetic behavior with the highest coercivity value of 198 Oe in Co (3 at%) doped BFO annealed at 500ºC. The samples exhibited non saturated hysteresis loop of Polarization with a weak ferroelectric response and a predominant paraelectric trend at room temperature. The optimum sample was achieved Co (2 at%) doped BFO annealed at 500ºC with a remnant polarization of 4.65 μC/cm^2 and magnetic coercivity of 163 Oe.

In both cases the dopants play an important role in the electrical and magnetic properties. A weak ferroelectric response was observed with a predominant paraelectric trend. This can be attributes to the high current leakage produced by the oxygen vacancies in BFO.

REFERENCES

[1] K.H. Yoon, J.W. Choi, D.H. *Lee, Characteristics of ZnO thin films deposited onto Al/Si substrates by r.f. magnetron sputtering*, Thin Solid Films, **302,** 116, (1997).

[2] J. Hu, R. G. Gordon, *Textured aluminum-doped zinc oxide thin films from atmospheric pressure chemical- vapor deposition*, J. Appl. Phys. **71**, 880, (1992).

[3] H. Kim, J.S. Horwitz, S.B. Qadri, D.B. Chrisey, *Epitaxial growth of Al-doped ZnO thin films grown by pulsed laser deposition*, Thin Solid Films **420-421,** 107-111, (2002).

[4] J.H. Lee, K.H. Ko, J.L. Par*k, Electrical and optical properties of ZnO transparent conducting films by the sol–gel method*, J. Cryst. Growth **247,** 119-125, (2003).

[5] H. Liu and, X. Wang, *Rectangular and saturated hysteresis loops of BiFeO3 film on $LaNiO_3$ bottom electrode*, J. of Alloys and Compounds **485,** 769–772 (2009).

[6] M. M. Kumar, V. R. Palkar *et al. Ferroelectricity in a pure $BiFeO_3$ ceramic*, Appl. Phys. Lett. **76,** 2764 (2000).

[7] J.R. Sahu, C.N.R. Rao, *Beneficial modification of the properties of multiferroic $BiFeO_3$ by cation substitution*, Solid State Sciences. **9**, 950-954 (2007).

[8] Xiaobo He, Lian Gao, *Synthesis of pure phase $BiFeO_3$ powders in molten alkali metal nitrates*, Ceramics International. **35**, 975-978 (2009).

[9] M. H. Lee, S. C. Lee *et al*. *Improvement of the Ferroelectric and the Leakage Current Properties with Mn Doping in $BiFeO_3$ Thin Films*, Journal of the Korean Physical Society, **57**, 1901-1904, (2010)

[10] H. Ohno *et al*. *Making Nonmagnetic Semiconductors Ferromagnetic*, Science **281**, 951 (1998).

[11] Ahsan M. Nazmul, S. Sugahara, and M. Tanaka, *Ferromagnetism and high Curie temperature in semiconductor heterostructures with Mn δ-doped GaAs and p-type selective doping*, Physical Review B **67**, 241308(R) (2003).

[12] T. Dietl *et al. Zener Model Description of Ferromagnetism in Zinc-Blende Magnetic Semiconductors*, Science **287**, 1019 (2000).

[13] C. Zener, *Interaction Between the d shells in the transition metals*, Physical Review, **81**, 440, (1951).

[14] M. A. Ruderman, C. Kittel, *Indirect Exchange Coupling of Nuclear Magnetic Moments by Conduction Electron*, Physical Review, **96**, 99 (1954).

[15] Hadis Morkoç, Ümit Özgür, *Zinc Oxide Fundamentals, Materials and Device Technology*, WILEY-VCH (2009)

[16] A. Kaminski and S. Das Sarma, *Polaron Percolation in Diluted Magnetic Semiconductors***,** Phys. Rev. Lett., **88**, 247202, (2002).

[17] J. M. D. Coey, M. Venkatesan, and C. B. Fitzgerald, *Donor impurity band exchange in dilute ferromagnetic oxides*, Nature Mater, **4**, 173–179, (2005).

[18] F. Matsukura, H. Ohno, and T. Dietl, chapter 1 *III-V Ferromagnetic Semiconductors*, Handbook of Magnetic Materials vol. 14, edited by K. H. J. Buschow (Elsevier, Amsterdam, 2002) p. 1-87.

[19] K. Sato, H. Katayama-Yoshida, *First principles materials design for semiconductor spintronics*, Semicond. Sci. Technol., **17**, 367–376, (2002).

[20] S. Datta, B. Das, *Electronic analog of the electro optic modulator*, Appl. Phys. Lett., vol. **56**, 665–667, (1990).

[21] R. Fiederling *et at*. *Injection and detection of a spin-polarized current in a light-emitting diode*, Nature, **402**, 787–790 (1999)
[22] T. Gruber *et al*. *Electron spin manipulation using semimagnetic resonant tunneling diodes*, Appl. Phys. Lett., **78**, 1101–1103, (2001).
[23] F. J. Jedema *et al*. *Electrical spin injection and accumulation at room temperature in an all-metal mesoscopic spin valve*, Nature, **410**, 345–348, (2001).
[24] Y. Ohno *et al*. *Electrical spin injection in a ferromagnetic semiconductor heterostructure*, Nature, **402**, 790–792, (1999).
[25] Ü. Özgür *et al*. *A comprehensive review of ZnO materials and devices*, Journal of Applied Physics **98**, 041301, (2005).
[26] S. H. Wei and A. Zounger, *Role of metal d states in II-VI semiconductors,* Physical Review B **37**, 8958, (1988).
[27] J. L. Martins, N. Troullier, and S. H. Wei, *Pseudopotential plane-wave calculations for ZnS*, Physical Review B **43**, 2213, 1991.
[28] Y. N. Xu and W. Y. Ching, *Electronic, optical, and structural properties of some wurtzite crystals*, Physical Review B **48**, 4335, (1993).
[29] O. Zakharov, A. Rubio *et al. Quasiparticle band structures of six II-VI compounds: ZnS, ZnSe, ZnTe, CdS, CdSe, and CdTe*, Phys.Rev. B **50**, 10780, (1994).
[30] D. Vogel, P. Krüger, J. Pollmann, *Ab initio electronic-structure calculations for II-VI semiconductors using self-interaction-corrected pseudopotentials*, Physical Review B **52**, R14316, (1995).
[31] W. Eerenstein, N. D. Mathur, J. F. Scott, *Multiferroic and magnetoelectric materials*, Nature, **442,** 760, (2006).
[32] G.A Smolenskil and I. E. Chupis, *Ferroelectromagnets*, Sov. Phys. Usp. **25**, 475, (1982).
[33] Nicola A. Spaldin, Manfred Fiebig, *The Renaissance of Magnetoelectric Multiferroics*, Science **309**, 391, (2005).
[34] Stoner, E. C. *Atomic moments in ferromagnetic metals and alloys with non-ferromagnetic elements*, Philosophical Magazine Series 7, **15**, 1018-1034, (1933).
[35] Nicola A. Hill, *Why Are There so Few Magnetic Ferroelectrics?*, J. Phys. Chem. B, **104** 6694, (2000).
[36] Claude Ederer, Nicola A. Spaldin, *A new route to magnetic ferroelectrics*, Nature Materials, Vol. **3**, 849, (2004).
[37] Gustau Catalan, James F. Scott, *Physics and Applications of Bismuth Ferrite*, Advances Materials, **21**, 2463, (2009).
[38] V. M. Goldschmidt, *The laws of crystal chemistry*, Naturwissenschaften, Vol. **14**, 477- 485, (1926).
[39] F. Kubel, H. Schmid, *Structure of a Ferroelectric and Ferroelastic Monodomain Crystal of the Perovskite $BiFeO_3$*, Acta Cryst. B. Vol. **46**, 698, (1990).
[40] A. Palewicz, R. Przeniosło *et al*. *Atomic displacements in $BiFeO_3$ as a function of temperature neutron diffraction study*, Acta Cryst. B**63**, 537- 544, (2007).
[41] Claude Ederer, Nicola A. Spaldin, *Weak ferromagnetism and magnetoelectric coupling in bismuth ferrite*, Physical Review B **71**, 060401R, (2005).
[42] I. Sosnowska, T. Peterlin-Neumaier, E. Streichele, *Spiral magnetic ordering in bismuth ferrite*, J. Phys. C **15**, 4835 (1982).
[43] I. Sosnowska *et al*. *Crystal structure and spiral magnetic ordering of $BiFeO_3$ doped with*

Manganese, Appl. Phys. A: Mater. Sci. Process. **74**, S1040, (2002).
[44] Y. F. Popov *et al. Linear magnetoelectric effect and phase transitions in bismuth ferrite* $BiFeO_3$, JETP Letters **57**, 69 (1993).
[45] Dzyaloshinskii, *Thermodynamic theory of weak ferromagnetism in antiferromagnetic substances*, Sov. Phys. JETP, **5**, 1259, (1957).
[46] T. Moriya, *Anisotropic Superexchange Interaction and Weak Ferromagnetism*, Physical Review **120**, 91 (1960).
[47] J. R. Teague, R. Gerson, and W. J. James, *Dielectric hysteresis in single crystal* $BiFeO_3$, Solid State Commun. **8**, 1073, (1970).
[48] R. Seshadri, Nicola A. Hill, *Visualizing the Role of Bi 6s "Lone Pairs" in the Off-Center Distortion in Ferromagnetic* $BiMnO_3$, Chem. Mater. **13**, 2892, (2001).
[49] V. R. Palkar and R. Pinto, $BiFeO_3$ *thin films: Novel effects*, PRAMANA Journal of Phys, **58**, 1003-1008, (2002).
[50] V. R. Palkar, J. John, R. Pinto, *Observation of saturated polarization and dielectric anomaly in magnetoelectric* $BiFeO_3$ *thin films*, Appl. Phys. Lett., **80**, 1628 (2002).
[51] Shuiyuan Chen et. al, *Multiferroic properties and converse magnetoelectric effect in* $Bi_{1-x}Ca_xFeO_3$ *Ceramics*, Journal of Alloys and Compounds, **506**, 537–540, (2010).
[52] Dirk Vogel, *et. al*, *Self-interaction and relaxation-corrected pseudopotentials for II-VI semiconductors*, Physical Review B. **54**, 5495, (1996).
[53] K. Sato, H. Katayama-Yoshida, *Electronic structure and ferromagnetism of transition-metal-impurity-doped zinc oxide*, Physica B **308–310**, 904–907, (2001).
[54] K. Sato, H. Katayama-Yoshida, *Ferromagnetism in a transition metal atom doped ZnO*, Physica E 10, 251–255, (2001).
[55] M Kuzma, I Stefaniuk, M. Bester, *Theoretical models and EPR study of Cr based diluted magnetic semiconductors*, Journal of Physics: Conference Series **213,** 012035, (2010).
[56] B. E. Larson, K. C. Haas, H. Ehrenreich, *Theory of exchange interactions and chemical trends in diluted magnetic semiconductors*, Physical Review B **37,** 4137, (1988).
[57] L. El Mir *et al. Multifunctional ZnO:V thin films deposited by rf-magnetron sputtering from aerogel nanopowder target material*, Thin Solid Films **519**, 5787–5791, (2011).
[58] S. Karamat *et al. Structural, compositional and magnetic characterization of bulk* V_2O_5 *doped ZnO system*, Applied Surface Science Vol. **256**, 2309–2314, (2010).
[59] Jinghai Yang *et al. Structure and magnetism of* $Zn_{0.9}Co_{0.1}O$ *DMS films prepared by chemical solution deposition method*, Applied Surface Science, Vol. **258**, 64-67**,** (2011).
[60] H. Saeki, H. Tabataa and Tomoji Kawai, *Magnetic and electric properties of vanadium doped ZnO films*, Solid State Communications **120**, 439-443, (2001).
[61] C. H. Ziener, S. Glutsch, F. Bechstedt, *RKKY interaction in semiconductors:Effects of magnetic field and screening*, Physical Review B **70**, 075205 (2004).
[62] **N.** Hoa Hong, Joe Sakai, A. Hassini, *Magnetism in V-doped ZnO thin films*, Phys. Condens. Matter. **17,** 199–204, (2005).
[63] C. Xu *et al. Ferromagnetism of aligned* $Zn_{1-x}V_xO$ *nanorods grown by a vapour transport route*, J. Phys. D: Appl. Phys. **41,** 195005, (2008).
[64] M. Venkatesan *et al. Anisotropic Ferromagnetism in Substituted Zinc Oxide*, Phys. Rev. Lett. **93**, 177206, (2004).

[65] O Toulemonde, M Gaudon, *New examination of the magnetic properties of cobalt-doped ZnO diluted magnetic semiconductors*, J. Phys. D: Appl. Phys. **43,** 045001, (2010).
[66] Kenji Ueda, Hitoshi Tabata, Tomoji Kawai, *Magnetic and electric properties of transition-metal-doped ZnO films*, Appl Phys Lett, **79**, 988 (2001).
[67] R. Slama *et al*. *Visible photocatalytic properties of vanadium doped zinc oxide aerogel nanopowder*, Thin Solid Films, Vol. **519**, 5792–5795 (2011).
[68] S. Thota, L. M. Kukreja, J. Kumar, *Ferromagnetic ordering in pulsed laser deposited* $Zn_{1-x}Ni_xO/ZnO$ *bilayer thin films*, Thin Solid Films **517**, 750–754 (2008).
[69] J. Wang *et al. Epitaxial* $BiFeO_3$ *Multiferroic Thin Film Heterostructures*, Science. **299**, 1719 (2003).
[70] B. Ruette *et al. Magnetic-field-induced phase transition in* $BiFeO_3$ *observed by high-field electron spin resonance: Cycloidal to homogeneous spin order*, Physical review B. **69**, 064114 (2004).
[71] T. Kimura *et al. Magnetic control of ferroelectric polarization*, Nature **426,** 55 (2003).
[72] B. Bhushan *et al. Effect of alkaline earth metal doping on thermal, optical, magnetic and dielectric properties of* $BiFeO_3$ *nanoparticles***,** J. Phys. D: Appl. Phys. **42**, 065004, (2009).
[73] C. Chung, J. Lin, J. Wu, *Influence of Mn and Nb dopants on electric properties of chemical solution depositied* $BiFeO_3$ *films*, Appl. Phys. Letters, **88**, 24, 242909, (2006).
[74] B. Yu, M. Li, J. Liu *et al. Effects of ion doping at different sites on electrical properties of multiferroic*$BiFeO_3$ *ceramics*, J. Phys. D: Appl. Phys. **41**, 065003, (2008).
[75] K. Young Yun *et al. Enhancement of electrical properties in polycrystalline* $BiFeO_3$ *thin films*, Appl. Phys. Lett. **89**, 192902 (2006).
[76] P. Uniyal, K. Yadav, *Pr doped bismuth ferrite ceramics with enhanced multiferroic properties*, J. Phys.: Condens. Matter **21**, 405901, (2009).
[77] S.H. Lee *et al. Piezoelectric coefficient of* $BiFe_{1-x}Mn_xO_3$ *thin films measured by piezoresponse force microscopy*, Physica **B. 383**, 31–32 (2006).
[78] P. singh *et al. Magnetic and ferroelectric properties of epitaxial Sr-doped thin films*, Solid State Communications **150**, 431-434, (2010).
[79] X. Wang, H. Liu, B. Yan, *Enhanced ferroelectric properties of Ce-substituted* $BiFeO_3$ *thin films on* $LaNiO_3$*/Si substrates prepared by sol–gel process*, Journal of the European Ceramic Society **29**, 1183–1187, (2009).
[80] S. K. Singh *et al. Enhanced polarization and reduced leakage current in* $BiFeO_3$ *thin films fabricated by chemical solution deposition*, Journal of Applied Physics, **100**, 064102 (2006)
[81] B. D Cullity, *Elements of X-ray Diffractions*, edited by Morris Cohen (Addison Wesley, MA, 1972), pp. 99, 309.
[82] Adrian Parra, (2006), *Room-Temperature Synthesis and Characterization of Highly Monodisperse Transition Metal-Doped ZnO Nanocrystals*, Master of Science, University of Puerto Rico at Mayagüez Campus, Puerto Rico.
[83] Bob B. He, *Two-Dimensional X-Ray Diffraction*, (John Wiley & Sons, Inc. New Jersey 2009), p. 5.
[84] J.J. Lu *et al. Conductivity enhancement and semiconductor–metal transition in Ti-doped ZnO films*, Optical Materials **29,** 1548–1552 (2007).

[85] D.R. Baer, S. Thevuthasan, Chapter 16 *Characterization of Thin Films and Coatings*, Handbook of Deposition technology for films and Coating, 3rd ed, edited by Peter Martin (Elsevier, US, 2010), p. 780.
[86] D. Heiman, *Photoluminescence Spectroscopy*, Class of Physics of Waves and Optics, Northeastern University, (2004).
[87] Thierry Goudon *et al. On the Shockley-Read-Hall Model: Generation-Recombination in Semiconductors*, AMS subject classification: 78A35, (2007).
[88] Anderson Janotti, Chris G Van de Walle, *Fundamentals of zinc oxide as a semiconductor*, Rep. Prog. Phys. **72**, 126501, (2009).
[89] J. Hays *et al. Effect of Co doping on the structural, optical and magnetic properties of ZnO Nanoparticles*, J. Phys. Condens. Matter, **19**, 266203 (2007).
[90] S. Shionoya, W.M. Yen, *Phosphor Handbook*, (CRC Press, Boca Raton, Florida. 1999).
[91] A. S. Risbud *et al. Magnetism in polycrystalline cobalt-substituted zinc oxide*, Physical Review B **68**, 205202 (2003).
[92] K. Sato, H. Katayama-Yoshida, *Stabilization of Ferromagnetic States by Electron Doping in Fe-, Co- or Ni-Doped ZnO*, Japanese Journal of Applied Physics, **40**, L334, (2001).
[93] K. Ando1 *et al. Large magneto-optical effect in an oxide diluted magnetic semiconductor* $Zn_{1-x}Co_xO$, Appl. Phys. Lett. **78**, 2700 (2001).
[94] Liwei Wang *et al. Structure and optical properties of ZnO:V thin films with different doping concentrations*, Thin Solid Films **517,** 3721–3725, (2009).
[95] Mingsong Wang *et al. Optical and photoluminescent properties of sol-gel Al-doped ZnO thin films*, Materials Letters, **61**, 1118–1121, (2007).
[96] K. Sakaia *et al*. *Defect centers and optical absorption edge of degenerated semiconductor ZnO thin films grown by a reactive plasma deposition by means of piezoelectric photothermal spectroscopy*, J. Applied Physics, **99**, 043508, (2006).
[97] Marius Grundmann, *The Physics of Semiconductors: An Introduction Including Nanophysics and Applications Handbook*, second edition (Springer, NY, 2010), p. 291-292.
[98] D. Paul Joseph and C. Venkateswaran, *Bandgap Engineering in ZnO By Doping with 3d Transition Metal Ions*, Journal of Atomic, Molecular, and Optical Physics Volume 2011, Article ID 270540, 7 pages doi:10.1155/2011/270540 (2011).
[99] K. Vanheusden, *Correlation between photoluminescence and oxygen vacancies in ZnO phosphors*, Appl. Phys. Lett. **68**, 403, (1996).
[100] P. K. Samanta, *Visible Emission from ZnO Nanorods Synthesized by a Simple Wet Chemical Method*, International Journal of NanoScience and Nanotechnology ISSN 0974– 3081, **1**, 81-90 (2009).
[101] Cheng Ying Chen, *et al. Surface effects on optical and electrical properties of ZnO nanostructures*, Pure Appl. Chem., **82**, 2055 (2010).
[102] Ilan Shalish *et al*. *Size-dependent surface luminescence in ZnO nanowires*, Physical Review B **69**, 245401 (2004).
[103] W. K. Hong *et al*. *Electrical Properties of Surface-Tailored ZnO Nanowire Field-Effect Transistors*, IEEE Trans. Electron Devices, **55**, 3020 (2008).
[104] J.T. Luo *et al*. *The electrical, optical and magnetic properties of Si-doped ZnO films*, Applied Surface Science, **258**, 2177 (2012).
[105] E. Wolska *et al. Optical Properties of ZnCoO Films and Nanopowders*, Acta Physica Polonica A, **116**, 918, (2009).

[106] Guozhong Xing *et al*. *Charge transfer dynamics in Cu-doped ZnO nanowires*, Applied Physics Letters **98**, 102105, (2011).
[107] Aihua Wang *et al. Nano-structure, magnetic and optical properties of Co-doped ZnO films prepared by a wet chemical method*, J. Phys. D: Appl. Phys. **41**, 215308 (5pp), (2008).
[108] Ruchika Sharma *et al. Epitaxial growth of Sc-doped ZnO films on Si by sol–gel route*, Applied Surface Science, **255**, 5781–5788, (2009).
[109] J.M.D. Coey, d^0 *ferromagnetism*, Solid State Sciences **7**, 660–667 (2005).
[110] Seong Keun Kim *et al. Comparison between ZnO films grown by atomic layer deposition using* H_2O *or* O_3 *as oxidant*, Thin Solid Films, **478**, 103– 108, (2005).
[111] R. SHARMA, *Investigations of highly conducting and transparent Sc doped ZnO films grown by the sol-gel process*, Materials Science-Poland, **27**, No. 1, (2009).
[112] L. El Mir *et al.* Synthesis and luminescence properties of vanadium-doped nanosized zinc oxide Aerogel , Physica B, **403**, 1770–1774, (2008).
[113] Santi Maensiri *et al. Synthesis and optical properties of nanocrystalline V-doped ZnO powders*, Optical Materials, **29**, 1700–1705, (2007).
[114] S.C. Lyu *et al. Low temperature growth and photoluminescence of well-aligned zinc oxide nanowires*, Chem. Phys. Lett. **363**, 134-138, (2002).
[115] L. Bergman *et al. Photoluminescence dynamics in ensembles of wide-band-gap nanocrystallites and powders*, J. Appl. Phys. **96,** 675 (2004).
[116] Shubra Singh *et al. Investigation of low-temperature excitonic and defect emission from Ni-doped ZnO nanoneedles and V-doped ZnO nanostructured film*, New Journal of Physics, **12**, 023007, (2010).
[117] R. Slama *et al. Photocatalytic and optical properties of vanadium doped zinc oxide Nanoparticles*, Int. J. Nanoelectronic and Materials, **3**, 133- 142, (2010).
[118] A. C. Gossard *et al. Microscopic magnetic properties of metallic and insulating* V_4O_7 *and* V_7O_{13}, Physical Review B, **9**, 1230-1239, (1974).
[119] A. C. Gossard *et al. Microscopic magnetic properties of vanadium oxides. II.* V_3O_5, V_5O_9, V_6O_{11}, *and* V_6O_{13}, Physical Review B, **10**, 4178–4183, (1974).
[120] K.A. Griffin *et al. Intrinsic Ferromagnetism in Insulating Cobalt Doped Anatase* TiO_2, Phys. Rev. Lett. 94, 157204, (2005).
[121] P.I. Archer, D.R. Gamelin, *Controlled grain-boundary defect formation and its role in the high-Tc ferromagnetism of* Ni^{2+}*:*SnO_2, J. Appl. Phys. **99**, 08M107, (2006).
[122] S.H. Liu *et al. Effects of hydrogenated annealing on structural defects, conductivity, and magnetic properties of V-doped ZnO powders*, Appl. Phys. Lett. **90**, 222505, (2007).
[123] M. Naeem *et al*. *Effect of reducing atmosphere on the magnetism of* $Zn_{1-x}Co_xO$ *(*$0 \le x \le 0.10$*) nanoparticles*, Nanotechnology **17**, 2675, (2006).
[124] Z.M. Tian *et al*. *Synthesis and magnetic properties of vanadium doped anatase* TiO_2 *nanoparticles*, J. Magn. Magn. Mater. **320**, L5–L9, (2008).
[125] C. Kittel, *Introduction to solid state physics*, eight edition, (John Wiley & Sons, Inc. US 2005).
[126] Hiromasa Saeki *et al. Magnetic and electric properties of Vanadium doped ZnO films*, Solid State Communications, **120**, 439- 443, (2001).
[127] T. Ren, H.R. Baker, K.M. Poduska, *Optical absorption edge shifts in electrodeposited ZnO thin films*, Thin Solid Films **515**, 7976, (2007).

[128] R.E.Marottia *et al*. *Bandgap energy tuning of electrochemically grown ZnO thin films by thickness and electrodeposition potential*, Sol. Energy Mater. Sol. Cells, **82**, 85 (2004).
[129] J. T. Luo *et al. Microstructure and photoluminescence study of vanadium-doped ZnO films*, J. Phys. D: Appl. Phys. **42**, 115109 (2009).
[130] L. El Mir *et al. Multifunctional ZnO:V thin films deposited by rf-magnetron sputtering from Aerogel nanopowder target material*, Thin Solid Films, **519**, 5787–5791, (2011).
[131] N. Kumara, *et. al*, *Structural, dielectric and magnetic properties of Pr substituted* $Bi_{1-x}Pr_xFeO_3$ *(0≤x≤0.15) multiferroic compounds*, Journal of Alloys and Compounds **501**, L29–L32, (2010).
[132] R. Mazumder, A. Sen, *Effect of Pb-doping on dielectric properties of* $BiFeO_3$ *ceramics*, J. Alloys Compd. **475**, 577 (2009).
[133] J. Li, Y. Duan, H. He, D. Song, *Crystal structure, electronic structure, and magnetic properties of bismuth-strontium ferrites*, J. Alloys Compd. **315**, 259 (2001).
[134] Y.P. Wang *et al*. *Room-temperature saturated ferroelectric polarization in BiFeO3 ceramics synthesized by rapid liquid phase sintering*, Appl. Phys. Lett. **84**, 1731 (2004).
[135] R.C.O. Handley, Modern Magnetic Materials: Principles and Applications, (Wiley, New York, 2000).
[136] D. H. Kim *et al. Effect of epitaxial strain on ferroelectric polarization in multiferroic BiFeO3 films*, Appl. Phys. Lett. **92**, 012911 (2008).
[137] J. Li *et al. Dramatically enhanced polarization in (001), (101), and (111)* $BiFeO_3$ *thin films due to epitiaxial-induced transitions*, Appl. Phys. Lett. **84**, 5261 (2004).